UNIVERSITÀ DEGLI STUDI DI PALERMO

Dottorato in Fisica
Dipartimento di Fisica e Chimica
FIS-03

Nanorings driven by strong laser fields: dynamics and applications

IL DOTTORE
Dario Cricchio

IL COORDINATORE
Antonio Cupane

IL TUTOR
Emilio Fiordilino

CICLO XXVI
ANNO CONSEGUIMENTO TITOLO 2016

Part 1

Theory

1 Introduction

Our research started from the idea of creating a simple model that could explain some features of the interaction between graphene and laser. Graphene is a carbon allotrope composed of a monoatomic layer of atoms arranged in a regular hexagonal pattern and which has essentially a bidimensional geometry. It has important electrical, optical and mechanical properties, a high electronic mobility, and it can be rolled to form nanotubes that can be approximated to one-dimensional wires. The state of the art permits the fabrication of nanotubes whose length is much larger than the radius; in these conditions the energy states pertaining to the circular motion are practically unpopulated. It is this consideration that provides meaning to the one dimensional assertion. Graphene has important properties: it was realized that the dispersion relation is linear around the six corners of the two-dimensional hexagonal pattern, leading to zero effective mass for electrons and holes. If, in the graphene structure, we substitute particular hexagons with pentagons, the geometry becomes spherical and we obtain a new allotrope of the carbon: the fullerene C_{60}. The name is an homage to Buckminster Fuller, whose geodesic domes the fullerene resembles. Spherical fullerene are called Buckyballs; an example is the C_{60} whose structure is a truncated (T = 3) icosahedron (soccer-ball like) with 20 exagons and 12 pentagons. According to Euler's theorem these 12 pentagons are required for closure of the carbon network consisting of n hexagons and C_{60} is the first stable fullerene because it is the smallest possible to obey this rule. In this structure none of the pentagons make contact with each other. There exist fullerenes smaller of the

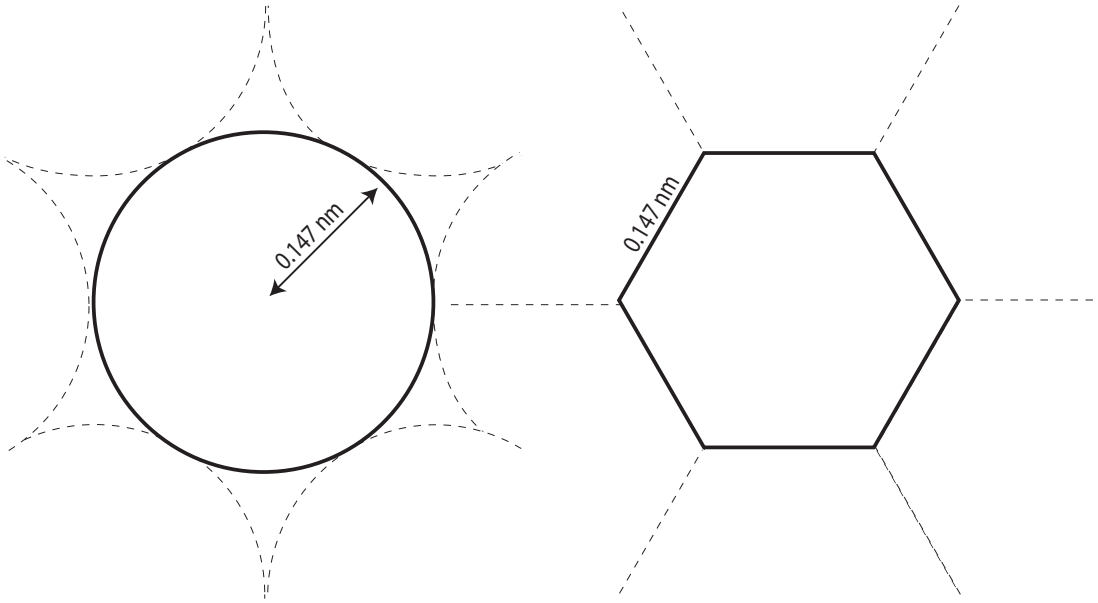

Figure 1.1: Equivalence between one single graphene cell and one nanoring.

C_{60}, but they have adjacent pentagons (called pentalene) that destabilize the structure. The fullere has been a topic of our recent research in which we have studied the behavior under the influence of a laser field. It has been shown that the use of C_{60} can also produce short pulses with duration of the order of $\tau \sim 2\sqrt{m_e R/eE_L}$ with R the radius of the fullerene, E_L the laser electric field strength, m_e the mass of the electron and e the positive elementary charge in [1, 2, 3].

Another interesting object is the nanoring, small ringformed crystal. The first nanoring fabricated was a zinc oxide nanoring with a diameter 1 to 4 μm and thin, wide shells that were 10 to 30 nm thick[4]. Nanorings consisting of Ag quantum dots with $C_{6\nu}$ symmetry interacting with a circularly polarized light were studied in [5], where it is shown that the high harmonic generation (HHG) spectra obtained from artificial nanorings are more intense than the HHG spectra obtained from benzene.

The main intuition of our research is to approximate the single cell of graphene to a nanoring. Our system is composed of one electron constrained on a circumference of which we calculate the emission of high harmonics and the polarization of the emitted harmonics. The origin of the harmonic generation is based in the non-linearity of the electron-laser interaction energy. This non-linear interaction forces

the molecule to emit a wide spectrum of harmonics of the pumping field. Optimizing our model, we have achieved an emission of harmonics compatible with that of the graphene. We will show our calculations compared with the experimental data. Furthermore we deepen the study of nanoring and their interaction with the laser and usage in quantum information.

Finally I will show the research conducted at the Max-Planck-Institut für Kernphysik about the momentum partition between constituents of exotic atoms during laser induced tunneling ionization.

2 Harmonic Generation Theory

2.1 Introduction

In order to understand the work done in these years, it is useful to explain what are the processes that are the basis of the generation of harmonics. Especially in the first part of the thesis I will discuss the following topics:

- Multiphoton ionization
- High Harmonic Generation
- Strong Field Approximation (SFA)

where I will explain the behavior of one electron driven by a laser field, consequently I will show the equations that permit to calculate the harmonic spectra.

2.2 Multiphoton Ionization and High Harmonic Generation (HHG)

Atoms and molecules driven by a laser field can be ionized by the absorption of the minimum number of photons necessary such that the total energy of the photons just exceeds tu the ionization energy E_s. If N is the number of absorbed photons, the energy of the emitted electron E_e will be:

$$E_e = N\hbar\omega - E_s < \hbar\omega \tag{2.1}$$

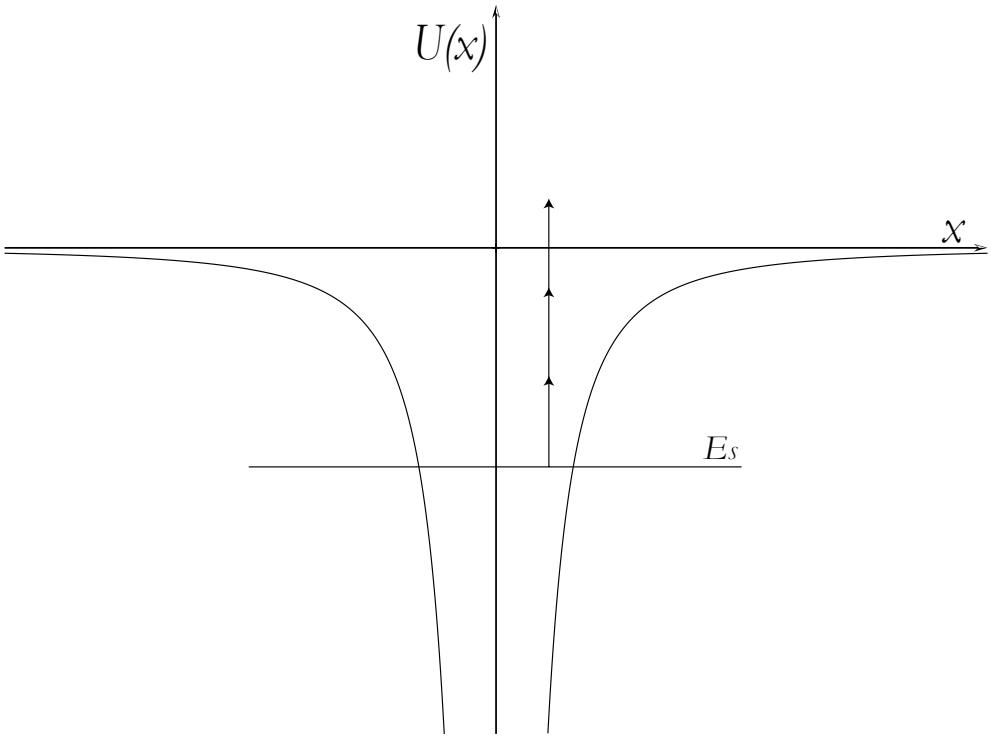

Having defined the multiphoton ionization, we can discuss the high harmonic generation (HHG) that describes the diffusion by the matter of high harmonics of the driving field. The HHG process can be described using the three-step model.

2.2.1 High Harmonic Generation

Usually the high harmonic generation can be described by three steps

I: An incident laser field ionize the atom and remove the electron from its ground state to the continuum (tunnel ionization).

II: The electron propagates in the laser field acquiring kinetic energy and its motion can be described classically.

III: The electron recombines emitting a photon of energy equal to kinetic energy acquired in the previous steps.

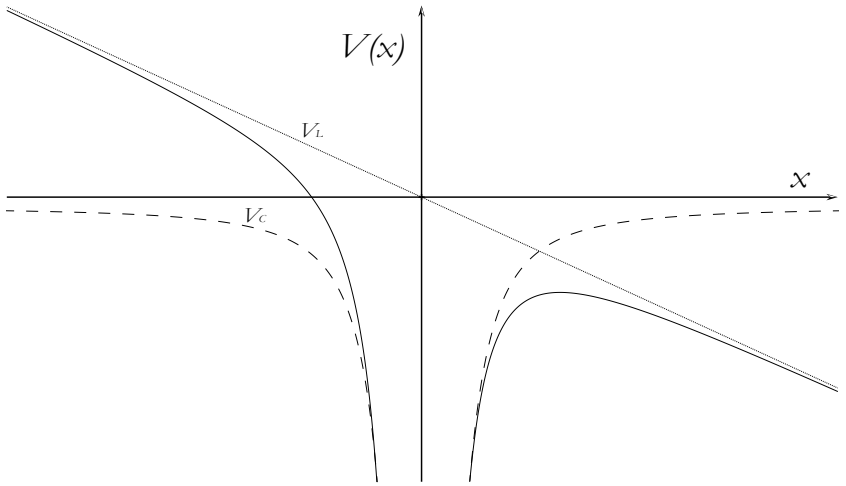

Figure 2.1: In this figure we show the total potential generated by superposition of the coulombian potential V_C (dashed line) and the laser potential V_L (pointed line) at the instant of maximum intensity.

Step I: Tunnel Ionization

In the tunnel ionization the electron absorbs a sufficient number of photons to exceed the barrier of potential. When the electron-laser interaction is comparable with the electron-nucleus force, the laser field cannot be described perturbatively. If we consider small frequencies and high intensity, the ionization can be described by means of a tunnel ionization. The laser-molecule interaction energy (in the single active electron approximation) is:

$$V_L = e\vec{\mathcal{E}}(t) \cdot \vec{r}$$

where $\vec{\mathcal{E}}(t)$ is the laser field and $\vec{r}$ is the electron position.

Step II: Propagation in the Laser Field

Due to high intensity of laser field, it is possible neglect the interation between electron and nucleus. In this picture, the electron is subordinate only to the force of laser field:

$$\vec{F} = m\vec{a} = -e\vec{\mathcal{E}}(t).$$

We suppose that the laser field is polarized along the z-axes and that its electric

field is described by:

$$\mathcal{E}_z(t) = \mathcal{E}_0 \cos(\omega_L t) \tag{2.2}$$

Assuming that ionization start at time t_i, and integrating equation (2.2) from t_i to t, we obtain:

$$v(t) = v_i - \frac{e\mathcal{E}_0}{m\omega_L}\left(\sin(\omega_L t) - \sin(\omega_L t_i)\right) = v_i + v_D - \frac{e\mathcal{E}_0}{m\omega_L}\sin(\omega_L t) \tag{2.3}$$

where $v_D = \frac{e\mathcal{E}_0}{m\omega_L}\sin(\omega_L t_i)$ is the *drift velocity* and v_i is the velocity at time t_i. If we integrate the (2.3) we obtain the position of electron:

$$z(t) = z_i + (v_i + v_D)(t - t_i) + \frac{e\mathcal{E}_0}{m\omega_L^2}\left(\cos(\omega_L t) - \cos(\omega_L t_i)\right). \tag{2.4}$$

The kinetic energy is:

$$E_{Kin}(t) = \frac{1}{2}mv(t)^2 = \frac{1}{2}m\left(v_i + v_D - \frac{e\mathcal{E}_0}{m\omega_L}\sin(\omega_L t)\right)^2. \tag{2.5}$$

The average kinetic energy in a period of the laser field is:

$$\langle E_{Kin}\rangle = \frac{1}{2}m(v_i + v_D)^2 + \frac{e^2\mathcal{E}_0^2}{4m\omega^2} = \frac{1}{2}(v_I + v_D)^2 + U_P, \tag{2.6}$$

where U_P is the *Ponderomotive Energy*. The potential ponderomotive energy is equal to the average energy of oscillation of the electron in the laser field.

Step III: Recombination

In this final step the electron recombines with the parent nucleus emitting high-energy photons. In particular the total energy is the sum of the ionization energy and the ponderomotive energy.

From equations 2.3 and 2.6 we can calculate the time of the electron collision and the corresponding kinetic energy. We can calculate the time collision by equating to zero the eq. 2.4

$$z(t_c) = z_i + (v_i + v_D)(t_c - t_i) + \frac{e\mathcal{E}_0}{m\omega_L^2}\left(\cos(\omega_L t_c) - \cos(\omega_L t_i)\right) = 0. \tag{2.7}$$

We can assume at the ionization instant that initial velocity and position are null because the laser oscillations are very large respect to the electron position and that only the electrons with small velocity after ionization can recombine with the nucleus. With these approximations the equations 2.7 and 2.5 become:

$$-\omega_L(t_c - t_i)\sin(\omega_L t_i) = \cos(\omega_L t_c) - \cos(\omega_L t_i) \tag{2.8}$$

$$E_{Kin}(t_c) = \frac{e^2\mathcal{E}_0^2}{2m\omega^2}\left(\sin(\omega_L t_c) - \sin(\omega_L t_i)\right)^2 \tag{2.9}$$

From these two equation we that the kinetic energy stems from the ionization instant t_i as well as from collision time t_c; and that t_c is a function of t_i:

$$t_c = f(t_i); \tag{2.10}$$

hence the electron collision energy depends from the ionization time:

$$E_{Kin}(t_i) = \frac{e^2\mathcal{E}_0^2}{2m\omega^2}\left[\sin\left(\omega_L f(t_i)\right) - \sin(\omega_L t_i)\right]^2. \tag{2.11}$$

In order to find the maximum oh this expression, we must to impose

$$\frac{dE_{Kin}(t)}{dt} = \frac{e^2\mathcal{E}_0^2}{2m\omega}\left[\sin(\omega_L f(t_i)) - \sin\left(\omega_L t_i\right)\right]\left[\cos\left(\omega_L f(t_i)\right)\frac{d}{dt_i}f(t_i) - \cos(\omega_L t_i)\right] = 0. \tag{2.12}$$

With numerical calculation we find the maximum for

$$\omega t \equiv 0.09\pi, 1.09\pi \tag{2.13}$$

that corresponds to

$$E_{Kin} = 3.17U_p. \tag{2.14}$$

Then when the electron recombines, we must sum all energy contributions:

$$E_{max} = E_I + 3.17U_p = \hbar\omega_{cutoff}. \tag{2.15}$$

In this way we can have a good evaluation of the cutoff position.

2.3 Strong Field Approximation (SFA)

The interaction of atoms and molecules with a laser field can be fruitfully described by using the strong field approximation. In the SFA the main assumption is that in the continuum the electron dynamic is dominated by the laser field and the nucleus potential is a weak perturbation that can be ignored at the lowest order [6].

Consider one atom in single active electron approximation driven by an intense laser field $\vec{\mathcal{E}}(t)$ and hence with a total Hamiltonian:

$$\mathcal{H} = -\frac{\hbar^2}{2m}\nabla^2 + V(\vec{r}) + e\vec{r}\cdot\vec{\mathcal{E}}(t) = \mathcal{H}_0 + e\vec{r}\cdot\vec{\mathcal{E}}(t), \tag{2.16}$$

where $\mathcal{H}_0$ is the free Hamiltonian and $V(\vec{r})$ is the coulombian interaction energy and $\vec{r}$ is the electron position. Then the Schrödinger equation of the system is given by

$$i\hbar\frac{\partial}{\partial t} \mid \Psi(t)\rangle = \left[\mathcal{H}_0 + e\vec{r}\cdot\vec{\mathcal{E}}(t)\right] \mid \Psi(t)\rangle \tag{2.17}$$

The ground state $\mid 0\rangle$ and the excited states $\mid e\rangle$ of the free Hamiltonian are:

$$\mathcal{H}_0 \mid 0\rangle = -I_p \mid 0\rangle \tag{2.18}$$

$$\mathcal{H}_0 \mid e\rangle = E_e \mid e\rangle \tag{2.19}$$

with I_p the ionization energy. Now we assume that the electron goes to the continuum by tunnel effect and that the electron in the continuum can be treated as a free particle and finally that the external laser field is very large such that the Keldysh parameter $\gamma = \sqrt{I_p/2U_p} < 1$. With these approximations, the wave function at time t can be expanded as

$$\mid t\rangle = e^{iI_p t}\left(\mid 0\rangle + \int d^3\vec{v}\, b(\vec{v},t) \mid \vec{v}\rangle\right) \tag{2.20}$$

with $\mid \vec{v}\rangle$ the atomic states in the continuum indicated by the kinetic momentum $\vec{v}$ and $b(\vec{v},t)$ its probability amplitude. Choosing an electric field along the x direction $\mathcal{E}_x = \mathcal{E}_0\cos(\omega t)$ and substituting this wave function into the Schrödinger equation and integrating over the time, we obtain the solution for $b(\vec{v},t)$:

$$b(\vec{v},t) = \int_0^t \mathbf{d}t' \mathcal{E}_0\cos(\omega t') d_x(\vec{v} + e\vec{A}(t) - e\vec{A}(t'))e^{-i\int_{t'}^{t}\mathbf{d}t''\left[\frac{(\vec{v}+e\vec{A}(t)-e\vec{A}(t''))^2}{2}+I_p\right]} \tag{2.21}$$

where d_x is the x component of the dipole moment matrix element $\vec{d}(\vec{v}) = -\langle \vec{v} \mid \vec{r} \mid 0 \rangle$, and $\vec{A}(t) = (-\mathcal{E}_0 \sin(t), 0, 0)$ is the vector potential of the external laser field. The equation 2.21 can be divided in two parts, in the first one the the term $\mathcal{E}_0 \cos(\omega t') d_x(\vec{v} + e\vec{A}(t) - e\vec{A}(t'))$ represents the probability amplitude to find the electron in the continuum with canonical momentum $\vec{p} = \vec{v} + e\vec{A}(t)$, and the exponential term describe the free propagation of the electron in the laser field from the time t' to the time t and represents the quasiclassical action.

Then if $\vec{p}$ is the canonical momentum, we can write the quasiclassical action as

$$S(\vec{p}, t, t') = \int_{t'}^{t} \mathbf{d}t'' \left(\frac{\left(\vec{p} - e\vec{A}(t'')\right)^2}{2} + I_p \right). \tag{2.22}$$

In order to calculate the x component of the time dependent dipole moment, it is necessary calculate $x(t) = \langle \Psi(t) \mid x \mid \Psi(t) \rangle$:

$$x(t) = i \int_0^t \mathbf{d}t' \int \mathbf{d}^3\vec{p} \quad \mathcal{E}_0 \cos(t') d_x(\vec{p} - e\vec{A}(t')) d_x^*(\vec{p} - e\vec{A}(t)) e^{-iS(\vec{p},t,t')} + c.c \tag{2.23}$$

where the matrix element $d_x^*(\vec{p} - e\vec{A}(t)) = \langle 0 \mid x \mid \vec{p} - e\vec{A}(t) \rangle$ is proportional to the probability that the electron recollide to the nucleus at time t. The integration over $d^3\vec{p}$ is equivalent to the sum over all possible values of $\vec{p}$ but Lewenstein [6] demonstrate that only the electron that at the exit of tunneling have a velocity close to zero can recollide with the nucleus. This is the main feature of the SFA.

2.4 High Harmonic Spectrum

In this section we show the typical high harmonic spectrum.

The spectrum can be divided in three regions: in the first region, typically the first ten harmonics, we have a decay of the harmonic intensities that become constants in the second region called plateau. Finally in the last region we have a cutoff, were we have a fast decay of the harmonic intensities. This is clearly a non-linear process.

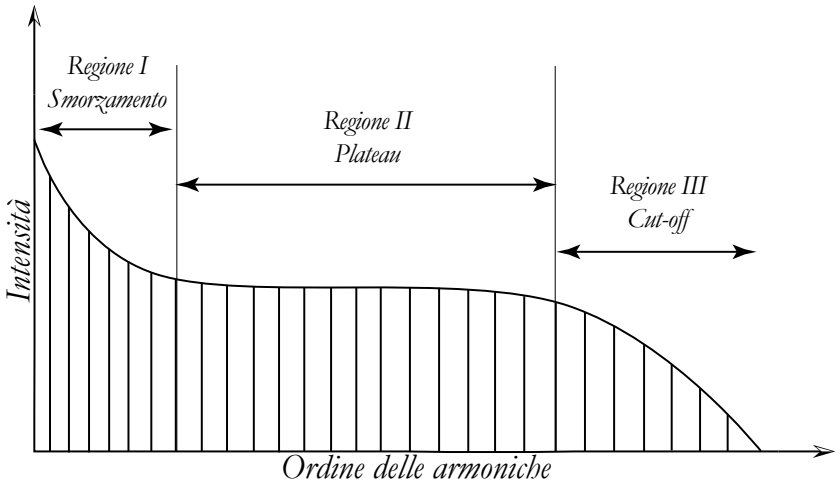

Figure 2.2: Typical high harmonic spectrum.

We can use several alternatives in order to calculate the harmonic spectrum. In particular:

- Electronic trajectory in three steps regime
- Fourier transform of the dipole moment of the electron
- Acceleration of the electron

The use of one method instead another is due to the mathematical convenience of the system to be studied. In order to explain the three methods, we will show the results obtained for a nanoring driven by a two color laser field and we will compare them.

2.5 Electronic trajectory in three steps regime

In order to explain the electronic trajectory in three steps regime , we give the example of the ionization of one atom in which the electron is ionized and then recollide with core. In this system we consider a two color elliptically polarized electric field:

$$\vec{\mathcal{E}}(t) = \frac{1}{2i}\left[\frac{\mathcal{E}_1}{\sqrt{1+\epsilon_1^2}}\left(\hat{e}_1 - i\epsilon_1\hat{e}_2\right)e^{i\omega t} + \frac{\mathcal{E}_2}{\sqrt{1+\epsilon_2^2}}\left(\hat{e}_1 - i\epsilon_2\hat{e}_2\right)e^{i2\omega t}\right] + c.c. \quad (2.24)$$

with $\epsilon_j \in [-1,1]$ the ellipticity of the laser field, $E_{1,2}$ its amplitude and $\hat{e}_{1,2}$ the versor. The vector potential is

$$\vec{A}(t) = -\int^t \vec{\mathcal{E}}(t')dt'. \tag{2.25}$$

Also we define

$$\vec{\alpha}(t) = \frac{e}{m}\int^t \vec{A}(t')dt' \qquad (e =\mid e \mid). \tag{2.26}$$

The rate emission of the n-th harmonic with polarization $\hat{e}_j$ is given by the equation

$$w_n(\hat{e}_j) = \frac{1}{8\pi^2\epsilon_0\hbar}\left(\frac{n\omega}{c}\right)^3 \mid T_n(\hat{e}_j \mid^2, \tag{2.27}$$

where the element of the matrix t are calculated with the equation

$$T_n(\hat{e}_j) = \int_{t_0}^{t_0+T} \frac{1}{T}\hat{e}_j^*\vec{d}(t_f)e^{in\omega t_f}dt_f \tag{2.28}$$

with t_0 the initial time and $T = 2\pi/\omega$. In strong field approximation (SFA) the matrix elements of the dipole moment $\vec{d}(t_f)$can be approximated as

$$\begin{aligned}\vec{d}(t_f) &= -\frac{i}{\hbar}\int \langle\psi_0 \mid e\vec{r} \mid \vec{q} + \frac{e}{\hbar}\vec{A}(t_f)\rangle d^3\vec{q}\cdot \\ &\cdot \int_{-\infty}^{t_f} dt_i \langle\vec{q} + \frac{e}{\hbar}\vec{A}(t_i) \mid e\vec{r}\cdot\vec{\mathcal{E}}(t_i) \mid \psi_0\rangle \cdot \\ &\cdot e^{-\frac{i}{2m\hbar}\int_{t_i}^{t_f}[\hbar\vec{q}+e\vec{A}(t)]^2dt + \frac{i}{\hbar}E_0(t_f-t_i)}.\end{aligned} \tag{2.29}$$

If we join the all the exponential terms into the quasiclassical equation, we obtain the following action:

$$S(\vec{q},t_i,t_f) = \frac{1}{2m}\int_{t_i}^{t_f}[\hbar\vec{q}+e\vec{A}(t)]^2dt + \int_{t_f}^{t_i} E_0dt + \int_{t_f}^{\infty} n\hbar\omega dt = \tag{2.30}$$

$$= \int_{t_f}^{\infty}(E_0+n\hbar\omega)dt + \frac{1}{2m}\int_{t_i}^{t_f}[\hbar\vec{q}+e\vec{A}(t)]^2dt + \int_{-\infty}^{t_i} E_0dt. \tag{2.31}$$

Initially the atom is in the ground state:

$$\mid\psi_0\rangle e^{-\frac{i}{\hbar}E_0t} \tag{2.32}$$

At time t_i the electron goes to the continuum, in tunnel regime, because the interaction $e\vec{r}\vec{\mathcal{E}}(t_i)$. At time $t < t_i$ the system is in the ground state, finally at time t_f the

electron returns to the starting point recombining with the nucleus and emitting a laser photon with energy $n\hbar\omega$. The T matrix (eq. 2.28), can be calculated with the saddle point method:

$$T_n(\hat{e}_j) \propto \sum_s M_s \frac{e^{-\frac{i}{\hbar}S_s}}{\sqrt{\det\left(\frac{\partial^2 S}{\partial q_k \partial q_\ell}\right)}}, \tag{2.33}$$

where $S_s \equiv S(\vec{q}_s, t_{is}, t_{fs})$ is the action calculated in the sallde points s and $M_s \equiv M(\vec{q}_s, t_{is}, t_{fs})$ is the product of the non exponential terms of the dipole moment matrix element in Eq. 2.29. The saddle point are the solution of the following equations:

$$\begin{aligned}
\frac{m}{t_f - t_i}\left[\vec{\alpha}(t_i) - \alpha(\vec{t}_f)\right] &= \hbar\vec{q} && (2.34)\\
\frac{1}{2m}[\hbar\vec{q} + e\vec{A}(t_i)]^2 &= E_0 && (2.35)\\
\frac{1}{2m}[\hbar\vec{q} + e\vec{A}(t_f)]^2 &= n\hbar\omega + E_0 && (2.36)
\end{aligned}$$

At first we need to find the initial time saddle point t_{is}. We set:

$$A(t) = \frac{\sin(\omega t_i)}{\omega}, \tag{2.37}$$

in the Eq. 2.35:

$$\frac{1}{2m}\left[\hbar^2 q^2 + 2\hbar\vec{q}e\vec{A}(t_i) + e^2 A(t_i)^2\right] = E_0 \tag{2.38}$$

$$\frac{1}{2m}\left[\hbar^2 q^2 + 2\hbar\vec{q}e\frac{\sin(\omega t_i)}{\omega} + e^2\frac{\sin(\omega t_i)^2}{\omega^2}\right] = E_0 \tag{2.39}$$

$$\hbar^2 q^2 + 2\hbar\vec{q}e\frac{\sin(\omega t_i)}{\omega} + e^2\frac{\sin(\omega t_i)^2}{\omega^2} - 2mE_0 = 0 \tag{2.40}$$

$$\frac{\sin(\omega t_i)^2}{\omega^2} + \frac{2\hbar\vec{q}}{e}\frac{\sin(\omega t_i)}{\omega} - \frac{2mE_0 - \hbar^2 q^2}{e^2} = 0 \tag{2.41}$$

$$\sin(\omega t_i)^2 + \frac{2\hbar\omega\vec{q}}{e}\sin(\omega t_i) - \left(2mE_0 - \hbar^2 q^2\right)\omega^2 = 0 \tag{2.42}$$

hence we have

$$\begin{aligned}
\sin(\omega t_i) &= -\frac{\hbar\omega\vec{q}}{e} \pm \frac{1}{2}\sqrt{\left(\frac{2\hbar\omega\vec{q}}{e}\right)^2 + 4\omega^2\frac{2mE_0 - \hbar^2 q^2}{e^2}}\\
&= -\frac{\hbar\omega\vec{q}}{e} \pm \frac{\omega}{e}\sqrt{2mE_0} && (2.43)
\end{aligned}$$

$$= -\frac{\omega}{e}\left(\hbar\vec{q} \pm \sqrt{2mE_0}\right) \tag{2.44}$$

Then we have four solutions:

$$\omega t_{is1} = \arcsin\left[-\frac{\omega}{e}\left(\hbar\vec{q} + \sqrt{2mE_0}\right)\right] \tag{2.45}$$

$$\omega t_{is2} = \pi + \arcsin\left[-\frac{\omega}{e}\left(\hbar\vec{q} + \sqrt{2mE_0}\right)\right] \tag{2.46}$$

$$\omega t_{is3} = \arcsin\left[-\frac{\omega}{e}\left(\hbar\vec{q} - \sqrt{2mE_0}\right)\right] \tag{2.47}$$

$$\omega t_{is4} = \pi + \arcsin\left[-\frac{\omega}{e}\left(\hbar\vec{q} - \sqrt{2mE_0}\right)\right] \tag{2.48}$$

Similarly from the Eq. 2.36 we find the final time saddle point t_{fs}:

$$\omega t_{fs1} = \arcsin\left[-\frac{\omega}{e}\left(\hbar\vec{q} + \sqrt{2m\left(n\hbar\omega + E_0\right)}\right)\right] \tag{2.49}$$

$$\omega t_{fs2} = \pi + \arcsin\left[-\frac{\omega}{e}\left(\hbar\vec{q} + \sqrt{2m\left(n\hbar\omega + E_0\right)}\right)\right] \tag{2.50}$$

$$\omega t_{fs3} = \arcsin\left[-\frac{\omega}{e}\left(\hbar\vec{q} - \sqrt{2m\left(n\hbar\omega + E_0\right)}\right)\right] \tag{2.51}$$

$$\omega t_{fs4} = \pi + \arcsin\left[-\frac{\omega}{e}\left(\hbar\vec{q} - \sqrt{2m\left(n\hbar\omega + E_0\right)}\right)\right] \tag{2.52}$$

Now we must calculate the electron motion into the laser field by the classical Newton equation: $m\vec{a}(t) = -e\vec{\mathcal{E}}(t)$. The solution of this equation with the initial condition $\vec{r}(t_i) = \vec{r}_i$ e $\vec{v}(t_i) = \vec{v}_i$ is:

$$m\vec{v}(t) = e\left[\vec{A}(t) - \vec{A}(t_i)\right] + m\vec{v}_i \tag{2.53}$$

$$\vec{r}(t) = \vec{r}_i + \vec{\alpha}(t) - \vec{\alpha}(t_i) - \left[\frac{e}{m}\vec{A}(t_i) - \vec{v}_i\right](t - t_i). \tag{2.54}$$

Using the recollision condition in the starting point $\vec{r}(t_f) = r_i$ we have

$$m\frac{\vec{\alpha}(t_i) - \vec{\alpha}(t_f)}{t_f - t_i} = m\vec{v}_i - e\vec{A}(t_i) = \vec{p}, \tag{2.55}$$

this equation is in agreement with Eq. 2.34. Because the energy conservation condition in Eq. 2.35, the initial kinetic energy of the electron into the laser field must be equal to the its final energy in the atomic ground state:

$$\frac{1}{2}m\vec{v}_i^2 = E_0. \tag{2.56}$$

This requirement can be satisfied with a complex velocity $\vec{v}_i$ such as:

$$\Re(\vec{v}_i) \cdot \Im(\vec{v}_i) = 0 \tag{2.57}$$

$$\Re(\vec{v}_i)^2 - \Im(\vec{v}_i)^2 = \frac{2E_0}{m} \tag{2.58}$$

Similarly for the energy conservation at final time t_f:

$$\frac{1}{2}m\vec{v}(t_f)^2 = n\hbar\omega + E_0, \tag{2.59}$$

the final electron velocity must satisfy the conditions:

$$\Re(\vec{v}(t_f)) \cdot \Im(\vec{v}(t_f)) = 0 \tag{2.60}$$

$$\Re(\vec{v}(t_f))^2 - \Im(\vec{v}(t_f))^2 = \frac{2(n\hbar\omega + E_0)}{m}. \tag{2.61}$$

Complex time and velocity are the consequence of the fact that the electron arises from the tunneling. Now we can calculate the harmonic spectra by the Fourier transform of the Eq. 2.54 or by the calculation of the electron acceleration. These two method are studied in the following two sections.

2.5.1 FFT of the dipole moment of the electron

Another method to obtain the harmonic spectrum is by the Fourier transform of the dipole momentum. We consider a system composed by one electron constrained over a circle of radius R driven by two laser fields along its plane (the $x-y$ plane), with angular frequency ω_x and $\omega_y = 2\omega_x$. The laser along the x axis is taken n-photon resonant between the ground state and the first excited state.

We write the total electric field as:

$$\vec{\mathcal{E}}_L(t) = \mathcal{E}_0\Big[\hat{\epsilon}_x f_x(t)\cos(\beta)\cos(\omega_x t) + \hat{\epsilon}_y f_y(t)\sin(\beta)\sin(\omega_y t)\Big] \tag{2.62}$$

where $\mathcal{E}_0$ is the total amplitude of the electric field and $f_k(t)$ the shapes of the two laser pulses. The convenient parameter β sets the intensity of the two lasers and leaves unchanged the total intensity; for $\beta = 0°$ we have only the electric field along the x axis, for $\beta = 45°$ the two electric fields have the same intensity and finally for $\beta = 90°$ we have only the second electric field.

The Hamiltonian of the system is:

$$\mathcal{H} = \mathcal{H}_0 + e\mathcal{E}_{0x}R\cos(\theta)f_x(t)\cos(\omega_x t) + e\mathcal{E}_{0y}R\sin(\theta)f_y(t)\sin(\omega_y t), \quad (2.63)$$

where R is the radius of the nanoring, θ is the angle between the electron position and the x axis, $\mathcal{E}_{0x} = \mathcal{E}_0\cos(\beta)$, $\mathcal{E}_{0y} = \mathcal{E}_0\sin(\beta)$ and $\mathcal{H}_0$ is the Hamiltonian in absence of external laser fields:

$$\mathcal{H}_0 = -\frac{\hbar^2}{2m_e}\nabla^2 = -\frac{\hbar^2}{2m_e r^2}\left[\frac{\partial}{\partial r}\left(r^2\frac{\partial}{\partial r}\right) - \hat{\ell}^2\right]. \quad (2.64)$$

where m_e is the mass of electron and ℓ is the operator of the orbital angular momentum. Since r is constant, the derivatives over r will vanish:

$$\mathcal{H}_0 = \frac{\hbar^2}{2m_e R^2}\hat{\ell}^2. \quad (2.65)$$

But $\hat{\ell}^2 = \hat{\ell}_x^2 + \hat{\ell}_y^2 + \hat{\ell}_z^2$, and the symmetry of the system permit us to write the free Hamiltonian as

$$\mathcal{H}_0 = \frac{\hbar^2}{2m_e R^2}\hat{\ell}_z^2 \quad (2.66)$$

with ℓ_z the z component of the angular momentum operator in units of $\hbar$.

If we solve the time dependent Schrödinger equation we find the expansion coefficients a_m of the wave function $\mid t\rangle$:

$$\mid t\rangle = \sum_{m,-\infty}^{+\infty} a_m(t) \mid m\rangle \quad (2.67)$$

where $\mid m\rangle = e^{im\varphi}/\sqrt{2\pi}$ are eigenstates of $\mathcal{H}_0$.
The equation we arrive at is:

$$\begin{aligned} i\dot{a}_m &= \omega_m a_m + \frac{e\mathcal{E}_0 R}{2\hbar}\{[\cos(\beta)\, f_x(t)\cos(\omega_x t) - i\sin(\beta)\, f_y(t)\sin(\omega_y t)]a_{m-1} + \\ &+ [\cos(\beta)\, f_x(t)\cos(\omega_x t) + i\sin(\beta)\, f_y(t)\sin(\omega_y t)]a_{m+1}\}. \end{aligned} \quad (2.68)$$

thus we have a set of coupled differential equations. From the state $\mid t\rangle$ we calculate the dipole moment $\vec{\mathcal{D}}$. The emitted spectrum of high harmonics will be the Fourier transform of the dipole momentum.

$$\vec{\mathcal{D}} = \sum_{m,-\infty}^{+\infty}\left[\hat{\epsilon}_x\Re\left(a_{m-1}^* a_m\right) + \hat{\epsilon}_y\Im\left(a_m^* a_{m-1}\right)\right]. \quad (2.69)$$

2.5.2 Acceleration of the electron

The last method to calculate the harmonic spectrum is by the calculation of the electron acceleration. We consider a system composed by one nanoring driven by a laser field; the Hamiltonian, and the full state of the charge carrier in the ring are the same of the past section. In this manner, the time dependent Schroedinger equation (TDSE)

$$i\hbar\partial_t|t\rangle = \mathcal{H}|t\rangle, \tag{2.70}$$

and

$$\begin{aligned} \mathcal{H} \mid t\rangle &= \sum_{n=-\infty}^{\infty} \hbar\omega_n c_n \mid n\rangle + V_x f_x(t)\sin(\omega_L t)\sum_{n=-\infty}^{\infty} c_n\cos(\theta) \mid n\rangle & (2.71)\\ &+ V_y f_y(t)\sin(\omega_L t)\sum_{n=-\infty}^{\infty} c_n\sin(\theta) \mid n\rangle & (2.72) \end{aligned}$$

with $V_i = e\mathcal{E}_{0i}R, i = x, y$, the potential energy of the charge carrier.

If we project $\langle m \mid$ state, we obtain:

$$\begin{aligned} i\hbar\dot{c}_m &= \hbar\omega_m c_m + V_x f_x(t)\sin(\omega_L t)\sum_{n=-\infty}^{\infty} c_n\langle m \mid \cos(\theta) \mid n\rangle \\ &+ V_y f_y(t)\sin(\omega_L t)\sum_{n=-\infty}^{\infty} c_n\langle m \mid \sin(\theta) \mid n\rangle \end{aligned} \tag{2.73}$$

$$\begin{aligned} -i\hbar\dot{c}^*_m &= \hbar\omega_m c^*_m + V_x f_x(t)\sin(\omega_L t)\sum_{n=-\infty}^{\infty} c^*_n\langle m \mid \cos(\theta) \mid n\rangle \\ &+ +V_y f_y(t)\sin(\omega_L t)\sum_{n=-\infty}^{\infty} c^*_n\langle m \mid \sin(\theta) \mid n\rangle \end{aligned} \tag{2.74}$$

We set

$$u_{mn} = \langle m \mid \cos(\theta) \mid n\rangle = \frac{1}{2}\left(\delta_{m-n+1,0} + \delta_{m-n-1,0}\right). \tag{2.75}$$

where $u_{mn} \in \Re$, then $u_{mn} = u^*_{mn}$.

Likewise we have

$$v_{mn} = \langle m \mid \sin(\theta) \mid n \rangle = \frac{i}{2} \left(\delta_{m-n+1,0} - \delta_{m-n-1,0} \right). \tag{2.76}$$

Then the equation 2.73 will be

$$\begin{aligned} i\hbar \dot{c}_m &= \hbar\omega_m c_m + V_x f_x(t) \sin(\omega_L t) \sum_{n=-\infty}^{\infty} u_{mn} c_n \\ &+ V_y f_y(t) \sin(\omega_L t) \sum_{n=-\infty}^{\infty} v_{mn} c_n. \end{aligned} \tag{2.77}$$

The x and y positions of the charge carrier are

$$\begin{aligned} x(t) &= \langle t \mid x \mid t \rangle = \langle t \mid R\cos(\theta) \mid t \rangle \\ &= R \sum_{n,m=-\infty}^{\infty} c_m^* c_n \langle m \mid \cos(\theta) \mid n \rangle = R \sum_{n,m=-\infty}^{\infty} u_{mn} c_m^* c_n \end{aligned} \tag{2.78}$$

$$\begin{aligned} y(t) &= \langle t \mid y \mid t \rangle = \langle t \mid R\sin(\theta) \mid t \rangle \\ &= R \sum_{n,m=-\infty}^{\infty} c_m^* c_n \langle m \mid \sin(\theta) \mid n \rangle = R \sum_{n,m=-\infty}^{\infty} v_{mn} c_m^* c_n \end{aligned} \tag{2.79}$$

If we set $S_{mni} = c_m^* c_n$, ,with $i = x, y$, then we define:

$$i\hbar \dot{S}_{mni} = i\hbar(\dot{c}_m^* c_n + c_m^* \dot{c}_n) = \tag{2.80}$$

$$\begin{aligned} &= \left(-\hbar\omega_m c_m^* - V_i F(t)_i \sin(\omega_L t) \sum_{k=-\infty}^{\infty} u_{mk}^* c_k^* \right) c_n + \\ &+ c_m^* \left(\hbar\omega_n c_n + V_i F(t)_i \sin(\omega_L t) \sum_{k=-\infty}^{\infty} u_{nk} c_k \right) \end{aligned} \tag{2.81}$$

setting $\omega_{nm} = \omega_n - \omega_m$ we obtain:

$$i\hbar \dot{S}_{mnx} = \hbar\omega_{nm} c_m^* c_n - V_x f_x(t) \sin(\omega_L t) \sum_{k=-\infty}^{\infty} \left[u_{mk}^* c_k^* c_n - u_{nk} c_m^* c_k \right] \tag{2.82}$$

$$= \hbar\omega_{nm} c_m^* c_n - V_x f_x(t) \sin(\omega_L t) \sum_{k=-\infty}^{\infty} \left[u_{mk}^* S_{kn} - u_{nk} S_{mk} \right] \tag{2.83}$$

$$i\hbar \dot{S}_{mny} = \hbar\omega_{nm} c_m^* c_n - V_y f_y(t) \sin(\omega_L t) \sum_{k=-\infty}^{\infty} \left[v_{mk}^* c_k^* c_n - v_{nk} c_m^* c_k \right] \tag{2.84}$$

$$= \hbar\omega_{nm} c_m^* c_n - V_y f_y(t) \sin(\omega_L t) \sum_{k=-\infty}^{\infty} \left[v_{mk}^* S_{kn} - v_{nk} S_{mk} \right]. \tag{2.85}$$

Then the velocities will be:

$$i\hbar \dot{x}(t) = i\hbar R \sum_{n,m=-\infty}^{\infty} u_{mn} \dot{S}_{mnx} \tag{2.86}$$

$$i\hbar\dot{y}(t) = i\hbar R \sum_{n,m=-\infty}^{\infty} v_{mn}\dot{S}_{mny} \tag{2.87}$$

with

$$\begin{aligned} u_{mn}u_{nk} &= \frac{1}{4}\left(\delta_{m-n+1,0} + \delta_{m-n-1,0}\right)\left(\delta_{n-k+1,0} + \delta_{n-k-1,0}\right) \qquad (2.88)\\ &= \frac{1}{4}\left(\delta_{m-n+1,0}\delta_{n-k+1,0} + \delta_{m-n+1,0}\delta_{n-k-1,0} + \delta_{m-n-1,0}\delta_{n-k+1,0} + \delta_{m-n-1,0}\delta_{n-k-1,0}\right) \end{aligned}$$

$$\begin{aligned} u_{mn}u^*_{mk} &= u_{mn}u_{km} = \frac{1}{4}\left(\delta_{m-n+1,0} + \delta_{m-n-1,0}\right)\left(\delta_{k-m+1,0} + \delta_{k-m-1,0}\right) \qquad (2.89)\\ &= \frac{1}{4}\left(\delta_{m-n+1,0}\delta_{k-m+1,0} + \delta_{m-n+1,0}\delta_{k-m-1,0} + \delta_{m-n-1,0}\delta_{k-m+1,0} + \delta_{m-n-1,0}\delta_{k-m-1,0}\right) \end{aligned}$$

$$\begin{aligned} v_{mn}v_{nk} &= -\frac{1}{4}\left(\delta_{m-n+1,0} - \delta_{m-n-1,0}\right)\left(\delta_{n-k+1,0} - \delta_{n-k-1,0}\right) \qquad (2.90)\\ &= -\frac{1}{4}\left(\delta_{m-n+1,0}\delta_{n-k+1,0} - \delta_{m-n+1,0}\delta_{n-k-1,0} - \delta_{m-n-1,0}\delta_{n-k+1,0} + \delta_{m-n-1,0}\delta_{n-k-1,0}\right) \end{aligned}$$

$$\begin{aligned} v_{mn}v^*_{mk} &= -v_{mn}v_{km} = \frac{1}{4}\left(\delta_{m-n+1,0} - \delta_{m-n-1,0}\right)\left(\delta_{k-m+1,0} - \delta_{k-m-1,0}\right) \qquad (2.91)\\ &= \frac{1}{4}\left(\delta_{m-n+1,0}\delta_{k-m+1,0} - \delta_{m-n+1,0}\delta_{k-m-1,0} - \delta_{m-n-1,0}\delta_{k-m+1,0} + \delta_{m-n-1,0}\delta_{k-m-1,0}\right) \end{aligned}$$

Then the velocities:

$$i\hbar\dot{x}(t) = i\hbar R \sum_{n,m=-\infty}^{\infty} u_{mn}\dot{S}_{mnx} \tag{2.92}$$

$$\begin{aligned} &= \hbar R \sum_{n,m=-\infty}^{\infty} u_{mn}\omega_{nm}c^*_m c_n - RV_x f_x(t)\sin(\omega_L t)\cdot\\ &\cdot \sum_{n,m=-\infty}^{\infty} u_{mn} \sum_{k=-\infty}^{\infty}\left[u^*_{mk}c^*_k c_n - u_{nk}c^*_m c_k\right] \qquad (2.93)\\ &= \frac{\hbar R}{2}\sum_{n=-\infty}^{\infty}\left(\omega_{n,n-1}c^*_{n-1} + \omega_{n,n+1}c^*_{n+1}\right)c_n -\\ &- RV_x f_x(t)\sin(\omega_L t)\sum_{n,m=-\infty}^{\infty}\sum_{k=-\infty}^{\infty}\left[u_{mn}u^*_{mk}c^*_k c_n - u_{mn}u_{nk}c^*_m c_k\right] \qquad (2.94) \end{aligned}$$

$$
\begin{aligned}
&= \frac{\hbar R}{2}\sum_{n=-\infty}^{\infty}\left(\omega_{n,n-1}c_{n-1}^{*}+\omega_{n,n+1}c_{n+1}^{*}\right)c_n-\frac{1}{4}RV_xf_x(t)\sin(\omega_Lt)\cdot\\
&\cdot\ \sum_{n,m=-\infty}^{\infty}\sum_{k=-\infty}^{\infty}\Big[\left(\delta_{m-n+1,0}\delta_{k-m+1,0}+\delta_{m-n+1,0}\delta_{k-m-1,0}+\right.\\
&+\ \left.\delta_{m-n-1,0}\delta_{k-m+1,0}+\delta_{m-n-1,0}\delta_{k-m-1,0}\right)c_k^{*}c_n-\\
&-\ \left(\delta_{m-n+1,0}\delta_{n-k+1,0}+\delta_{m-n+1,0}\delta_{n-k-1,0}+\right.\\
&+\ \left.\delta_{m-n-1,0}\delta_{n-k+1,0}+\delta_{m-n-1,0}\delta_{n-k-1,0}\right)c_m^{*}c_k\Big] \qquad (2.95)\\
&= \frac{\hbar R}{2}\sum_{n=-\infty}^{\infty}\left(\omega_{n,n-1}c_{n-1}^{*}+\omega_{n,n+1}c_{n+1}^{*}\right)c_n-\frac{1}{4}RV_xf_x(t)\sin(\omega_Lt)\sum_{n,m=-\infty}^{\infty}\cdot\\
&\cdot\ \Big[\left(\delta_{m-n+1,0}c_{m-1}^{*}+\delta_{m-n+1,0}c_{m+1}^{*}+\delta_{m-n-1,0}c_{m-1}^{*}+\delta_{m-n-1,0}c_{m+1}^{*}\right)c_n-\\
&-\ c_m^{*}\left(\delta_{m-n+1,0}c_{n+1}+\delta_{m-n+1,0}c_{n-1}+\delta_{m-n-1,0}c_{n+1}+\delta_{m-n-1,0}c_{n-1}\right)\Big] \qquad (2.96)\\
&= \frac{\hbar R}{2}\sum_{n=-\infty}^{\infty}\left(\omega_{n,n-1}c_{n-1}^{*}+\omega_{n,n+1}c_{n+1}^{*}\right)c_n-\\
&-\ \frac{RV_xf_x(t)\sin(\omega_Lt)}{4}\sum_{n=-\infty}^{\infty}\Big[\left(c_{n-2}^{*}+2c_n^{*}+c_{n+2}^{*}\right)c_n-\\
&-\ c_{n-1}^{*}\left(c_{n-1}+c_{n+1}\right)-c_{n+1}^{*}\left(c_{n-1}+c_{n+1}\right)\Big] \qquad (2.97)\\
&= \frac{\hbar R}{2}\sum_{n=-\infty}^{\infty}\left(\omega_{n,n-1}S_{n-1,n,x}+\omega_{n,n+1}S_{n+1,n,x}\right)-\\
&-\ \frac{RV_xf_x(t)\sin(\omega_Lt)}{4}\sum_{n=-\infty}^{\infty}\Big[S_{n-2,n,x}+2S_{n,n,x}+S_{n+2,n,x}-S_{n-1,n-1,x}-\\
&-\ S_{n-1,n+1,x}-S_{n+1,n-1,x}-S_{n+1,n+1,x}\Big] \qquad (2.98)
\end{aligned}
$$

$$
\begin{aligned}
&i\hbar\dot{y}(t)=i\hbar R\sum_{n,m=-\infty}^{\infty}v_{mn}\dot{S}_{mny} \qquad (2.99)\\
&= \hbar R\sum_{n,m=-\infty}^{\infty}v_{mn}\omega_{nm}c_m^{*}c_n-RV_yf_y(t)\sin(\omega_Lt)\cdot\\
&\cdot\ \sum_{n,m=-\infty}^{\infty}v_{mn}\sum_{k=-\infty}^{\infty}\left[v_{mk}^{*}c_k^{*}c_n-v_{nk}c_m^{*}c_k\right] \qquad (2.100)\\
&= \frac{\hbar R}{2}\sum_{n=-\infty}^{\infty}\left(\omega_{n,n-1}c_{n-1}^{*}-\omega_{n,n+1}c_{n+1}^{*}\right)c_n-RV_yf_y(t)\cdot\\
&\cdot\ \sin(\omega_Lt)\sum_{n,m=-\infty}^{\infty}\sum_{k=-\infty}^{\infty}\left[v_{mn}v_{mk}^{*}c_k^{*}c_n-v_{mn}v_{nk}c_m^{*}c_k\right] \qquad (2.101)
\end{aligned}
$$

$$
\begin{aligned}
&= \frac{\hbar R}{2}\sum_{n=-\infty}^{\infty}\left(\omega_{n,n-1}c^*_{n-1}-\omega_{n,n+1}c^*_{n+1}\right)c_n-\frac{1}{4}RV_yf_y(t)\sin(\omega_Lt)\cdot\\
&\cdot\ \sum_{n,m=-\infty}^{\infty}\sum_{k=-\infty}^{\infty}\Big[\left(\delta_{m-n+1,0}\delta_{k-m+1,0}-\delta_{m-n+1,0}\delta_{k-m-1,0}-\right.\\
&-\ \left.\delta_{m-n-1,0}\delta_{k-m+1,0}+\delta_{m-n-1,0}\delta_{k-m-1,0}\right)c^*_kc_n+\\
&+\ \left(\delta_{m-n+1,0}\delta_{n-k+1,0}-\delta_{m-n+1,0}\delta_{n-k-1,0}-\delta_{m-n-1,0}\delta_{n-k+1,0}+\right.\\
&+\ \left.\delta_{m-n-1,0}\delta_{n-k-1,0}\right)c^*_mc_k\Big] \qquad (2.102)\\
&= \frac{\hbar R}{2}\sum_{n=-\infty}^{\infty}\left(\omega_{n,n-1}c^*_{n-1}+\omega_{n,n+1}c^*_{n+1}\right)c_n-\frac{1}{4}RV_yf_y(t)\sin(\omega_Lt)\sum_{n,m=-\infty}^{\infty}\cdot\\
&\cdot\ \Big[\left(\delta_{m-n+1,0}c^*_{m-1}-\delta_{m-n+1,0}c^*_{m+1}-\delta_{m-n-1,0}c^*_{m-1}+\delta_{m-n-1,0}c^*_{m+1}\right)c_n+\\
&+\ c^*_m\left(\delta_{m-n+1,0}c_{n+1}-\delta_{m-n+1,0}c_{n-1}-\delta_{m-n-1,0}c_{n+1}+\delta_{m-n-1,0}c_{n-1}\right)\Big] \qquad (2.103)\\
&= \frac{\hbar R}{2}\sum_{n=-\infty}^{\infty}\left(\omega_{n,n-1}c^*_{n-1}-\omega_{n,n+1}c^*_{n+1}\right)c_n-\frac{RV_yf_y(t)\sin(\omega_Lt)}{4}\cdot\\
&\cdot\ \sum_{n=-\infty}^{\infty}\Big[\left(c^*_{n-2}-2c^*_n+c^*_{n+2}\right)c_n+c^*_{n-1}\left(c_{n+1}-c_{n-1}\right)+c^*_{n+1}\left(c_{n-1}-c_{n+1}\right)\Big]\\
&= \frac{\hbar R}{2}\sum_{n=-\infty}^{\infty}\left(\omega_{n,n-1}S_{n-1,n,y}-\omega_{n,n+1}S_{n+1,n,y}\right)+\\
&+\ \frac{RV_yf_y(t)\sin(\omega_Lt)}{4}\sum_{n=-\infty}^{\infty}\Big[S_{n-2,n,y}-2S_{n,n,y}+S_{n+2,n,y}+S_{n-1,n+1,y}-\\
&-\ S_{n-1,n-1,y}+S_{n+1,n-1,y}-S_{n+1,n+1,y}\Big] \qquad (2.104)
\end{aligned}
$$

With a second time differentiation, we obtain the accelerations along x and y.

For the x acceleration we must calculate:

$$
\begin{aligned}
&\frac{d}{dt}\Big[\frac{\hbar R}{2}\sum_{n=-\infty}^{\infty}\left(\omega_{n,n-1}S_{n-1,n,x}+\omega_{n,n+1}S_{n+1,n,x}\right)\Big]= \qquad (2.105)\\
&\qquad\frac{\hbar R}{2}\sum_{n=-\infty}^{\infty}\left(\omega_{n,n-1}\dot{S}_{n-1,n,x}+\omega_{n,n+1}\dot{S}_{n+1,n,x}\right) \qquad (2.106)
\end{aligned}
$$

$$
\begin{aligned}
\frac{d}{dt}\ &\Big[-\frac{RV_xf_x(t)\sin(\omega_Lt)}{4}\sum_{n=-\infty}^{\infty}\Big(S_{n-2,n,x}+2S_{n,n,x}+S_{n+2,n,x}-\\
&-\ S_{n-1,n-1,x}-S_{n-1,n+1,x}-S_{n+1,n-1,x}-S_{n+1,n+1,x}\Big)\Big]= \qquad (2.107)\\
&= -\frac{RV_xf_x(t)\omega_L\cos(\omega_Lt)}{4}\sum_{n=-\infty}^{\infty}\Big(S_{n-2,n,x}+2S_{n,n,x}+S_{n+2,n,x}-
\end{aligned}
$$

$$
\begin{aligned}
- \quad & S_{n-1,n-1,x} - S_{n-1,n+1,x} - S_{n+1,n-1,x} - S_{n+1,n+1,x}\Big) - \\
- \quad & \frac{RV_x\dot{f}_x(t)\sin(\omega_L t)}{4}\sum_{n=-\infty}^{\infty}\Big(S_{n-2,n,x} + 2S_{n,n,x} + S_{n+2,n,x} - \\
- \quad & S_{n-1,n-1,x} - S_{n-1,n+1,x} - S_{n+1,n-1,x} - S_{n+1,n+1,x}\Big) - \\
- \quad & \frac{RV_x f_x(t)\sin(\omega_L t)}{4}\sum_{n=-\infty}^{\infty}\Big(\dot{S}_{n-2,n,x} + 2\dot{S}_{n,n,x} + \dot{S}_{n+2,n,x} - \\
- \quad & \dot{S}_{n-1,n-1,x} - \dot{S}_{n-1,n+1,x} \dot{-} S_{n+1,n-1,} - \dot{S}_{n+1,n+1,}\Big) \qquad (2.108)
\end{aligned}
$$

with:

$$
\begin{aligned}
\dot{S}_{mnx} &= -i\omega_{nm}c_m^* c_n + \frac{i}{\hbar}V_x f_x(t)\sin(\omega_L t)\sum_{k=-\infty}^{\infty}\Big[u_{mk}^* c_k^* c_n - u_{nk}c_m^* c_k\Big] \qquad (2.109)\\
&= -i\omega_{nm}c_m^* c_n + \frac{i}{2\hbar}V_x f_x(t)\sin(\omega_L t)\sum_{k=-\infty}^{\infty}\cdot \\
&\cdot \quad \Big[\left(\delta_{m-k+1,0} + \delta_{m-k-1,0}\right)c_k^* c_n - \\
&- \quad c_m^*\left(\delta_{n-k+1,0} + \delta_{n-k-1,0}\right)c_k\Big] \qquad (2.110)\\
&= -i\omega_{nm}c_m^* c_n + \frac{i}{2\hbar}V_x f_x(t)\sin(\omega_L t)\cdot \\
&\cdot \quad \Big[\left(c_{m-1,x}^* + c_{m+1,x}^*\right)c_n - c_m^*\left(c_{n-1,x} + c_{n+1,x}\right)\Big] \qquad (2.111)\\
&= -i\omega_{nm}S_{m,n,x} + \frac{i}{2\hbar}V_x f_x(t)\sin(\omega_L t)\cdot \\
&\cdot \quad \Big(S_{m-1,n,x} + S_{m+1,n,x} - S_{m,n-1,x} - S_{m,n+1,x}\Big). \qquad (2.112)
\end{aligned}
$$

Then the x acceleration will be the summation of eq. 2.105 and eq. 2.108.

For the y acceleration we must calculate:

$$
\begin{aligned}
&\frac{d}{dt}\Big[\frac{\hbar R}{2}\sum_{n=-\infty}^{\infty}\left(\omega_{n,n-1}S_{n-1,n,y} - \omega_{n,n+1}S_{n+1,n,y}\right)\Big] = \qquad (2.113)\\
&\qquad \frac{\hbar R}{2}\sum_{n=-\infty}^{\infty}\Big(\omega_{n,n-1}\dot{S}_{n-1,n,y} - \omega_{n,n+1}\dot{S}_{n+1,n,y}\Big) \qquad (2.114)
\end{aligned}
$$

$$
\begin{aligned}
\frac{d}{dt} \quad & \Big[\frac{RV_y f_y(t)\sin(\omega_L t)}{4}\sum_{n=-\infty}^{\infty}\Big(S_{n-2,n,y} - 2S_{n,n,y} + S_{n+2,n,y} + S_{n-1,n+1,y} - \\
- \quad & S_{n-1,n-1,y} + S_{n+1,n-1,y} - S_{n+1,n+1,y}\Big)\Big] = \qquad (2.115)
\end{aligned}
$$

$$
\begin{aligned}
&= \frac{RV_y f_y(t)\omega_L \cos(\omega_L t)}{4} \sum_{n=-\infty}^{\infty} \Big(S_{n-2,n,y} - 2S_{n,n,y} + S_{n+2,n,y} + S_{n-1,n+1,y} - \\
&- S_{n-1,n-1,y} + S_{n+1,n-1,y} - S_{n+1,n+1,y} \Big) + \\
&+ \frac{RV_y \dot{f}_y(t) \sin(\omega_L t)}{4} \sum_{n=-\infty}^{\infty} \Big(S_{n-2,n,y} - 2S_{n,n,y} + S_{n+2,n,y} + S_{n-1,n+1,y} - \\
&- S_{n-1,n-1,y} + S_{n+1,n-1,y} - S_{n+1,n+1,y} \Big) + \\
&+ \frac{RV_y f_y(t) \sin(\omega_L t)}{4} \sum_{n=-\infty}^{\infty} \Big(\dot{S}_{n-2,n,y} - 2\dot{S}_{n,n,y} + \dot{S}_{n+2,n,y} + \dot{S}_{n-1,n+1,y} - \\
&- \dot{S}_{n-1,n-1,y} + \dot{S}_{n+1,n-1,y} - \dot{S}_{n+1,n+1,y} \Big) \qquad (2.116)
\end{aligned}
$$

with:

$$
\begin{aligned}
\dot{S}_{mn,y} &= -i\omega_{nm} c_m^* c_n + \frac{i}{\hbar} V_y f_y(t) \sin(\omega_L t) \sum_{k=-\infty}^{\infty} \Big[v_{mk}^* c_k^* c_n - v_{nk} c_m^* c_k \Big] \qquad (2.117) \\
&= -i\omega_{nm} c_m^* c_n + \frac{1}{2\hbar} V_y f_y(t) \sin(\omega_L t) \cdot \sum_{k=-\infty}^{\infty} \Big[\left(\delta_{m-k+1,0} - \delta_{m-k-1,0}\right) c_k^* c_n + \\
&+ c_m^* \left(\delta_{n-k+1,0} - \delta_{n-k-1,0}\right) c_k \Big] \qquad (2.118) \\
&= -i\omega_{nm} c_m^* c_n + \frac{1}{2\hbar} V_y f_y(t) \sin(\omega_L t) \cdot \\
&\cdot \Big[\left(c_{m+1,y}^* - c_{m-1,y}^* \right) c_n + c_m^* \left(c_{n+1,y} - c_{n-1,y} \right) \Big] \qquad (2.119) \\
&= -i\omega_{nm} S_{m,n,y} + \frac{1}{2\hbar} V_y f_y(t) \sin(\omega_L t) \cdot \\
&\cdot \Big(S_{m+1,n,y} - S_{m-1,n,y} + S_{m,n+1,y} - S_{m,n-1,y} \Big). \qquad (2.120)
\end{aligned}
$$

Then the x acceleration will be the summation of eq. 2.113 and eq. 2.116. In fig. 2.3 we can see the spectra calculated using the two methods: dipole spectrum and acceleration spectrum. Both the spectra are very similar, in fact they present the same information. We have some differences in the first part of the spectra, there the dipole spectrum presents a descendent shape while the acceleration spectrum have a little peak near the 5-th harmionic. We can obtain the same shape of the acceleration spectra by multiply the dipole spectra for ω^4. We also notice that the acceleration spectrum presents a wider plateau than the dipole spectrum. In this thesis we do not show the spectra calculated with the electron trajectory because at present we are working on it and we do not have complete simulations.

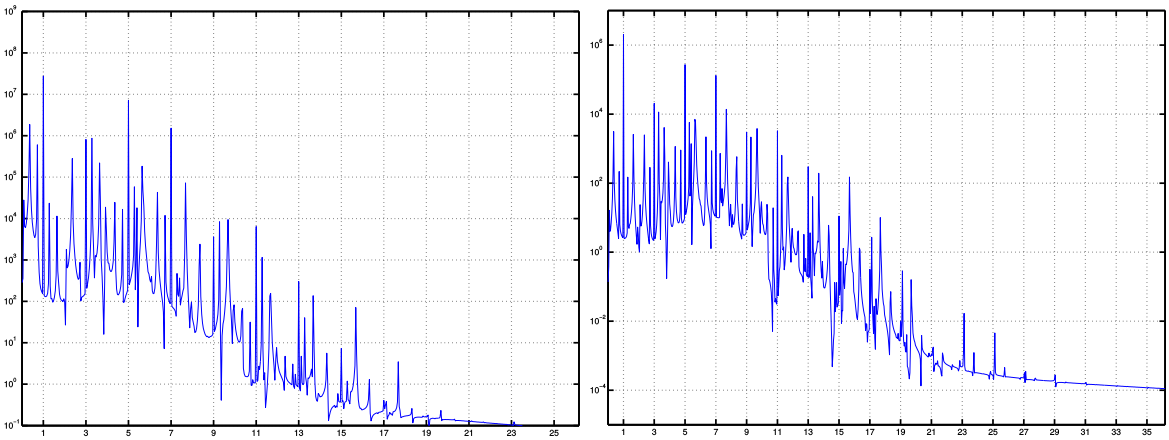

Figure 2.3: Harmonic spectra calculated on one nanoring of radius R=2.7 au and a driven by a laser field with $\lambda = 800$ nm and intensity $I = 6 \cdot 10^{14}$ W/cm^2. On the left we present the dipole spectrum and on the right we present the acceleration spectrum. In the x-axes we have the harmonic order and in the y-axes we have the intensity in arbitrary units.

Part 2

Results

3 Fullerenides: High Harmonic Generation

In this chapter we study the behaviour of one fullerene in presence of a strong Laser field and compare our theoretical model with experimental studies of high-order harmonic generation in the plasmas containing fullerenes under different plasma conditions and laser parameters in the case of sub-5 fs (femtosecond = 10^{-15} s) pulses.

3.1 Theoretical Model

We consider one electron constrained over a spherical surface with 60 atoms in the presence of a laser electric field linearly polarized along the z-axis. We have chosen to use this values to compare it with the fullerens C_{60}. Fullerenes have a graphite-like structure, but instead of purely hexagonal packing, they also contain pentagons (or even heptagons) of carbon atoms, which bend the graphene sheet into spheres, ellipses, or cylinders. Among fullerenes, C_{60} is particularly noteworthy since its pentagonal and hexagonal rings of carbon atoms give it a spherical shape. This feature endows C_{60} with an appealing spherical symmetry which can be used to simplify the treatment [1].

In the dipole approximation, the laser field has the form

$$\vec{\mathcal{E}}(t) = \hat{k}\vec{\mathcal{E}}_L f(t)\sin(\omega_L t) \tag{3.1}$$

with $\mathcal{E}_L$ the intensity of the field, $f(t)$ the pulse profile and $\hat{k}$ the z-unit vector. In our calculation we have used two pulse profiles: the first one has trapezoidal shape

and the second one a gaussian shape. The TDSE to be solved is

$$i\hbar\frac{\partial}{\partial t}\psi(t) = \mathcal{H}\psi(t) \tag{3.2}$$

with $\mathcal{H}$ the hamiltonian of the system:

$$\mathcal{H} = \mathcal{H}_0 + \hbar\Omega_L(t)\cos(\theta)\sin(\omega_L t) \tag{3.3}$$

where

$$\mathcal{H}_0 = \frac{\hbar^2}{2I}\hat{\ell}^2 \tag{3.4}$$

is the hamiltonian of the electron in the absence of the laser, $\hat{\ell}^2$ is the angular momentum operator, and

$$\Omega_L(t) = \frac{e\mathcal{E}(t)R}{\hbar}, \tag{3.5}$$

where $\mathcal{E}$ is the electric field.

The energies of the states of the unperturbed hamiltonian $\mathcal{H}_0$ are

$$\hbar\omega_\ell \equiv \frac{\hbar^2}{2I}\ell(\ell+1), \tag{3.6}$$

and the energy gap between adjacent levels grows linearly with the level order,

$$\hbar\omega_{\ell+1,\ell} \equiv \hbar(\omega_{\ell+1} - \omega_\ell) = \frac{\hbar^2}{I}(\ell+1) \tag{3.7}$$

then the gap between contiguous energy levels is linearly increasing with ℓ, this is the result of the supposed spherical symmetry and mimics the characteristic ionization suppression of the fullerene. Infact the fullerene C_{60} has an ionization energy of about 7.6 eV but it can absorb photons from the laser field up to 50 eV before undergoing ionization [7]. It is convenient to write the state vector $\mid t\rangle$ as a linear combination of eigenstates of the laser free Hamiltonian $\frac{\hbar^2}{2I}\mathbb{L}^2$. If we solve the TDSE we find the expansion coefficients $c_{\ell m}$ of the wavefunction $\mid t\rangle$, and the linear combination of the state vector $\mid t\rangle$ will be :

$$\mid t\rangle = \sum_{\ell'=0}^{\infty}\sum_{m'=-\ell}^{\ell} c_{\ell',m'}(t) \mid \ell', m'\rangle. \tag{3.8}$$

Because φ is a cyclic variable, the laser will couple solely states with $m = m'$; let $\mid \Lambda, m\rangle$ be the initial state of the electron, with Λ the quantum number of the initial orbital angular momentum, then the Schrödinger equation becomes

$$i\dot{c}_{\ell m} = \omega_\ell c_{\ell m} + \Omega_L \sum_{\ell'=\Lambda}^{\infty} \sin(\omega_L t)\langle \ell, m \mid \cos(\theta) \mid \ell', m\rangle c_{\ell', m} \tag{3.9}$$

The matrix elements are:

$$\langle \ell, m \mid \cos(\theta) \mid \ell', m\rangle = \sqrt{\frac{4\pi}{3}} \int Y_{\ell,m}(\theta,\varphi)^* Y_{1,0}(\theta,\varphi) Y_{\ell',m}(\theta,\varphi) \mathrm{d}\Omega. \tag{3.10}$$

If we set

$$b_{\ell m} \equiv \sqrt{\frac{(\ell + m + 1)(\ell - m + 1)}{(2\ell + 1)(2\ell + 3)}} \tag{3.11}$$

we obtain

$$\begin{aligned} \int Y_{\ell,0}(\theta,\varphi)^* Y_{1,0}(\theta,\varphi) Y_{\ell+1,m}(\theta,\varphi)\mathrm{d}\Omega &= \sqrt{\frac{4\pi}{3}} b_{\ell,m} \qquad \text{if } \ell \geq \Lambda \\ \int Y_{\ell,0}(\theta,\varphi)^* Y_{1,0}(\theta,\varphi) Y_{\ell-1,m}(\theta,\varphi)\mathrm{d}\Omega &= \sqrt{\frac{4\pi}{3}} b_{\ell-1,m} \quad \text{if } \ell > \Lambda \end{aligned}$$

Therefore

$$i\dot{c}_{\Lambda,m} = \omega_\Lambda c_{\Lambda,m} + \Omega_0(t) b_{\Lambda,m} \sin(\omega_L t) c_{\Lambda+1,m} \tag{3.12}$$

$$i\dot{c}_{\ell>\Lambda,m} = \omega_\ell c_{\ell,m} + \Omega_0(t) \sin(\omega_L t)(b_{\ell-1,m} c_{\ell-1,m} + b_{\ell,m} c_{\ell+1,m}) \tag{3.13}$$

Thus, the TDSE can be written as the following set of coupled differential equations

$$\begin{cases} i\dot{c}_{\Lambda,m} = \omega_\Lambda c_{\Lambda,m} + \Omega_0(t) b_{\Lambda,m} \sin(\omega_L t) c_{\Lambda+1,m} \\ i\dot{c}_{\Lambda+1,m} = \omega_{\Lambda+1} c_{\Lambda+1,m} + \Omega_0(t)(b_{\Lambda,m} c_{\Lambda,m} + b_{\Lambda+1,m} c_{\Lambda+2,m}) \sin(\omega_L t) \\ i\dot{c}_{\Lambda+2,m} = \omega_{\Lambda+2} c_{\Lambda+2,m} + \Omega_0(t)(b_{\Lambda+1,m} c_{\Lambda+1,m} + b_{\Lambda+2,m} c_{\Lambda+3,m}) \sin(\omega_L t) \\ \vdots \\ i\dot{c}_{\Lambda+s,m} = \omega_{\Lambda+s} c_{\Lambda+s,m} + \Omega_0(t)(b_{\Lambda+s-1,m} c_{\Lambda+s-1,m} + b_{\Lambda+s,m} c_{\Lambda+s+1,m}) \sin(\omega_L t) \\ \vdots \\ i\dot{c}_{\Lambda+M,m} = \omega_{\Lambda+M} c_{\Lambda+M,m} + \Omega_0(t) b_{\Lambda+M-1,m} c_{\Lambda+M-1,m} \sin(\omega_L t) \\ i\dot{c}_{\Lambda+M+1,m} = 0 \end{cases}$$

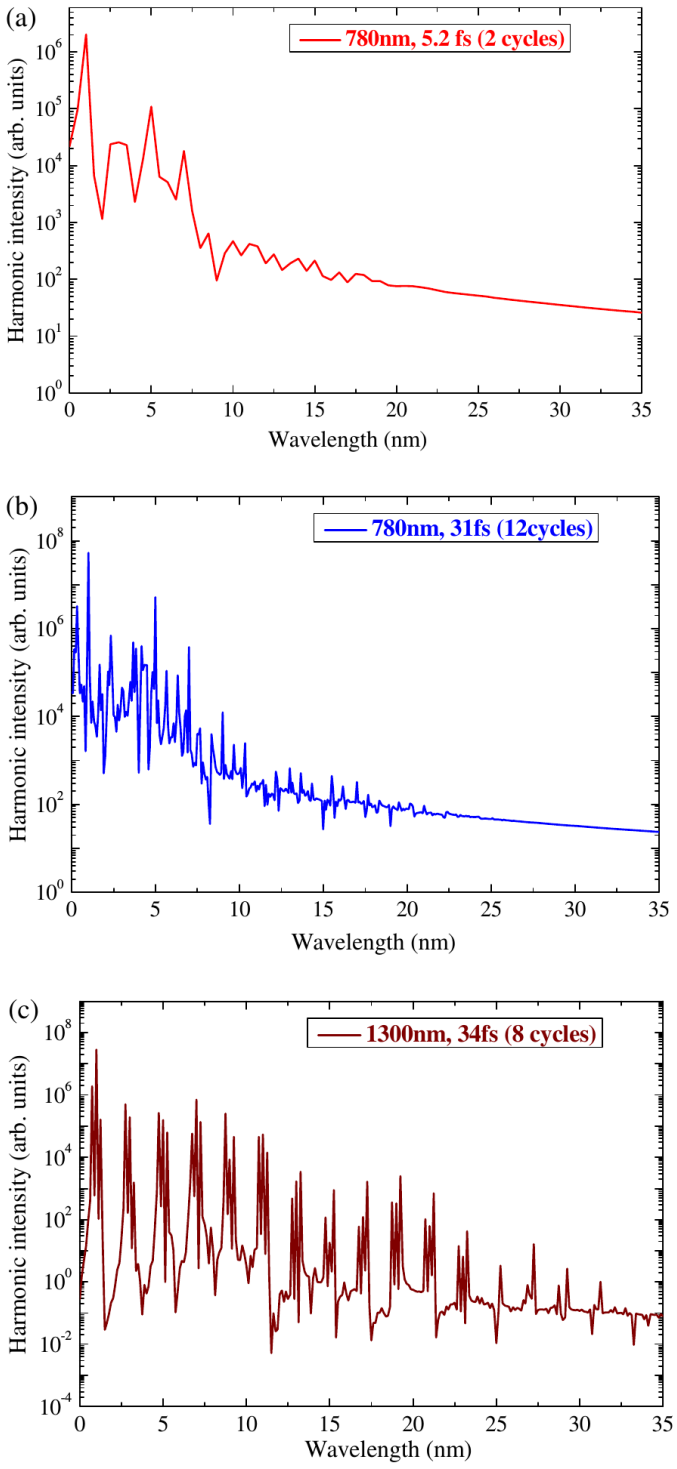

Figure 3.1: (Color online) Calculated data of the harmonic spectra from fullerene plasma in the case of (a), (b) 780 nm and (c) 1300 nm probe radiation. The pulse durations are (a) 2 optical cycles (5.2 fs), (b) 12 optical cycles (31 fs), and (c) 8 optical cycles (34 fs).

since the energy gap increases linearly with ℓ, the higher levels will not be significantly populated and then it is possible to truncate the system of differential equations for N a sufficiently large integer. Then the energy levels with quantum number $\ell > \Lambda + M$, where M is quantum number that refers to the z-projection of the angular momentum, do not participate to the dynamics of the system. The set of differential equations shows a ladder like structure so that any energy level is coupled to the two nearest levels. This system of differential equations has been truncated at the level M and it has been numerically solved by use of the matlab numerical routine ode45. The ode45 rutine is based on an explicit Runge-Kutta formula, the Dormand-Prince pair. It is a one-step solver, in computing $y(t_n)$, it needs only the solution at the immediately preceding time point, $y(t_{n-1})$.

The wave function yields the electric dipole moment as:

$$\langle t \mid R\cos(\theta) \mid t \rangle = R\sum_{s,0}^{\infty}(c^*_{\Lambda+s,m}c_{\Lambda+s+1,m} + c_{\Lambda+s,m}c^*_{\Lambda+s+1,m})b_{\Lambda+s,m} \tag{3.14}$$

whose Fourier transform yields the spectrum.

The calculated harmonic spectrum from C_{60} is presented in Fig. 3.1 on the facing page in the case of 775 nm ($\hbar\Omega_L$= 1.6 eV) femtosecond pulses propagating through the fullerene medium. The theoretical model presented here exploits the spherical symmetry of the C_{60} by introducing radical approximations, the most important of which is the fact that the molecule cannot be ionized. This approximation deserves some comments. In spite of the ionization suppression of the C_{60} molecule, some ionization is bound to occur so that the theory becomes unreliable when ionization becomes relevant; this situation is reached when the laser pulse is intense or long lasting. The theory can be extended to cope with these situations by introducing an imaginary part in the energy of the levels.

3.2 Experimental Results

We give a detailed description of experimental setup made by the research group at the Imperial College of London led by Rashid Ganeev and Jon Marangos.

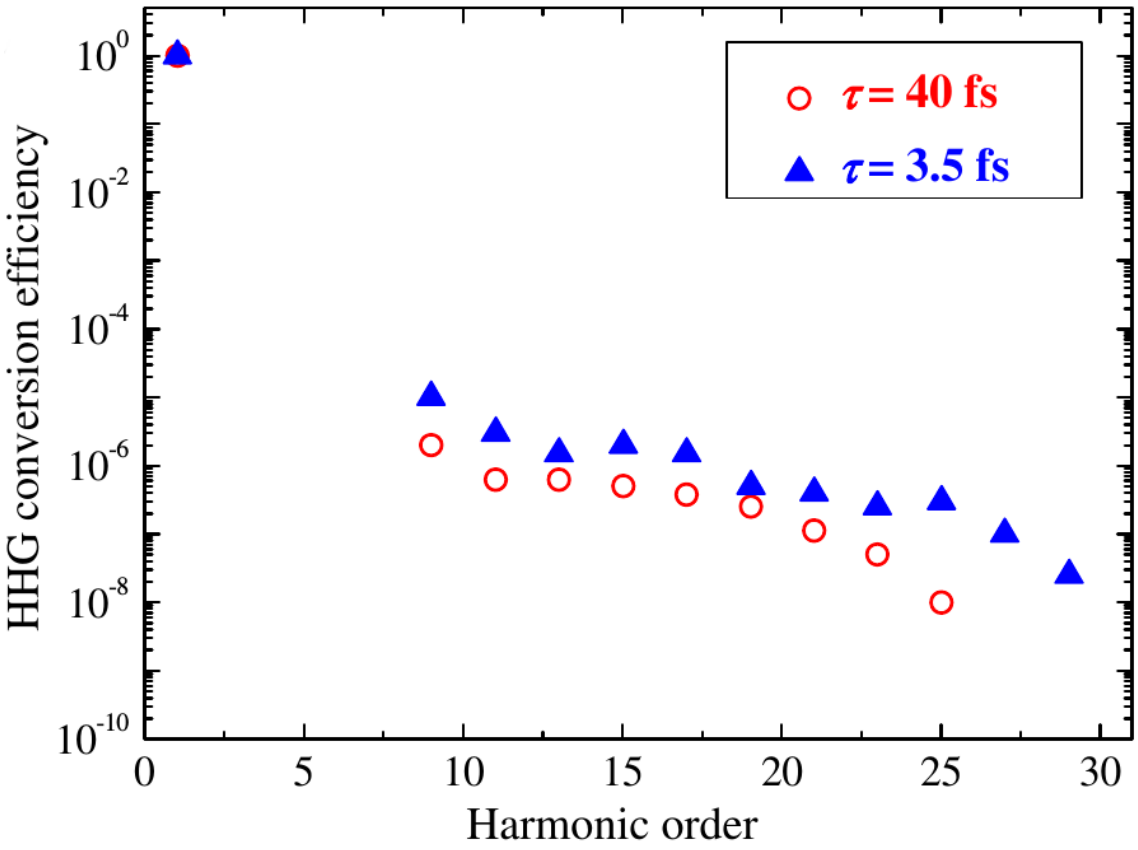

Figure 3.2: Comparative studies of the HHG from fullerene plasma using the 4.5 fs (triangles) and 40 fs (circles) pulses.

In the experiment was used a short laser pulse to create the fullerene ablation plume. The laser is a Ti:sapphire with a wavelength 775 nm and intensity $I_{fs} = 5 \cdot 10^{14}\mathrm{W/cm^2}$ It was focused into the plasma plume to generate high-order harmonics. The HHG radiation was analysed by a spatially-resolving XUV spectrometer. In these experiments it has been studied in particular the C_{60} powder for harmonics generation.

The results of comparative studies of the HHG in fullerene plasma using the few-cycle (4.5 fs) and multi-cycle (40 fs) pulses are presented in Fig. 3.2. One can see that the cutoff in the case of longer pulses (25th harmonic) was shorter with regard to the few-cycle pulses.

3.3 Comparision of Results

We presented the results of the experimental and theoretical studies of high-order harmonic generation in the plasmas containing fullerenes under different conditions and laser duration of the pulse of 4.5 fs anf 45 fs.

In Fig. 3.1 we show the calculated harmonic spectra from C_{60} in the case of 780 nm(photon energy E_{ph} =1.6 eV) and 1300 nm (photon energy E_{ph} =0.96 eV) pulses propagating through the fullerene medium. The calculations were carried out for 2-cycle pulses (t = 5.2 fs) and 12-cycle pulses (t = 1 fs) of 780 nm radiation and 8-cycle pulses (t = 34 fs) of 1300 nm radiation and intensity $6 \cdot 10^{14}$ W/cm^2 , which were close to the conditions of fullerene HHG experiments. The spectra are formed of well-resolved harmonics but with broadened lines (in the case of short pulses) and hyper Raman lines (in the case of long pulses). Hyper Raman, lines with frequency other than harmonics, are due to transitions between laser dressed molecular states.

Our calculations showed well-defined harmonics (up to H_c =31) in the case of 1300 nm multicycle pulses. The theoretical model exploited the spherical symmetry of the C_{60} by introducing a number of approximations, the most important of which is that the molecule cannot be ionized. This approximation deserves some comment. In spite of the ionization suppression of the C_{60} molecule, some ionization is bound to occur so that the theory becomes unreliable when ionization becomes significant. The harmonic cutoff in the case of 1300 nm radiation was extended compared with 780 nm radiation (H_c =17), analogously as in the case of experiment.

The comparative studies using 3.5 and 40 fs pulses showed that, for few-cycle pulses, the harmonic cutoff is extended compared with multicycle pulses, which can be attributed to reduced fragmentation of C_{60} for the shorter pulse. The comparison of fullerene harmonic spectra generated in the case of 1300 and 780 nm multicycle probe pulses showed the extension of generating harmonic orders in the former case. Theoretical calculations of fullerene harmonic spectra were carried out in the single active electron approximation, which showed harmonics up to H_c =31 in the case of 1300 nm multicycle pulses and up to H_c =17 in the case of 780 nm multicycle pulses.

4 High-order-harmonic generation in dimensionally reduced systems

4.1 Introduzione

In this chapter we discuss the response of a nanoring driven by a laser field in different states of polarization with particular attention to the spectrum emitted by the laser-induced charge oscillations. We use the dependent wave function of a nanoring driven by a laser field for studying the properties of the electromagnetic radiation emitted by the nanoring as a function of the polarization state of the laser. The diffused radiation has the characteristics of high order harmonic generation. For non circularly polarized laser field it is evident an extension of the expected cutoff position indicating that nanorings are efficient sources of radiation. The polarization state of the emitted harmonics can be opportunely controlled by varying the parameters of the pump field. The profile of the absorbed angular moment shows that a magnetic moment can be induced depending on the polarization of the driven field.

4.2 Theory

Let us consider an electron constrained over a circle of radius R lying in the $x-y$ plane and acted upon by a laser elliptically polarized in the same plane.

The number of free parameters entering the problem is large and might entwine the relation between causes and effects into a Gordian knot; thus, in the following,

we undertake all the simplifying steps which can help the comprehension. With this guiding idea we confine our treatment to relatively long pulse duration in order to reduce effects related to envelope phase and line broadening. The external electric field is therefore taken of the form

$$\vec{\mathcal{E}}(\vec{r},t) = \mathcal{E}_L f(t)\Big[\vec{\epsilon}_x \cos\beta \cos(\omega_L t) + \vec{\epsilon}_y \sin\beta \sin(\omega_L t)\Big] \tag{4.1}$$

$\vec{\epsilon}_x$ and $\vec{\epsilon}_y$ being the unit vectors along the x and y axes respectively and $\beta \in [0, \pi/2]$ a parameter characterizing the field polarization: $\beta = 0$ gives a laser polarized along the x axis, $\beta = \pi/2$ gives a laser polarized along the y axis, $\beta = \pi/4$ gives a circular polarization. It is worth to note that the phase of the field, for linear polarization along the two axes, differs by $\pi/2$, therefore slightly different results are to be expected in the two cases. The pulse shape of the field is described by the function $f(t)$.

We solve the time dependent Schroedinger equation

$$i\hbar\frac{\partial}{\partial t}|t\rangle = \mathcal{H}|t\rangle \tag{4.2}$$

with

$$\mathcal{H} = \mathcal{H}_0 + \hbar\Omega(t)\Big[\cos\beta\cos(\omega_L t)\cos\varphi + \sin\beta\sin(\omega_L t)\sin\varphi\Big] \tag{4.3}$$

the full time dependent Hamiltonian of the problem. Here

$$\mathcal{H}_0 = \frac{\hbar^2}{2m_e R^2}\hat{\ell}_z^2 \tag{4.4}$$

is the laser free Hamiltonian, with only the kinetic energy term, and

$$\hbar\Omega(t) \equiv e\mathcal{E}_L R f(t) \tag{4.5}$$

describes the laser-ring maximum interaction energy; $\hat{\ell}_z$ is the usual z component of the orbital angular momentum operator (in units of $\hbar$) whose eigenvectors and eigenvalues are the well known angular momentum states

$$\hat{\ell}_z|m\rangle = m|m\rangle, \quad m = 0, \pm1, \pm2\ldots; \tag{4.6}$$

the analytical expression for $|m\rangle$ being

$$|m\rangle \to \Phi_m(\varphi) = \frac{e^{im\varphi}}{\sqrt{2\pi}}. \tag{4.7}$$

The states $|m\rangle$ are eigenstates of $\mathcal{H}_0$ with energy

$$\mathcal{H}_0|m\rangle = \hbar\omega_m|m\rangle \Rightarrow \hbar\omega_m = \frac{\hbar^2 m^2}{2m_e R^2} \tag{4.8}$$

and provide a suitable basis for the Hilbert space of our problem. The ground state $|0\rangle$ is not degenerate while the states $|\pm m\rangle$ have the same energy.

We expand the time dependent state $|t\rangle$ as a linear combination of the bare states

$$|t\rangle = \sum_{m=-\infty}^{+\infty} a_m(t)|m\rangle; \tag{4.9}$$

by making use of the matrix elements

$$\langle n|\cos\varphi|m\rangle = \frac{1}{2}(\delta_{m-n+1,0} + \delta_{m-n-1,0}) \tag{4.10}$$

$$\langle n|\sin\varphi|m\rangle = \frac{-i}{2}(\delta_{m-n+1,0} - \delta_{m-n-1,0}) \tag{4.11}$$

we obtain a set of coupled equations for the probability amplitudes:

$$i\dot{a}_n = \omega_n a_n + \frac{\Omega(t)}{2}\Big\{[\cos\beta\cos(\omega_L t) - i\sin\beta\sin(\omega_L t)]a_{n-1} + \\ + [\cos\beta\cos(\omega_L t) + i\sin\beta\sin(\omega_L t)]a_{n+1}\Big\} \tag{4.12}$$

showing a ladder type coupling of the states; this set of equations has been solved by numerical integration. The gap between the energy levels increases linearly with $|n|$ and we expect that upper states are negligibly populated and do not contribute to the evolution of the systems. Therefore we solve this set of coupled equations by mere truncating the system for $|m| \geq 10$; we checked that states with $|m| > 10$ do not contribute to the final result for the values of the physical parameters we use .

From the state $|t\rangle$ we can calculate all time dependent quantum averaged (TDQA) parameters that are relevant to our ends. The TDQA dipole moment is $\vec{D}(t) = -e\vec{r}(t)$ with

$$\vec{r} = \vec{\epsilon}_x\langle t|x|t\rangle + \vec{\epsilon}_y\langle t|y|t\rangle = \sum_{n=-\infty}^{+\infty}\Big[\vec{\epsilon}_x\Re(a_{n-1}^* a_n) + \vec{\epsilon}_y\Im(a_n^* a_{n-1})\Big] \tag{4.13}$$

the TDQA position of the electron, the TDQA energy being given by

$$E(t) = \sum_{m=-\infty}^{+\infty} |a_m(t)|^2 \hbar\omega_m \tag{4.14}$$

and the TDQA angular momentum acquired by the electron being

$$L_z(t) = \sum_{m=-\infty}^{+\infty} |a_m(t)|^2 m\hbar. \tag{4.15}$$

To these quantities we associate the correspondent time independent quantum averaged quantities:

$$\langle E \rangle = \frac{1}{T} \int_0^T E(t)dt \tag{4.16}$$

and

$$\langle L_z \rangle = \frac{1}{T} \int_0^T L_z(t)dt \tag{4.17}$$

with T the laser pulse duration.

In the last two decades, HHG has been dedicated much attention because opens the route towards devices generating high frequency and coherent electromagnetic radiation. In atoms driven by a linearly polarized field, it already seems a well established fact that the maximum obtainable frequency ω_M (cutoff) is given by the general law of the eq. 2.15 on page 17.

The relation (2.15) can be easily determined from mere energy conservation law and classical physics; it corresponds to a classical trajectory of the electron that reaches the continuum and then is recaptured by the parent ion [8, 9]; such a trajectory exists only for linearly polarized laser field. By quantal or classical calculations the favorable trajectory that gives rise to the emission of $\hbar\omega_M$ can be determined [10]. At this point it should be stressed that the cutoff photon is emitted during the head on collision and recapture process but any electromagnetic emission is essentially due to the acceleration of the electron. HHG has been obtained for physical situations when no recollision is presented such as two level systems [11, 12, 13] or even when no bound state is supported such as repulsive potentials [14]. Other cutoff laws have been obtained for two level atoms or molecules [15, 11, 16, 17].

If a source of high frequency radiation is looked after, it is of paramount importance to be able to increase the value of ω_M by changing the free physical parameters. However the rigid law in Eq. (2.15) seems to leave to the researcher the laser parameters and, essentially, $\mathcal{E}_L/\omega_L$ as efficient control knob.

Sources other than atoms are under investigation. Among the more promising there is to consider molecules providing all their free parameters as control knobs. Accordingly to theory, the emission power is proportional to $|\vec{r}(\omega)|^2$ ($\vec{r}(\omega)$ is the Fourier transform of $\vec{r}(t)$); molecules have larger sizes, are more polarizable than atoms and, thus, can give a good harmonic yield at relative lower laser intensity. Nanomolecules have large dimensions, display simplifying symmetries that paradoxically can make calculations easier than for smaller molecules and, when nanodots are at hand, can be taylored at will.

One of the points of interest of this chapter is the study of the dependence of the polarization state of the emitted harmonics upon the polarization state of the pump laser. Elliptically polarizable laser fields, that do not favor HHG from atoms, can stimulate emission from molecules; this is an appealing feature for molecules since it allows the control of the polarization of the harmonics [18]. Moreover nanorings can be magnetized and the question is still a scarcely explored ocean.

All of this suggests us the study of a nanoring driven by a laser field in different polarization states. Again, to keep the extension of this work within reasonable boundaries, we shall concentrate solely on the main effects without following all the rivulets furrowing the area whose exploration is procrastinated to subsequent works.

4.3 Results

Here we present calculations of a nanoring with radius $R = 2.7a_0$ driven by a laser field given in Eq.(4.1); $f(t)$ is a trapezoidal function with ramps lasting 4 optical cycles (oc) and total duration of 32 oc. Since we are interested in the response of the system to different laser polarization, we decide to keep the overall laser intensity $I_L \propto \mathcal{E}_L^2 = \mathcal{E}_x^2 + \mathcal{E}_y^2$ constant. Here, according to Eq. (4.1), $\mathcal{E}_x = \mathcal{E}_L \cos\beta$ and

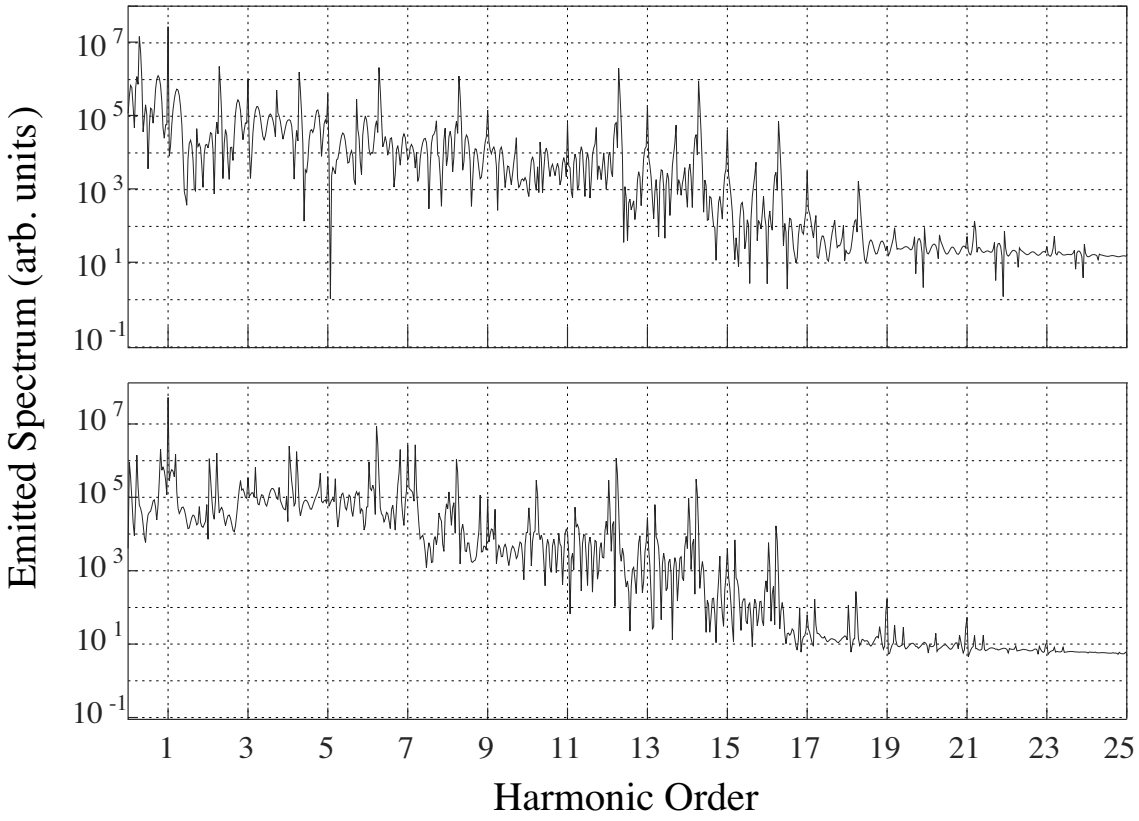

Figure 4.1: Spectrum emitted by the nanoring. The relevant parameters entering the calculations are $I_L = 4 \cdot 10^{14}$ W/cmâĹŠ^2, $\lambda_L = 1969$ nm ($\hbar\omega_L = 0.63$ eV). (Top) $\beta = 0°$ (laser polarized along the x axis); (bottom) $\beta = 20°$ (elliptically polarized laser, $I_x = 3.5 \cdot 10^{14}$ W/cm^2; $I_y = 4.7 \cdot 10^{13}$ W/cm^2)

$\mathcal{E}_y = \mathcal{E}_L \sin\beta$ denote the maximum values of the driving field along the x and y directions respectively. As a rule we denote the laser with I_L given in W cm^{-2}.

The polarization of the nth harmonic field is determined by the angle ψ and the eccentricity e_c defined as [19, 18]:

$$\tan 2\psi = \tan(2\alpha)\cos\delta\,, \quad 0 \leq \psi < \pi \tag{4.18}$$

$$e_c = \tan\chi\,, \quad -\pi/4 < \chi \leq \pi/4 \tag{4.19}$$

with $\sin 2\chi = \sin 2\alpha \sin\delta$, $\tan\alpha = (\mathcal{E}_x^{(n)}/\mathcal{E}_y^{(n)})$ and δ the relative phase between $\mathcal{E}_x^{(n)}$ and $\mathcal{E}_y^{(n)}$; the negative (positive) sign for e_c takes into account for the clockwise (counterclockwise) orientation of the emitted harmonic.

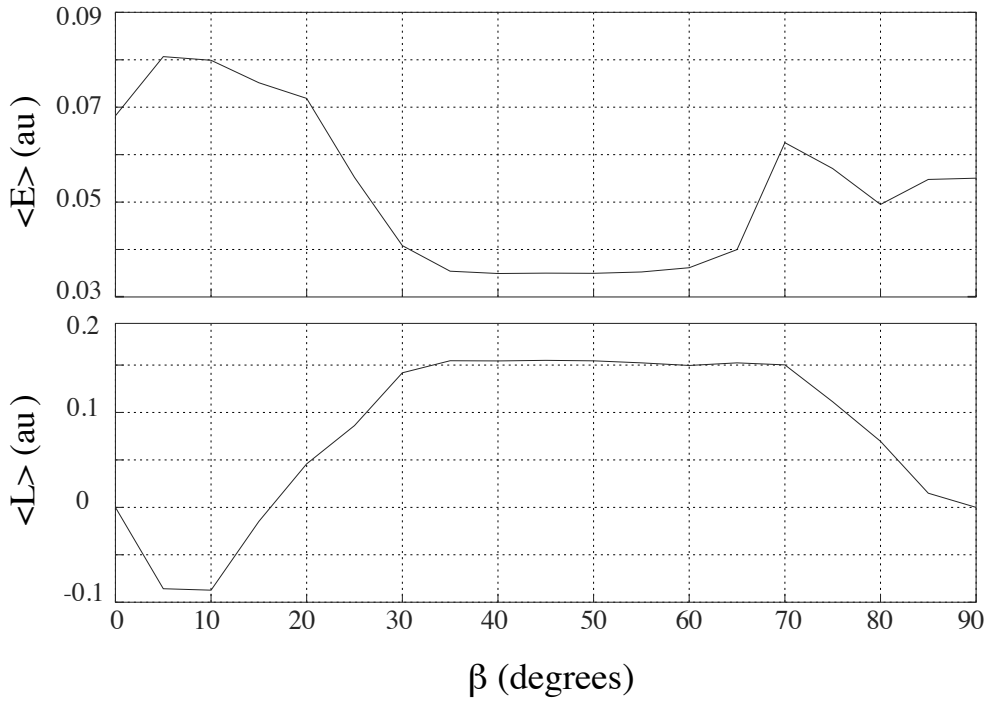

Figure 4.2: (Top) Average energy (in au); (bottom) average angular momentum (in units of $\hbar$) absorbed by the ring in the whole laser shot versus the polarization parameter β in degrees. The relevant parameters used for the calculations are $I_L = 4 \cdot 10^{14}$ W/cmâĹŠ^2 , $\lambda_L = 1969$ nm ($\hbar\omega_L = 0.63$ eV)

We discuss the response of the system to a laser operating in the infrared and visible laser regime and start our discussion with the case when $\hbar\omega_L = 0.63$ eV so that $\omega_1 - \omega_0 = 3\omega_L$. The laser intensity is taken as $I_L = 4 \cdot 10^{14}$ W cm^{-2}. With such a choice of the parameters, Eq. (2.15) gives an expected cutoff of the emission in atoms at $\omega_M = 12\omega_L$.

In Fig (4.1 on the preceding page) we show the spectrum emitted by the nanoring for two different polarizations. A circularly polarized pump does not produce harmonics and this is to be waited for, since the model is too symmetric to give a significant yield in the actual situation. Movies of the behavior of the electronic packet show the presence of a rotating packet with constant velocity, then the absence of significant electron acceleration prevents the emission of photons . Linear and elliptic polarization show emission lines (harmonic and not) and an extended cutoff.

Always for the same laser intensity I_L in Fig. (4.2) we show the absorbed energy $\langle E \rangle$ [from Eq: (4.16 on page 48)] and the acquired angular momentum $\langle L_z \rangle$ [from Eq:

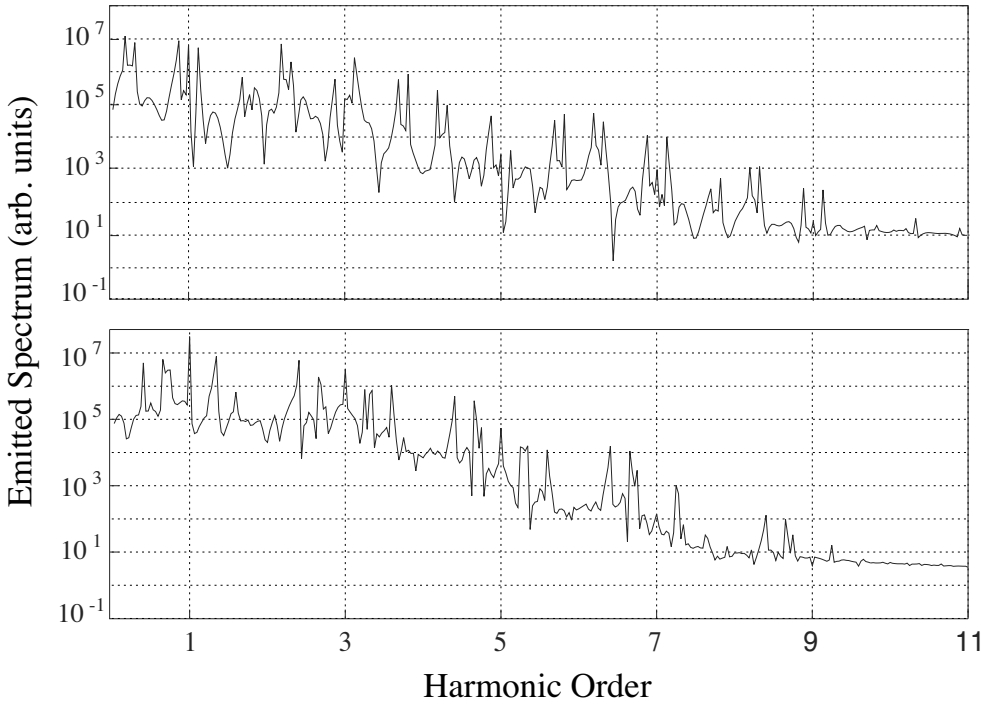

Figure 4.3: Spectrum emitted by the nanoring. The relevant parameters entering the calculations are $I_L = 4 \cdot 10^{14}$ W/cmâĹŠ^2, $\lambda_L = 591$ nm ($\hbar\omega_L = 2.1$ eV). (Top) $\beta = 0°$ (laser polarized along the x axis); (bottom) $\beta = 20°$ (elliptically polarized laser, $I_x = 3.5 \cdot 10^{14}$ W/cm^2; $I_y = 4.7 \cdot 10^{13}$ W/cm^2)

(4.17 on page 48)]: there is a net absorption of energy and angular momentum during the laser shot at all values of β. Letting aside the obvious result for linear polarization, we see that for a wide range of angles the transferred momentum is distributed along a plateau. This means that a magnetic momentum can be induced in a nanoring by a loosely polarized laser field. We have performed similar calculations for $\hbar\omega_L = 2.1$ eV and the same value of the laser intensity giving a nominal cutoff energy $\omega_M = 3\omega_L$. In Fig.s (4.3) the spectra are shown. Again the cutoff is more extended than expected and shows that nanorings are efficient emitters. This appealing results can be motivated by considering the differences between atoms and nanorings. In atoms, by using the three steps model, the cutoff is the maximum energy obtainable by the active electron and compatible with a recapture act. Conceptually in nanorings there is no upper limit to the energy that can be gained by the electron and delivered in a single photon emission. It is surprising that a simple system with states coupled in a ladder way can still emit all the energy in a single shot. Of course the position of the plateau is an

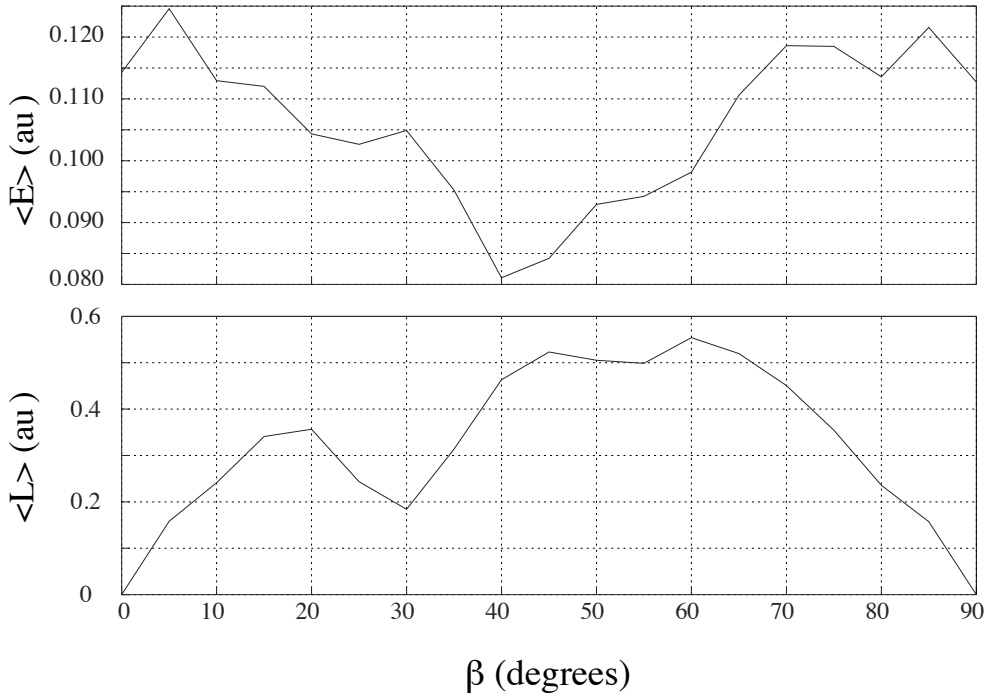

Figure 4.4: (Top) Average energy (in au); (bottom) average angular momentum (in units of $\hbar$) absorbed by the ring in the whole laser shot versus the polarization parameter β in degrees. The relevant parameters used for the calculations are $I_L = 4 \cdot 10^{14}$ W/cmâĹŠ^2 , $\lambda_L = 591$ nm ($\hbar\omega_L = 2.1$ eV)

important parameter both for fundamental and technological reasons. Its analytical determination has been shown to be laborious in the simple two-level system [11]; in nanorings its position and extension is intriguing but as yet unexplained.

Fig. (4.4) shows the averaged energy $\langle E \rangle$ absorbed by the ring and the averaged absorbed angular momentum $\langle L_z \rangle$. Again the previously shown trend is confirmed although the averaged absorbed angular momentum does not show the previous plateau as a function of the polarization parameter β. One of the most interesting uses of HHG is the possibility of creating very short, isolated, pulses. To this goal several schemes have been developed; particularly attractive seems the use a driving laser field of time dependent polarization [20, 21]. In Tables (4.1 on the next page) and (4.2 on the following page) we list the polarization angles ψ and the eccentricity e_c versus the order of the emitted harmonic. It is clear from the data that the polarization state of any harmonic is controlled by the polarization state of the pumping field. This feature can be of great use in the synthesis of short harmonics via the

$\beta \downarrow n \rightarrow$	1	3	5	7	9	11	13	15	17	19	21
0	$\binom{0}{0}$	$\binom{0}{0}$	$\binom{0}{0}$	$\binom{-}{-}$	$\binom{0}{0}$	$\binom{0}{0}$	$\binom{0}{0}$	$\binom{0}{0}$	$\binom{0}{0}$	$\binom{-}{-}$	$\binom{-}{-}$
5	$\binom{0}{0.54}$	$\binom{-}{-}$	$\binom{90}{0.12}$	$\binom{89}{-0.1}$	$\binom{103}{-0.36}$	$\binom{-}{-}$	$\binom{-}{-}$	$\binom{3}{0.45}$	$\binom{-}{-}$	$\binom{-}{-}$	$\binom{-}{-}$
10	$\binom{1}{0.69}$	$\binom{5}{-0.16}$	$\binom{94}{0.09}$	$\binom{91}{0.28}$	$\binom{88}{0.13}$	$\binom{-}{-}$	$\binom{-}{-}$	$\binom{-}{-}$	$\binom{0}{-0.36}$	$\binom{-}{-}$	$\binom{-}{-}$
15	$\binom{2}{0.6}$	$\binom{-}{-}$	$\binom{101}{0.64}$	$\binom{-}{-}$	$\binom{-}{-}$	$\binom{-}{-}$	$\binom{20}{0.25}$	$\binom{4}{0.6}$	$\binom{124}{0.62}$	$\binom{72}{0.61}$	$\binom{50}{0.54}$
20	$\binom{1}{0.65}$	$\binom{13}{-0.28}$	$\binom{176}{-0.76}$	$\binom{86}{0.5}$	$\binom{78}{-0.45}$	$\binom{-}{-}$	$\binom{178}{-0.19}$	$\binom{2}{0.25}$	$\binom{159}{-0.48}$	$\binom{99}{-0.08}$	$\binom{99}{-0.24}$
25	$\binom{1}{0.83}$	$\binom{1}{0.76}$	$\binom{165}{-0.01}$	$\binom{89}{0.5}$	$\binom{106}{0.08}$	$\binom{-}{-}$	$\binom{3}{0.36}$	$\binom{5}{0.56}$	$\binom{20}{0.7}$	$\binom{65}{-0.05}$	$\binom{60}{-0.43}$
30	$\binom{1}{0.93}$	$\binom{8}{0.9}$	$\binom{175}{0.47}$	$\binom{87}{0.63}$	$\binom{99}{-0.42}$	$\binom{-}{-}$	$\binom{-}{-}$	$\binom{17}{0.12}$	$\binom{-}{-}$	$\binom{-}{-}$	$\binom{-}{-}$
35	$\binom{0}{0.97}$	$\binom{1}{0.98}$	$\binom{172}{0.45}$	$\binom{88}{0.88}$	$\binom{96}{0.95}$	$\binom{-}{-}$	$\binom{-}{-}$	$\binom{-}{-}$	$\binom{-}{-}$	$\binom{-}{-}$	$\binom{-}{-}$
40	$\binom{0}{0.99}$	$\binom{4}{1}$	$\binom{5}{0.82}$	$\binom{43}{0.85}$	$\binom{-}{-}$	$\binom{-}{-}$	$\binom{-}{-}$	$\binom{-}{-}$	$\binom{-}{-}$	$\binom{-}{-}$	$\binom{-}{-}$
45	$\binom{103}{1}$	$\binom{-}{-}$	$\binom{-}{-}$	$\binom{-}{-}$	$\binom{-}{-}$	$\binom{-}{-}$	$\binom{-}{-}$	$\binom{-}{-}$	$\binom{-}{-}$	$\binom{-}{-}$	$\binom{-}{-}$

Table 4.1: Polarization angle ψ (up value in $\binom{0..}{0..}$) and eccentricity e_c (bottom value in $\binom{0..}{0..}$) versus the order n of the harmonic for different value of the parameter β. The relevant parameters of the calculations are $\lambda_L = 591$ nm ($\hbar\omega_L = 2.1$ eV), $I_L = 4 \cdot 10^{14}$ W cm^{-2}. The not given values are for harmonics not present in the spectrum.

control of the polarization state of the pump field. Preliminary results show that the harmonic radiation of nanoring can be synthesized to give pulses duration $\sim 1/10$ oc. The described effects are robust against modification of duration and shape of the pulse. We obtained the response of the nanoring to trapezoidal pulses with duration 16 and 64 oc and checked that the spectrum is essentially unchanged by this parameter. Instead the use of a gaussian or sin^2 pulse with 32 oc makes the spectrum regularly noisier.

$\beta \downarrow n \rightarrow$	1	3	5	7	9
0	$\binom{0}{0}$	$\binom{-}{-}$	$\binom{-}{-}$	$\binom{0}{0}$	$\binom{-}{-}$
5	$\binom{6}{0.92}$	$\binom{87}{0}$	$\binom{111}{0.78}$	$\binom{163}{0.6}$	$\binom{-}{-}$
10	$\binom{76}{0.99}$	$\binom{81}{-0.35}$	$\binom{88}{0.73}$	$\binom{26}{0.99}$	$\binom{37}{0.77}$
15	$\binom{87}{0.9}$	$\binom{87}{0.52}$	$\binom{90}{0.91}$	$\binom{144}{1}$	$\binom{51}{0.96}$
20	$\binom{89}{0.77}$	$\binom{86}{0.97}$	$\binom{6}{0.95}$	$\binom{160}{0.93}$	$\binom{-}{-}$
25	$\binom{91}{0.43}$	$\binom{76}{1}$	$\binom{86}{0.16}$	$\binom{16}{0.93}$	$\binom{-}{-}$
30	$\binom{1}{-0.62}$	$\binom{4}{0.88}$	$\binom{93}{0.88}$	$\binom{150}{0.96}$	$\binom{-}{-}$
35	$\binom{91}{0.08}$	$\binom{92}{0.89}$	$\binom{-}{-}$	$\binom{-}{-}$	$\binom{-}{-}$
40	$\binom{89}{0.96}$	$\binom{92}{1}$	$\binom{-}{-}$	$\binom{-}{-}$	$\binom{-}{-}$
45	$\binom{153}{1}$	$\binom{-}{-}$	$\binom{-}{-}$	$\binom{-}{-}$	$\binom{-}{-}$

Table 4.2: Polarization angle ψ (up value in $\binom{0..}{0..}$) and eccentricity e_c (bottom value in $\binom{0..}{0..}$) versus the order n of the harmonic for different value of the parameter β. The relevant parameters of the calculations are $\lambda_L = 591$ nm ($\hbar\omega_L = 2.1$ eV), $I_L = 4 \cdot 10^{14}$ W cm^{-2}. The not given values are for harmonics not present in the spectrum.

4.4 Conclusion

Nanoparticles such as buckyballs, nanotubes and rings are molecules of, possibly, large dimensions. Their shape presents interesting symmetries that can be exploited to obtain information on their behavior; these symmetries are particularly at hand when dealing with a laser illuminating the material; actually it seems that the field can be as strong as to make not useful a detailed knowledge of the bare states of the molecules. The impressive simplicity of treatment possible for buckyballs and rings [2, 22] shows the opportunity to seek for models giving a quick crop of reliable information; the comparison with experiments [3] conforts and strengthens the hopes.

Rings driven by a laser can efficiently emit an electromagnetic field endowed of interesting properties. We have seen. first of all, that the spectrum of the emission is wider than expected from atoms and that the cutoff law is quite similar to the cutoff law for buckyballs; then, that the characteristics of the harmonic field can be controlled by changing the laser parameters. In particular, our investigations show that the polarization of the driving laser provides a fine tool of control; as a result, the polarization of the diffused harmonics can be tuned.

Preliminary results show that within our model nanorings are suitable to emit a train of short electromagnetic pulses obeying a scaling law for the duration similar to the one for buckyballs; our simulations reveal a peculiar dependence of the train upon the laser polarization that cannot be reported here to keep this work within a reasonable limit. An interesting point is the fact that non zero angular momentum can be stored in the ring; a point to be developed in future research is the determination of the optimal pulse profile to maximize the storage. Since the equation of motion of the electron in the nanoring and of a rigid rotator are the same, the output of these study can cast light on the problem of setting in motion a molecule with a definite angular velocity.

Experiments have been carried out on the second harmonic generation of a thin silver sheet [23] with a matrix of geometrical nanoholes. A small area of graphene can be seen as a collection of holes or of tangent nanorings and therefore our model

calculations receive from these results confirmation and impetus.

We have elected to describe the laser pulse as a superposition of two orthogonal pulses of the same shape $f(t)$ [Eq. (4.1 on page 46)] but of course time dependent polarization state of the driver opens a wide range of possibilities all foreshadowing interesting channels to be explore

5 Nanorings driven by a two-color laser field

5.1 Introduction

In this chapter we use a model of nanoring driven by two orthogonal laser fields of angular frequency ω_x and ω_y, with $\omega_y = 2\omega_x$, and ω_x resonant between the ground state and the first excited state. We chose this ratio of the two laser photon frequencies because in calculations not shown in this thesis we obtained more harmonics with respect to other configurations.

Our system is composed by one electron constrained on a circumference. We calculate the emission and the polarization of the emitted harmonics. The origin of the harmonic generation is based in the non linearity of the electron-laser interaction energy. This non linear interaction forces the molecule to emit a wide spectrum of harmonics of the pumping field. Several studies have shown that a two color field can enhance considerably the harmonic yield [24, 25, 26, 27].

The study of the emission properties of a ring driven by a quasi-periodic train of electromagnetic half-cycle pulses is shown in [28], where it is shown that a sequence of pulses induces a non-equilibrium charge polarization. The charge oscillation generates an electromagnetic emission that can be tuned by changing the shape and the intensity of the pulses. In [29] it is shown that the presence of an impurity influences the polarization of the emitted harmonics and allows the HHG in the terahertz range.

Recently we obtained encouraging results using an elliptically polarized laser field [30]. In that work we studied the dynamics of a nanoring driven by a strong laser field

in different states of polarization obtaining spectra up to 21th harmonic. With this model, using two laser fields, we obtain spectra up to 51th harmonic. Then this is a good method for controlling the harmonic emission. We turn on the two lasers at two different instants so that the two pulse shapes are shifted. Then we perform a Gabor analysis on the total spectrum to study the contribution that the two individual lasers give to the spectrum.

Finally we study the angular momentum and the energy acquired by the electron and we show that the electron stores a residual angular momentum after we turn off the laser.

5.2 Theory

The system is composed by one electron constrained over a circle of radius R driven by two laser fields on its plane (the $x-y$ plane), with angular frequency ω_x and $\omega_y = 2\omega_x$. The laser along the x axis is taken n-photon resonant between the ground state and the first excited state. We made this choice because the combination of two lasers, consisting of the fundamental and the second harmonic, enhances the harmonic signal, compared with the case when only one laser [31, 32] is present. Total electric field, Hamiltonian and wave function are the same of the precedent chapter.

From the state $\mid t\rangle$ we calculate the dipole moment $\vec{\mathcal{D}}$ and the emitted spectrum of high harmonics, the absorbed angular momentum L_z and the absorbed energy E as a function of the time and of the angle β:

$$\vec{\mathcal{D}} = \sum_{m=-\infty}^{+\infty} \left[\hat{\epsilon}_x \Re\left(a^*_{m-1} a_m\right) + \hat{\epsilon}_y \Im\left(a^*_m a_{m-1}\right)\right] \tag{5.1}$$

$$E(t) \equiv \langle t \mid \mathcal{H}_0 \mid t\rangle = \sum_{m=-\infty}^{+\infty} |a_m(t)|^2 \hbar\omega_m \tag{5.2}$$

$$L_z(t) = \sum_{m=-\infty}^{+\infty} |a_m(t)|^2 \hbar m \tag{5.3}$$

Of course $E(t)$ and $L_z(t)$ are related; in fact, we can write the absorbed energy as:

$$E(t) = \frac{\hbar^2}{2m_e R^2}\langle t \mid \hat{\ell}_z^2 \mid t\rangle = \frac{\hbar^2}{2m_e R^2}\left[(\Delta\ell_z)^2 + (L_z(t))^2\right], \tag{5.4}$$

where $\Delta\ell_z$ is the variance. The first term is related to the dispersion of the wave function and the second term to the net motion along the ring.

5.3 Results

In our calculations we use a nanoring with radius of $R = 2.7$ au and a laser intensity of $I \propto |\mathcal{E}_{0x}|^2 + |\mathcal{E}_{0y}|^2 = 4 \cdot 10^{14}$ W/cm^2. Since the gap between the energy levels increases linearly with $|m|$ the system of differential equations (eq. 4.12 on page 47) can be safely truncated for a sufficiently large integer $|m|$. In our calculations we use the states $m = -10, ..., 10$.

We introduced a delay time between the two laser fields to study the spectrum and harmonic yield as a function of the overlap between the two fields. From results not shown here we have seen that for $\mathcal{E}_{0y} > \mathcal{E}_{0x}$ we obtain a wider spectrum.

$$A_g(t_0;\omega) = \int_{-\infty}^{+\infty} A(t) e^{-(t-t_0)^2/(2\sigma^2)} e^{-i\omega t} dt \tag{5.5}$$

In Fig. 5.1 on the next page we show the spectra obtained using a laser field with $\hbar\omega_x = 0.38$ eV and $\hbar\omega_y = 0.76$ eV when we turn on the second laser 0, 12, 28 and 32 optical cycles (oc) after the first laser. We used a trapezoidal pulse shape of 32 oc with 4 oc ascent and 4 oc descent. From these spectra we can see that, shifting the second pulse shape, the spectrum varies considerably; in particular with a delay of 28 optical cycles we obtain a richer and clean spectrum where in the first part we have mainly odd harmonics and in the second part of it we have even harmonics. However the laser intensity in the region of the overlapping is greater than other regions because we have the contribution of two laser fields. It is important to notice that when the two pulses are completely separate, the spectrum is very poor. Then we can deduce that even a small overlap of the two pulse shapes is sufficient to produce a rich spectrum of harmonics. The shape and the harmonic yield of the spectrum can be strongly manipulated by changing the temporal shift between the two pulses within one optical cycle.

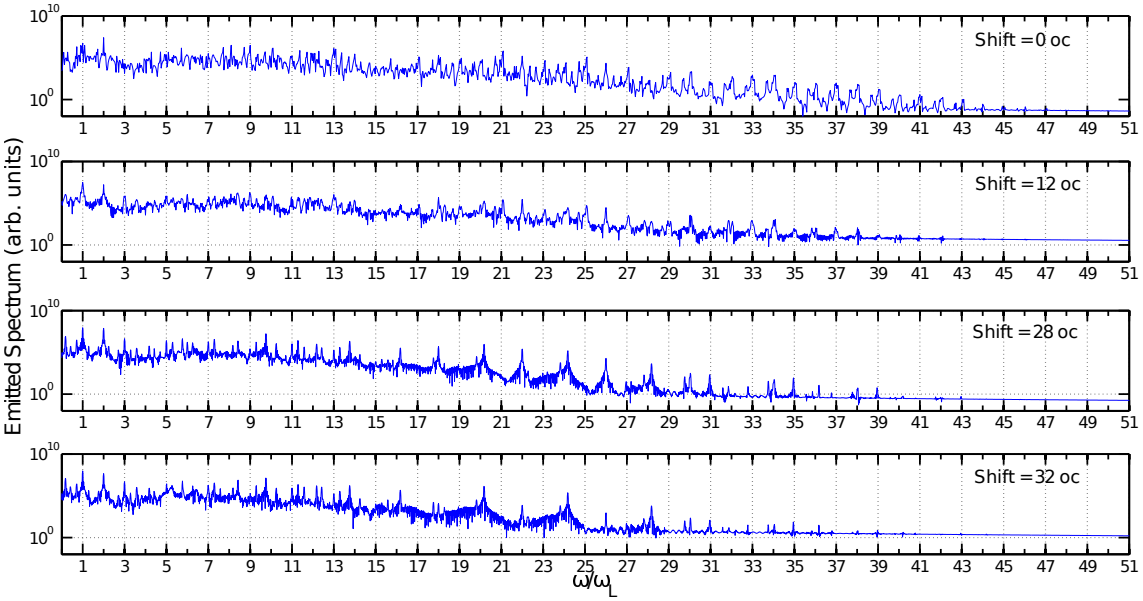

Figure 5.1: Dipole power spectra obtained using a laser field with $\hbar\omega_x = 0.38$ eV, that corresponds to 5 resonance photons between the ground state and the first excited state, $\hbar\omega_y = 0.76$ eV and $\beta = 65°$. We show the spectrum when we turn on the second laser 0, 12, 28 and 32 optical cycles after the first laser. For each laser we used a trapezoidal shape pulse of 32 oc with a 4 oc ascent and a 4 oc descent.

In Fig. 5.2 on the facing page (left) we show the spectra with two different shifts. It is clear the possibility of control given by a judiciously choice of the shift. In Fig. 5.2 on the next page (right) we show the spectrum obtained using only one laser with angular frequency ω_x (top) and, using only one laser with with angular frequency ω_y (bottom). We notice that the sum of the two spectra generates a total spectrum with more harmonics and this is a good result because we can think to generate a large spectrum using two lasers that individually would generate few harmonics. To understand the contribution given by each laser field at different instants, we performed a Gabor analysis of our data. The Gabor transform of a signal $A(t)$ is defined in [33]:

$$A_g(t_0;\omega) = \int_{-\infty}^{+\infty} A(t) e^{-(t-t_0)^2/(2\sigma^2)} e^{-i\omega t} dt \tag{5.6}$$

and can be interpreted as giving the spectrum of a signal as seen through a temporal window centered at t_0 and width σ; in the present calculations always $\sigma = 5$ oc.

We show the Gabor analysis to the case $\hbar\omega_x = 0.38$ eV, $\hbar\omega_y = 0.76$ and a 28 oc temporal shift between the two pulses. In Fig. 5.3 on page 62 we compare the Gabor spectra taken during the first and the second part of the pulse with the spectra emitted

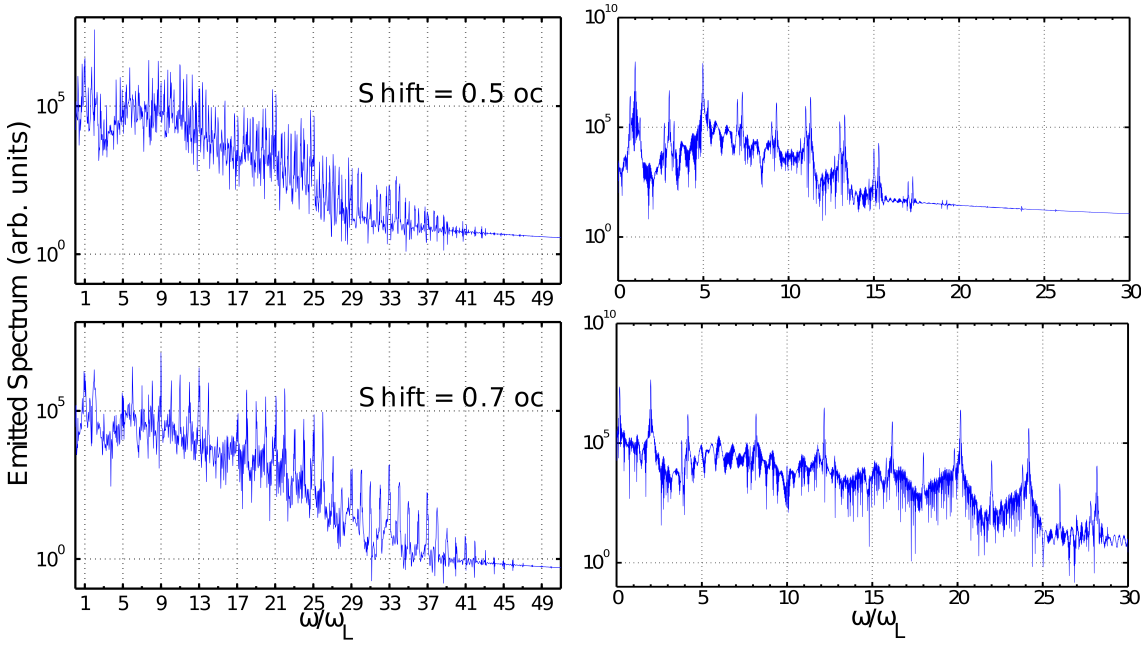

Figure 5.2: Left:Dipole power spectra obtained using a laser field with $\hbar\omega_x = 0.38$ eV, $\hbar\omega_y = 0.76$ eV and $\beta = 65°$. We show the spectrum when we turn on the second laser 0.5 oc and 0.7 oc after the first laser. Right: (top) Harmonics spectra obtained using solely a laser field with $\hbar\omega_x = 0.38$ eV (top), $\hbar\omega_y = 0.76$ eV (bottom) and $\beta = 65°$.

by the ring when only one laser is present. The first part of the spectrum, before the 15th harmonics is generated by the first laser and the second part is generated by the second laser. Furthermore odd order harmonics are emitted when the first laser is active and even order harmonics when the second laser is active (of course even order harmonics are just odd harmonics of the second laser); the latter assertion is demonstrated in Fig. 5.4 on page 63 presenting the temporal evolution of two harmonics of opposite parity. Actually between 28 oc and 32 oc we can see the turning off and on of the odd and the even harmonics respectively. In Fig. 5.5 on page 64-Left we show the polarization of the emitted harmonics obtained using $\hbar\omega_x = 0.38$ eV, $\hbar\omega_y = 0.76$ eV and $\beta = 65°$ with a complete overlapping of the two shape pulses. In this figure we report the angle of the ellipse (top) and the eccentricity (bottom) of each emitted harmonic; they are the angle between the semi-major axes of the polarization ellipse and the x axis and its eccentricity. From calculations not shown in this thesis, we saw that these parameters are controlled by the intensity and the frequency of the

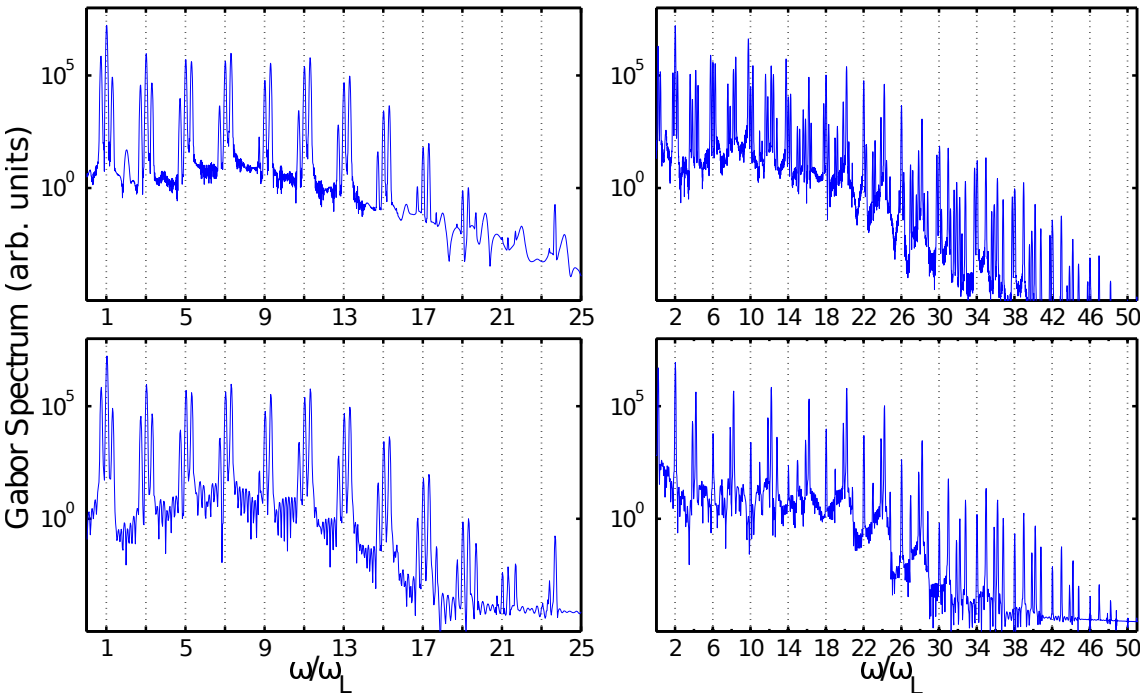

Figure 5.3: Gabor power spectra with $\sigma = 5$ oc, $\hbar\omega_x = 0.38$ eV and $\hbar\omega_y = 0.76$. Top row: the window is centred at $t_0 = 15$ oc (left) and at $t_0 = 43$ oc (right). Bottom row: Gabor spectrum obtained when only one laser along x axix is present (left) and when only one laser along y axix is present (right); the window is centred at 15 oc after the on switching of the laser field.

two laser. In Fig. 5.5 on page 64-Right we show the energy (top) and the angular momentum (bottom) absorbed by the laser field using $\beta = 50°$. We can see that the electron absorbs and emits energy periodically: this comportment is generated by a non uniform motion of the electron along the ring. We suspect that this uneven motion generates some of those spectral lines that are not harmonics. It is important to notice that in this configuration the electron stores a residual angular momentum.

5.4 Conclusions

Nanorings driven by a laser field can efficiently emit harmonics with a large spectrum, in fact a broad and dense spectrum is a prerequisite for the construction of short pulses since it could be used for linearly superposing waves within a suitable band [34]. In this chapter we have shown the possibility of controlling the emitted harmonics by changing parameters such as the laser intensity, the energy of the laser photon or the

shift between the shape pulses. In our calculations we chose the rate of the two laser field, $\omega_y = 2\omega_x$, in order to enhance the harmonic generation [31, 32].In particular we noticed that when the intensity of the laser along the y axis is greater than the one along the x axis, we can obtain a richer spectrum. We notice that the combination of two laser generates a spectrum with more harmonics respect to the case of only one laser.

We also studied the spectrum by varying the shift between the pulse shapes. In this case we noticed that it is sufficient a brief superposition of the pulse shapes to generate a wide spectrum. The best case is when the two pulse shapes share their tails. In this case we obtain a cleaner spectrum and harmonics clearly defined. To study the contribution of each laser to the total spectrum, we performed a Gabor analysis. From this analysis we noticed that the laser with angular frequency ω_x has a greater contribution in the first area of the total spectrum, about the first fifteen harmonics, and that it generates the odd harmonics. On the other hand the laser with angular frequency ω_y generates the even harmonics and has a greater contribution in the final area of the total spectrum. We noticed a great improvement to the spectrum by using a temporal shift within one optical cycle. This small shift leaves unchanged the position of the plateau. Thank to this behaviour, we have a fine control knob of the spectrum. Another important result is that we can control the polarization of the emitted harmonics and the angular momentum of the electron. The control of the polarization of the emitted harmonics is important for all application requiring radiation with a particular photon energy and polarization. We can imagine to create a laser that uses nanoring to obtain particular configurations of photon energy and

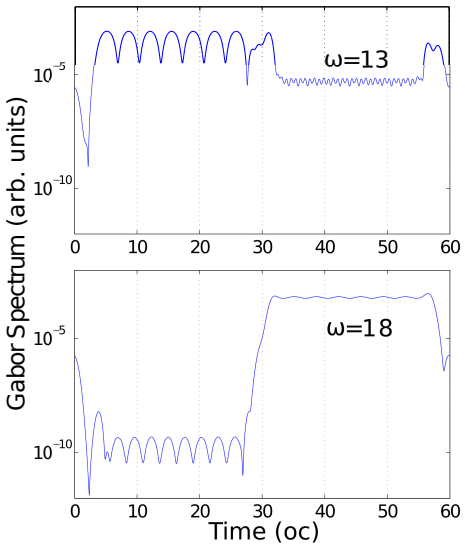

Figure 5.4: Time evolution of the 13th harmonic (top) and the 18th (bottom) relative to the spectrum with a shift of 28 oc and $\beta = 65°$. Parameters as in Fig. 5.1 on page 60.

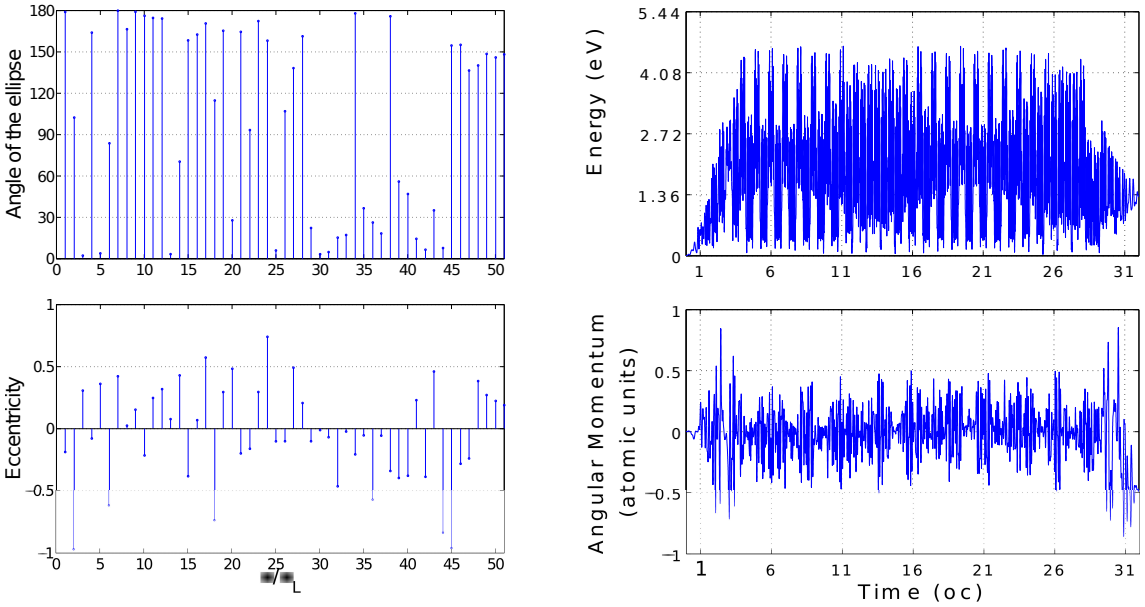

Figure 5.5: Left: Polarization of the harmonics emitted obtained using a laser field with $\hbar\omega_x = 0.38$ eV, $\hbar\omega_y = 0.76$ eV and $\beta = 65°$. On the top of this figure we show the angle of the polarization ellipses and on the bottom we show the eccentricity of the polarization ellipses. The negative sign of the eccentricity denote reverse rotation direction of the laser field. **Right:** Energy absorbed (top) by the electron and angular momentum absorbed (bottom) by the electron as a function of time using a laser field with $\hbar\omega_x = 0.38$ eV, $\hbar\omega_y = 0.76$ eV and $\beta = 50°$.

polarization in output simply by changing the input parameters.

Finally we have shown that the nanoring can acquire a residual angular momentum and that it absorbs and emits energy periodically . This periodical emission can generate some of those spectral lines that are not harmonics. With these last results we hope that the nanorings can be used to store angular momentum and use it in quantum information theory.

6 Nanoring as Logic Gate and memory mass device

6.1 Introduction

This chapter uses the knowledge gained in previous works to go in a new and interesting field, that of the quantum computation. In fact the rapid development of the nanosciences opens new technological frontiers. Computer science is one of them: by some years we are observing a saturation in the microprocessors performance which requires the finding of new objects that allow the construction of logic circuits faster and smaller than today's. For these reasons the research is focusing on a new kind of devices that show electrical and optical properties and that can be suitable to construct logic circuits: nanorings and graphenes are an example of them. They show interesting behavior in nanotechnology, optic and computer science thanks to their electrical and optical properties that make them apt to implementation in logic circuits.

The work that we discuss in this chapter deals with the possibility to use nanorings, driven by a laser field, as logical gates. Our system is composed by one nanoring, with only one active electron, driven by an elliptically polarized laser field. We calculate the harmonics and the Raman lines emitted and the angular momentum acquired by the electron in different states of polarization of the incident laser field. The process that we use is the high harmonic generation (HHG) [35, 36]. Several studies shows that the use of a two-color laser field or of a laser photon energy resonant between the ground state and the first excited state can enhance the emitted spectrum [3, 29, 31]. Then we calculate the HHG spectra and, from the use of the wavelet transform, we

recognize the presence of a signal composed by the first two harmonics and the Raman lines. We perform our calculations by varying the states of polarization of the incident laser field. We also calculate the angular momentum acquired by the electron in order to use it to create a truth table of logical operations and then to use the nanoring as a logic gate. We give examples of implementation of nanoring to construct a basic logic circuit such as the half and the full-adder. We can also construct a reversible logic gate, the Toffoli gate, using two nanorings. Finally we discuss the possibility of constructing a memory mass device using an array of nanorings.

6.2 Theory

In our system we consider the same past model of nanoring of radius R in the single active electron approximation driven by one laser elliptically polarized along the same plane. The dipole moment of the system is:

$$\begin{aligned} \vec{\mathcal{D}} &= e\vec{r}(t) = \hat{\epsilon}_x\langle t \mid x \mid t\rangle + \hat{\epsilon}_y\langle t \mid y \mid t\rangle = \\ &= \sum_{m=-\infty}^{+\infty}\left[\hat{\epsilon}_x\Re\left(a_{m-1}^* a_m\right) + \hat{\epsilon}_y\Im\left(a_m^* a_{m-1}\right)\right] \end{aligned} \tag{6.1}$$

where $\vec{r}$ is the position of the electron. The angular momentum acquired by the electron is:

$$L_z(t) = \sum_{m=-\infty}^{+\infty} |a_m(t)|^2 \hbar m, \tag{6.2}$$

and the correspondent time averaged angular momentum is:

$$\langle L_z\rangle = \frac{1}{T}\int_0^T L_z(t)\mathbf{d}t. \tag{6.3}$$

From the angular momentum we can define the magnetic momentum as $\vec{m} = \gamma\vec{L}$, with γ the gyromagnetic ratio of the electron.

6.3 Results

In our calculations we use different configurations of laser intensity and laser photon energy. In particular we use laser intensities I_L in the range $10^{10} - 10^{14}$ W/cm^2 and laser energy $\hbar\omega_L$ in the range $0.1 - 2$ eV, that in wavelength correspond to 12398 nm and 620 nm, and a radius from $R = 2.7\ a_0$, like the radius of the aromatic group, until to $R = 100\ a_0$. In fact large value of radius require small energies of the laser photon and less laser intensity. Then the dependence upon the radius permits to engineer the nanoring to obtain particular transition energies and to make it flexible for various uses. In Fig. 6.1 (top) we show the final and the time averaged angular momentum versus the polarization angle with R=2.7 a_0, $\hbar\omega_L = 2$ eV and $I_L = 10^{14}$ W/cm^2. The time averaged angular momentum is calculated for each polarization angle using the Eq. 6.3. In this simulation we use a laser duration of 32 optical cycles (oc) with a trapezoidal pulse shape. To understand when a signal is present, we performed a Morlet wavelet analysis on the total spectrum. The Morlet mother wavelet is defined as:

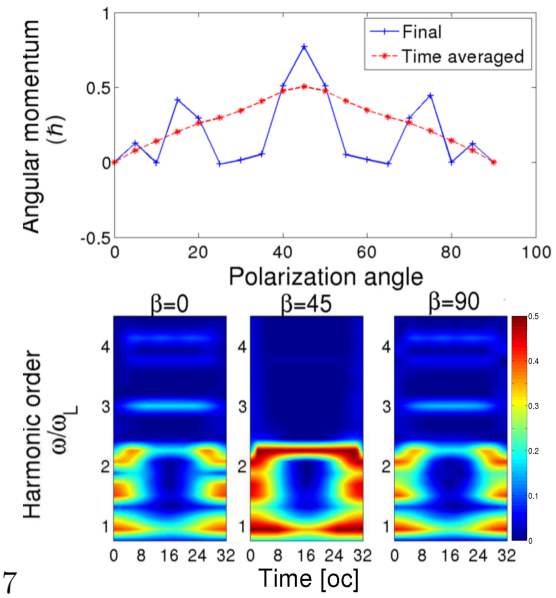

Figure 6.1: Top: Final (solid line) and time averaged (dashed line) angular momentum obtained with $\hbar\omega_L = 2$ eV and $I_L = 10^{14}$ W/cm^2 and R=2.7 a_0. Bottom: Morlet wavelet analysis of the dipole moment for $\beta = 0°, 45°, 90°$.

$$\mathcal{M}(x) = \left(e^{-ix} - e^{-\frac{\sigma_0^2}{2}}\right) e^{-\frac{x^2}{2\sigma_0^2}} \tag{6.4}$$

where σ_0 is a parameter that indicates the time-frequency resolution of the integration [37]. In our calculation, we chose $\sigma_0 = 6$, that correspond to 6 oscillations of the signal within the Morlet wavelet shape. We indicate with H_1 and H_{II}, the first two odd harmonics of the spectrum and with H_{R1} and H_{R2} the signals corresponding to the Raman transitions located near the first

and the second even harmonics of the HHG spectrum. In fact by the Eq. 5.2 we have $\hbar\omega_1 = 1.9$ eV, $\hbar\omega_2 = 7.6$ eV, $\hbar\omega_3 = 17$ eV, then we can define the signal H_{R1} as the transition between the virtual level with energy of $2\hbar\omega_1 = 3.8$ eV and the ground state, and signal H_{R2} as the combination of two Raman transition: $\hbar\omega_2$ and $\hbar\omega_2 + \hbar\omega_1 = 9.4$ eV. The Raman transitions depend upon the radius of the nanoring, we chose the value R=2.7 a_0 in order make the system comparable to a single cell of graphene or an aromatic group.

$\mathcal{E}_{x,y}$	H_I	H_{II}	H_{R1}	H_{R2}	L_z
0 0	0	0	0	0	0
1 0	1	1	1	1	0
0 1	1	1	1	1	0
1 1	1	0	1	0	1
$L = 0$	OR	XOR	OR	XOR	AND

Table 6.1: Truth table: in input we have the laser states $\mathcal{E}_{x,y}$ and in output we have the first two odd harmonics, the Raman transitions and the final angular momentum.

In Fig. 6.1 (bottom) we show the wavelet analysis for $\beta = 0°, 45°, 90°$. In this analysis the line H_{R1} is slightly shifted up the 4 eV by the presence of a non Raman line. In fact if within the oscillations in σ_0 we have several lines, the final value of the wavelet is shifted towards the more intense line. Now we create a truth table where we associate the values 1 and 0 to the polarization states of the incident laser field and to the presence or absence of signals. In particular we can divide the elliptical polarized laser into two components: $\mathcal{E}_x$ parallel to the x axis and $\mathcal{E}_y$ parallel to the y axis. When the laser is off, we have the state $\mathcal{E}_x = 0$ and $\mathcal{E}_y = 0$ ($\mathcal{E}_{x,y} = (0,0)$); for $\beta = 0° \rightarrow \mathcal{E}_{x,y} = (1,0)$, for $\beta = 90° \rightarrow \mathcal{E}_{x,y} = (0,1)$ and for $\beta = 45° \rightarrow \mathcal{E}_{x,y} = (1,1)$. We also associate the value 1 when the system presents a final angular momentum L_z. In Tab. 6.1 we can see that the first odd harmonic and the H_{R1} line behave as a OR logic gate, the second odd harmonic and the H_{R2} line behaves as a XOR logic gate and L_z behave as a AND logic gate.

Now we study the system using two consecutive laser pulses. We use the first laser pulse, circularly polarized, as a pump ($\beta = 45°$) and the second laser pulse, elliptically polarized, to probe the system. We make this choice in order to prepare the system with an initial angular momentum. From the dashed line of Fig. 6.1 we can see that for $\beta = 45°$

we have a positive time averaged angular momentum and the emission of the first odd harmonic and the H_{R1} line (Fig. 6.1 (bottom-middle)). We obtain different results varying the sign of the initial angular momentum. In Fig. 6.2 we show the final and the time averaged angular momentum with different signs of the initial angular momentum: $L < 0$ (top) and $L > 0$ (bottom). In this simulation we used a laser duration of 64 oc where in the first 32 oc we prepared the system with an initial angular momentum in order to study the nanoring with different starting conditions. In Fig. 6.3 we show the respective wavelet analysis. If we have a positive initial angular momentum we obtain a BUFFER for the first odd harmonic, the H_{R1} line, and for the final angular momentum, a XOR logic gate for the second odd harmonic and a RESET for the H_{R2} line; if the initial angular momentum is negative, we obtain a BUFFER for the first odd harmonic and the H_{R1} line, an AND logic gate for the H_{R2} line and an OR for the second odd harmonic. These results are listed in the truth table of Tab. 6.2. We are aware that high values of the laser photon and intensity can present some difficulties in the applications. In fact is preferred to use these high values in a powder of nanorings or in a strip containing nanorings in order to generate harmonics in different regions containing nanorings. From this point of view, we consider the system with radius of $R = 2.7\ a_0$ as the inferior limit of validity of our model. In fact in other calculation, that now we will show, we decrease the laser intensity and the energy of the photon laser and increase the radius until 100 a_0. These new parameters are preferable for the constructions of logic port because there is not the risk of destroying the object. With large radii we obtain the same results. In Fig. 6.4 we show the wavelet transform using a radius of $R = 25$ and $R = 50\ a_0$ respectively, a laser intensity of 10^{10} W/cm^2 and

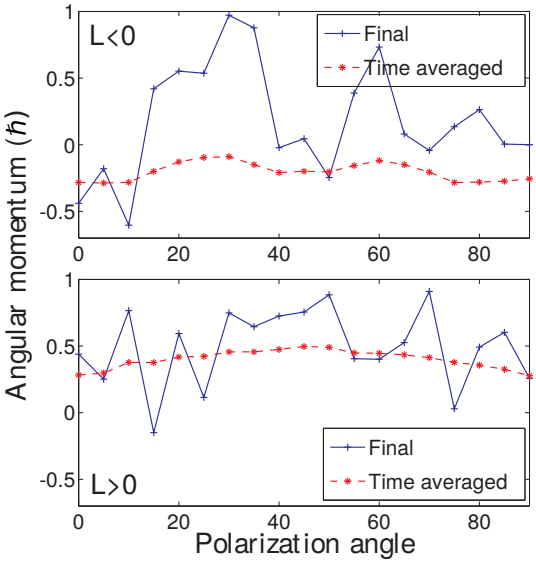

Figure 6.2: Final (solid line) and time averaged (dashed line) angular momentum obtained with $\hbar\omega_L = 2$ eV and $I_L = 10^{14}$ W/cm^2 and R=2.7 a_0. Initial angular momentum $L < 0$ (top) and $L > 0$ (bottom).

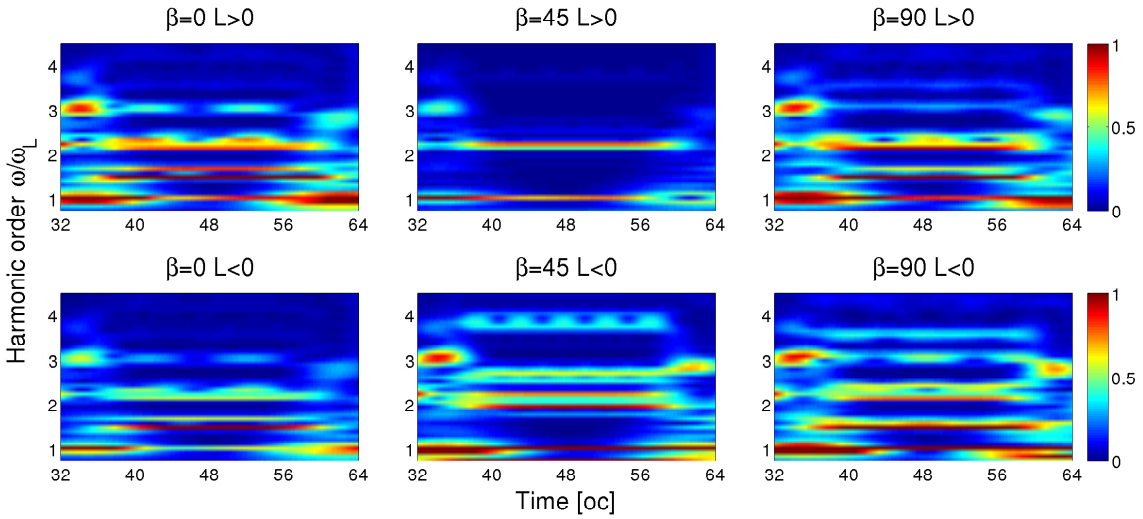

Figure 6.3: Morlet wavelet analysis of the dipole moment with $\hbar\omega_L = 2$ eV and $I_L = 10^{14}$ W/cm^2 and R=2.7 a_0 for $\beta = 0°, 45°, 90°$ and an initial angular momentum $L > 0$ (top line) and $L < 0$ (bottom line).

a laser photon of 0.1 eV and without an initial angular momentum. We can see that the structure of the emitted lines is the same but less defined. This because the harmonic spectrum present several non Raman lines that shift and enlarge the lines.

Now we show how nanorings can be arranged to form logic circuits. Examples of logical circuits are the half and the full adder. The half adder is a digital electronic component that has in input two bits ($\mathcal{E}_x$ and $\mathcal{E}_y$ in our case) and give in output their sum (S) and their carry (C). We can use the nanoring without initial angular momentum as an half adder using as output the second odd harmonic, the H_{R2} line and L_z (Tab. 6.3). Combining two nanorings, we have the possibility to make a full adder, where we use the carry of a previous summation. In fact we can use the harmonics obtained by one nanoring as input for a second nanoring etcetera. In this way we obtain a logic circuit with a set of concatenated nanorings.

6.3.1 Store information

We now suggested a way of using the nanoring to store information. When a nanoring is driven by a circular polarized laser field, the electron will round on it with a circular motion. This movement will generate a current I. If we call $\vec{S}$ the surface of the nanoring,

$\mathcal{E}_{x,y}$	H_1	H_{II}	H_{R1}	H_{R2}	L_z
0 0	1	0	1	0	1
1 0	1	1	1	0	1
0 1	1	1	1	0	1
1 1	1	0	1	0	1
L>0	BUFFER	XOR	BUFFER	RESET	BUFFER

$\mathcal{E}_{x,y}$	H_1	H_{II}	H_{R1}	H_{R2}	L_z
0 0	1	0	1	0	1
1 0	1	1	1	0	1
0 1	1	1	1	0	0
1 1	1	1	1	1	0
L<0	BUFFER	OR	BUFFER	AND	//

Table 6.2: Truth table: in input we have the laser states $\mathcal{E}_{x,y}$ with a initial positive angular momentum (top) and with a negative initial angular momentum (bottom). In output we have the first two odd harmonics, the Raman transitions and the final angular momentum.

the magnetic moment generated by the motion of the electron will be:

$$\vec{m} = I \int \mathrm{d}\vec{S}, \tag{6.5}$$

or, in terms of the angular momentum: $\vec{m} = \gamma \vec{L}$. If we have a planar array of nanorings and if $\vec{\sigma}$ is the surface of the laser spot containing several nanorings, the magnetic momentum generated will be proportionally to the summation of the the contributions of each nanoring within the laser spot surface (Fig. 6.5). Then we can use the nanoring to store information with the magnetic momentum. In these calculations we did not take into account the information decay.

When the nanoring is driven by a laser field in the state (1,1), it acquire an angular momentum and we obtain $L_z = 1$. Then if we use another laser pulses with inverse circular polarization, we obtain an angular momentum state $L_z = 0$; we can consider the angular momentum like a pseudo-spin.

These simple behaviours make the nanoring an interesting object to store information.

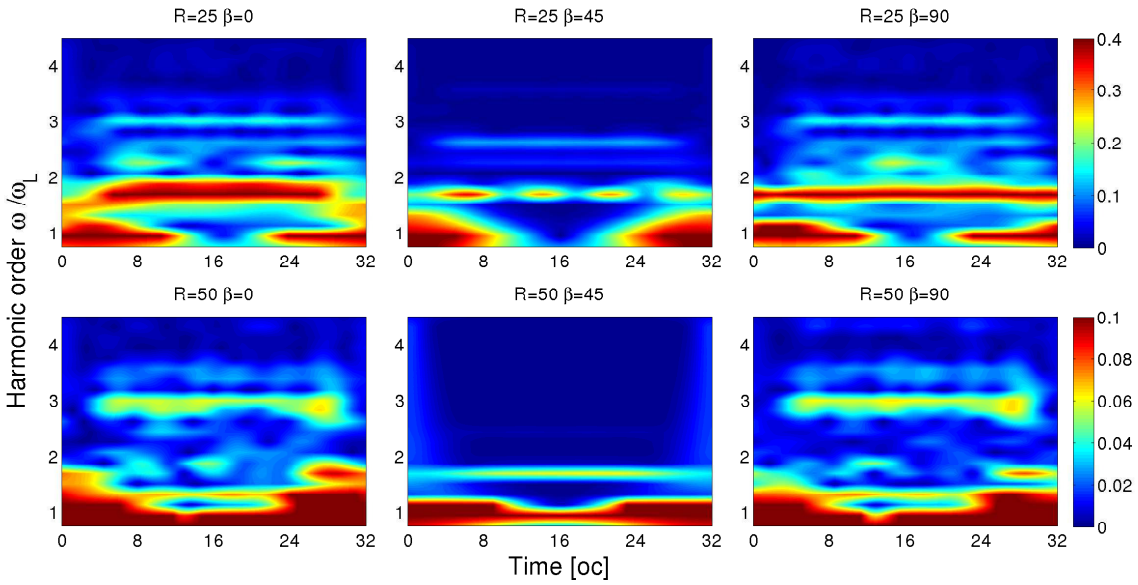

Figure 6.4: Morlet wavelet analysis of the dipole moment for $\beta = 0°, 45°, 90°$, a radius of $R = 25$ (top line) and $R = 50$ a_0 (bottom line), a energy of laser photon of 0.1 eV and an intensity of 10^{10} W/cm^2.

6.4 Conclusions

We can consider the nanorings a real alternative to modern logic components thanks to their size and speed.

We investigated the possibility to use nanorings driven by a laser field to make logic circuits. In particular we used the emitted signals and the final angular momentum of the nanoring to create logic gate that can be used to make logic operations. In fact we noticed the possibility to construct the XOR, OR and AND logic gates and use them to make a half and full adder. Combining two or more nanorings, we can obtain a full adder, but the presence of XOR and AND logic gates give us the possibility to make a Toffoli gate. The Toffoli gate is an universal reversible logic gate that permits to construct any reversible circuit. It has 3 bit inputs (a, b and c) and outputs and realizes the function c XOR (a AND b). In fact if we set the first two bits, the Toffoli gate inverts the

$\mathcal{E}_{x,y}$	Sum	Carry
0 0	0	0
1 0	1	0
0 1	1	0
1 1	0	1

Table 6.3: Truth table of the half adder: in input we have the laser states $\mathcal{E}_{x,y}$ and in output we have the values of the second odd harmonic and the H_{R2} line for the sum, and the values of L_z for the carry.

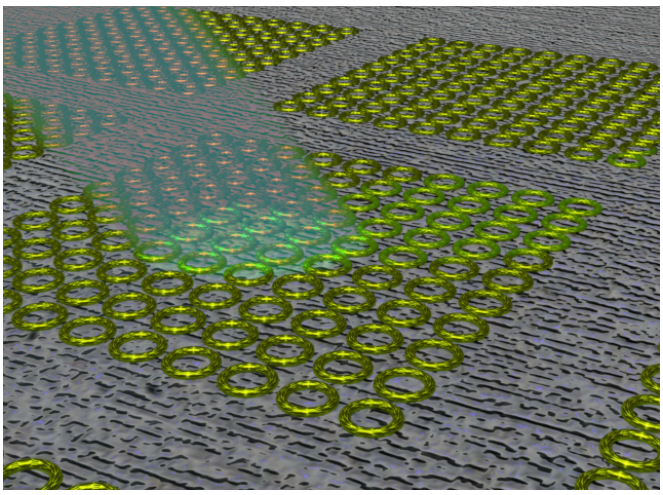

Figure 6.5: Schematic representation of array of nanorings used to store informations. When one array is driven by the laser field, it creates a magnetic moment that represents a bit.

third bit, otherwise all bits remain the same. Then it is possible to use the nanorings as a Toffoli gate and create any logic circuit. We also can use the angular momentum acquired by the electron in the nanoring to store information. In fact we can consider the final angular momentum like a pseudo-spin that can be reversed by changing the direction of circular polarization of the incident laser field. The entire process, including harmonics generation, Raman transitions, and angular momentum, takes about 10^{-15} seconds. In addition we can create cells of nanoring arrays and store informations on it using the laser to generate a magnetic moment. In this chapter we showed several simulations to study the system with different parameters, such as the radius, the energy of the laser photon and the intensity of the laser. In fact if we enlarge the radius and decrease the energy laser photon, we obtain the same results. If we think to construct a nanoring with a radius of 25 or 50 a_0, we can use a laser photon with energy ~ 0.1 eV and a laser intensity of $\sim 10^{10}$ W/cm^2.

7 Classical chaos and harmonic generation in laser driven nanorings

7.1 Introduction

In this chapter we study a quantum ring driven by an intense laser field that emits electromagnetic radiation stemming from the strong acceleration experienced by the active electrons. The shape of the spectrum is multiform and is ruled by the relevant parameters of the problem. In order to elucidate the physical origin of such a rich variety of spectra we study the comportment of one single classical charge constrained both on a unidimensional structured ring acted upon by a linearly polarized laser field. Our simulations show that the response of the ring evidences chaotic and unstable behaviour that can be at the origin of the variegated quantum results. Thus the model here discussed might cast light in the still obscure relation between classical chaos and quantum realm.

7.2 Theory

In the effort to penetrate the core of the problem, in this chapter we adopt a simple model of the system by removing details which might blur the understanding of the results. All approximations have been proved to be valid in the quantum treatment of HHG. Therefore we consider a model system in the single active electron approximation with one electron constrained to move along a one dimensional ring of radius R driven by a linearly polarized electric field. The presence of tangential forces acting on the

electron is explicitly considered with the introduction of a potential that structures the ring; for definiteness we investigate a model characterized by the presence of six potential wells regularly distributed along the circle that might mimic six atoms in a circle (such as a graphene cell) or, better, a structure introduced in the ring by the manufacturer; the quantal treatment of the system can be found in [38]. However it must be understood that the one presented in [38] and hereafter is a simple model meant to give information on the general comportment of an artificial slender annular system.

The classical Hamilonian of the electron on the ring is assumed to be

$$\mathcal{H} = \frac{\ell^2}{2I} + U_0 \cos(6\phi) + V_0 \cos(\phi) \sin(\omega_L t). \tag{7.1}$$

A small dissipative term proportional to $\dot{\phi}$ is added to the equation of motion to wash away any intrinsic instability of the undamped equations [39] and gives the Newton equation of motion

$$\ddot{\phi} = \frac{6U_0}{I} \sin(6\phi) + \frac{V_0}{I} \sin(\phi) \sin(\omega_L t) - 2\gamma\dot{\phi} \tag{7.2}$$

with ϕ the angular coordinate of the moving particle, ℓ the conjugate momentum (angular momentum), I the moment of inertia of the particle, $2U_0$ the depth of the structures, V_0 the maximum laser-particle interaction energy and ω_L the laser angular frequency. The equation of motion is non linear in ϕ at all orders and could introduce chaotic behaviour in the dynamics. For later use it is convenient to obtain the x component of the acceleration of the charge. Let $x(t) = R\cos(\phi)$ be the x component of the position of the charge, then the relative component of the acceleration is:

$$\ddot{x} = -R\Big[\ddot{\phi}\sin(\phi) + \dot{\phi}^2\cos(\phi)\Big]. \tag{7.3}$$

Since it is better to work with adimensional parameters, by defining the scaled time (or, loosely, time) $\tau = \omega_L t$, the equation of motion is equivalent to the two coupled first order differential equations:

$$\begin{cases} \phi' = \ell \\ \ell' + 2a\ell = u\sin(6\phi) + v\sin(\phi)\sin(\tau) \end{cases} \tag{7.4}$$

with $a = \gamma/\omega_L$, $u = 6U_0/(I\omega_L^2)$, $v = V_0/I\omega_L^2$ and the prime sign denoting derivative with respect to τ; the dynamical variables (ϕ, ℓ) form the phase space of the particle whose angular momentum is $L = I\omega_L\ell$. The set of differential equations must be solved with initial conditions $(\phi(0), \ell(0)) = (\phi_0, \ell_0)$.

In the three-step model (chap. 2.2.1), the cutoff energy is equal to the maximum kinetic energy of the electron and is released in the recombination step plus the energy of the ground state. Indeed our model can support a generalized picture of ionization and recombination of the electron: in principle it must not be excluded the possibility that the particle, initially confined in the neighborood of a particular potential well, under the action of the laser ends up its motion captured in the neighborhood of a different potential well. In the light of the previous discussion we also evaluate the kinetic energy in units of V_0:

$$K \equiv \frac{L^2}{2IV_0} = \frac{\ell^2}{2v}. \tag{7.5}$$

Let $\vec{p}(\tau)$ be the position of the electron in our adimensional phase space at the *instant* τ; we are interested in understanding how the trajectories of the electron are determined by the choice of the initial position $\vec{p}(0)$. The point at issue here is to understand if very close initial conditions result in very close final trajectories or not; in other words the point at issue is to determine if the equations of motion can have chaotic nature and, eventually, to delimit the areas of the input parameters which result in chaos. We leave to subsequent investigation of more realistic two dimesional systems a refined analysis.

As a first step we stroboscopically map in the phase space the trajectory points sampled at intervals $\Delta\tau = 2\pi$ for several choices of the initial condition $\vec{p}(0)$; we call the ensuing plot as Poincaré section. In the Poincaré section, the presence of regular patterns, accumulation and randomly distributed points discriminates periodic behaviour from attractors and chaotic behaviour [40, 39].

From the Larmor formula, we know that the power spectrum of the electromagnetic field emitted by the accelerating charge is proportional to $|A(\omega)|^2$ where $A(\omega)$ is the

Fourier transform of the dipole acceleration:

$$A(\omega) = \frac{1}{\sqrt{2\pi}} \int_{-\infty}^{+\infty} x''(\tau) e^{-i\omega\tau} d\tau; \tag{7.6}$$

consequently, for any simulation reported in this chapter, we provide the spectrum $|A(\omega)|^2$ versus the harmonic order.

7.3 Results

We have calculated the temporal evolution of the electron in the ring for several choices of the three load parameters a, u and v and for many choices of $\vec{p}(0)$, the initial position of the particle in the phase space. Since the number of possible outputs is huge, in what follows we show only few plots in order to provide the general information. Having in mind the HHG from the quantum counterpart of this classical model [38], we choose the values of the load parameters corresponding to a mesoscopic ring and to the lasers used in the laboratories. Therefore we always take $R = 10a_0$, with a_0 the Bohr radius, $\lambda = 1060$ nm corresponding to $\omega_L = 1.78 \cdot 10^{15}$ sec^{-1} ($\hbar\omega_L = 1.16$ eV) and $\gamma = 5 \cdot 10^{-3}\omega_L$. The initial reduced angular momentum ℓ_0 is an important load parameter which strongly affects the nature of the problem; in the following we always confine ourselves to the choice $\ell_0 = 0$. Throughout the work the laser intensity $\mathcal{I}$ has been taken within the lower side range of the value used in HHG experiments; in Table (7.1) the conversion between $\mathcal{I}$ and v can be found. The depth of the wells, when non-null, has been taken as $U_0 = 7.5 \cdot 10^{-2} e^2/a_0 = 2.04$ eV corresponding to $u = 2.4348$.

$\mathcal{I}$ (W cm^{-2})	v
10^{13}	0.9120
$4.7 \cdot 10^{13}$	1.9771
$4.72 \cdot 10^{13}$	1.9813
$4.74 \cdot 10^{13}$	1.9855
$5 \cdot 10^{13}$	2.0392
10^{14}	2.8839
$5 \cdot 10^{14}$	6.4486

Table 7.1: Laser intensities $\mathcal{I}$ in W cm^{-2} used throughout the calculations and corresponding values of the adimensional parameter v.

7.3.1 Plain ring

We begin by studying the case of the plain ring by setting $u = 0$; thus, in absence of laser all points of the ring are equivalent; when the laser field is active and polarized along the x axis, an electron at rest at $\phi = 0°$ and $\phi = 180°$ remains at rest. The most effective coupling between laser and electron is at $\phi = 90°$ and $\phi = 270°$ because at those points the laser field is tangent to the circumference. We present here few paradigmatic plots for $a = 5 \cdot 10^{-3}$ and discuss the characteristic features of the motion. For $v = 0.912$ generally speaking the Poincaré section presents three different attractors, mainly near $\phi_0 = 30°$, $\phi_0 = 90°$, $\phi_0 = 150°$, but also near the specular points $\phi_0 = 210°$, $\phi_0 = 270°$, $\phi_0 = 330°$ with different values of ℓ; this feature meaning that the motion has three different periods. It is also frequent the existence of only one attractor orbit; the transition from a type to a different type is abrupt. For example in Fig. (7.1) ($v = 0.912$) in the left column we show the Poincaré section for three different and close starting positions and in the right column the corresponding spectrum of the emitted electromagnetic radiation. The stroboscopic positions in the phase space, after some initial erratic behaviour which might induce the impression of randomness, finally settle down on accumulation points detected in the plots of left column from the larger density of representative points. Somehow surprisingly, the HHG spectrum of the radiation is formed by well resolved odd order harmonic lines together with spectral lines which in the quantal realm would be named hyper-Raman. All lines stem from a large and broad shape which often appears also in quantum calculation.

In Fig. (7.2) we show similar plots with a stronger field ($v = 2.0392$). The Poincaré sections reveals always two accumulation points reached after erratic exploration of the phase space; the Fourier power spectrum instead shows well resolved odd, even and half order harmonics stemming from the mentioned continuous background. Half integer harmonics are generally considered as pinpointing the insurgence of chaos. Since a larger value of v means a stronger laser-ring coupling, these different behaviours seem to be expected. It must be remarked that a periodic attractor is not reached always. When $\phi_0 = 30°$ (plots not shown) the stroboscopic points wanders all over the phase

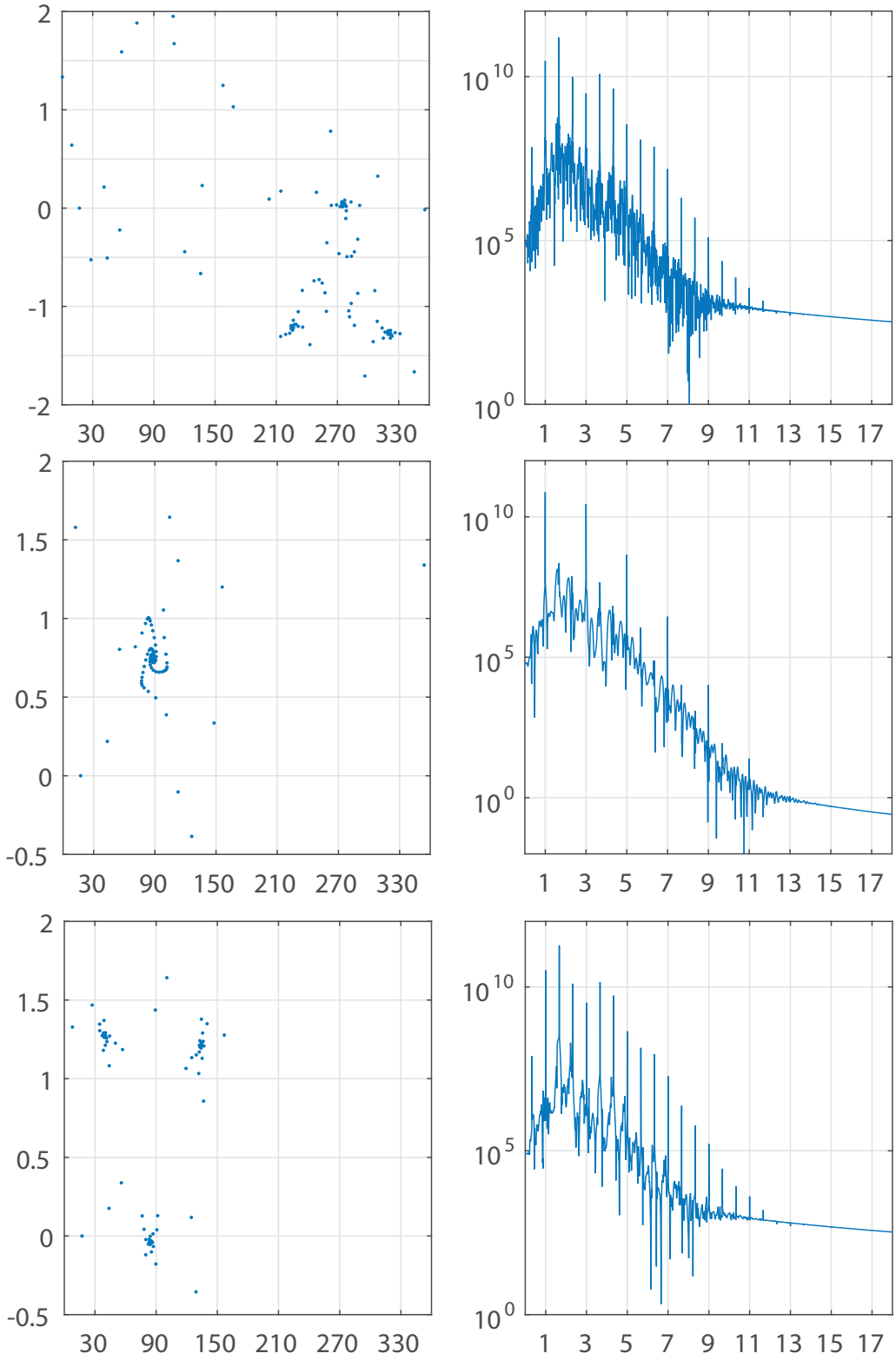

Figure 7.1: Left column: Poincaré section of the motion of the electron in a plain ring; abscissa ϕ (degrees); ordinate ℓ (diensionless). Right column, Fourier power spectrum of $\phi(\tau)$ (arb. un.) vs the harmonic order ω/ω_L. $u = 0$. Always the electron starts at rest. The starting points are: top $\phi_0 = 17°$, center $\phi_0 = 17.2°$, bottom $\phi_0 = 17.3°$; the calculations are carried out for 200 cycles. The values of the load parameters are $a = 5 \cdot 10^{-3}$, $u = 0$ and $v = 0.912$.

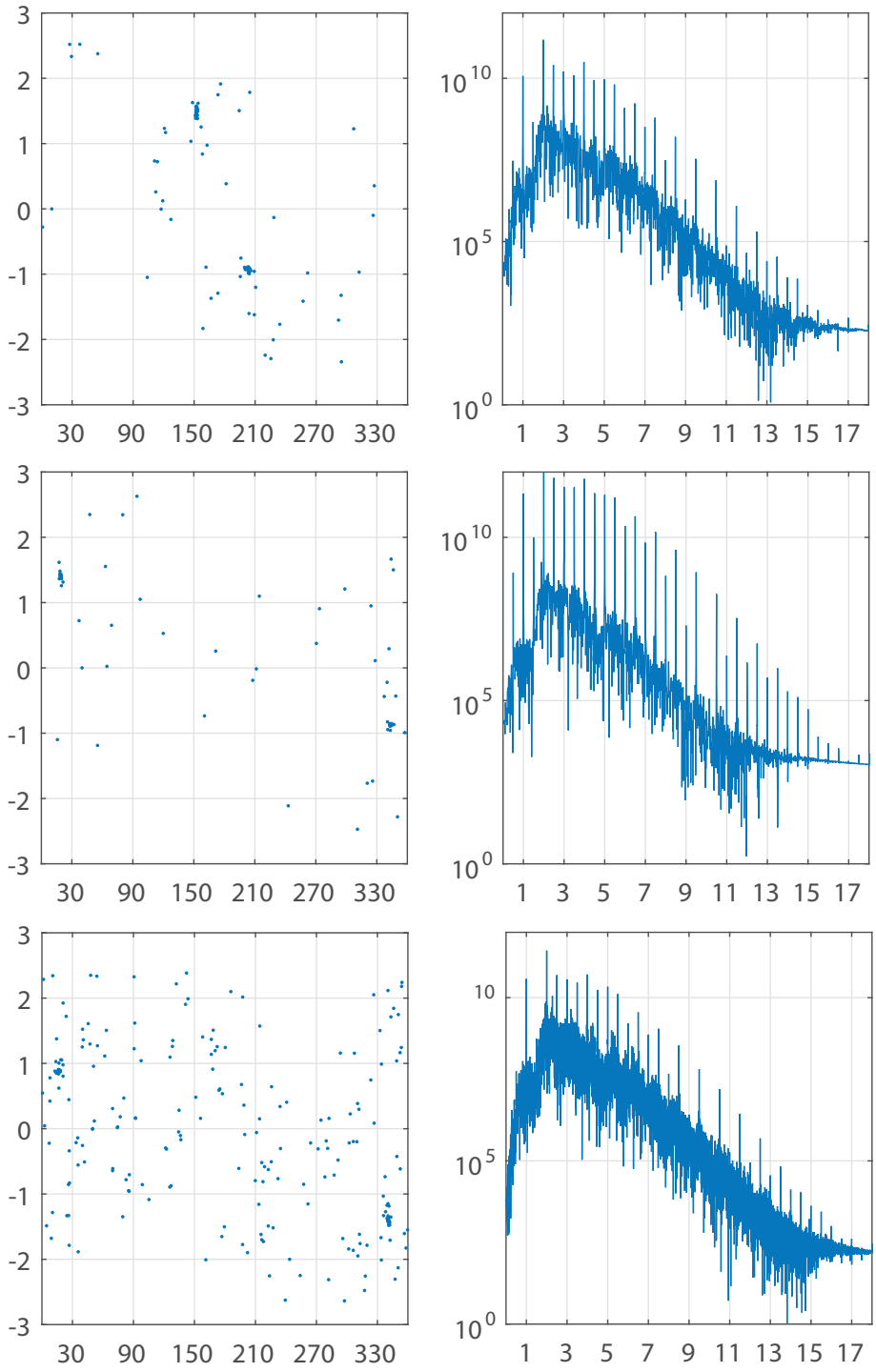

Figure 7.2: Left column: Poincaré section of the motion of the electron in a plain ring; abscissa ϕ (degrees); ordinate ℓ (diensionless). Right column: Fourier power spectrum of $\phi(\tau)$(arb. un.) vs the harmonic order ω/ω_L. $u = 0$. Always the electron starts at rest. The starting points are: top $\phi_0 = 10°$ (calculations carried out for 200 cycles); center $\phi_0 = 40°$ (calculations carried out for 800 cycles); bottom $\phi_0 = 50°$ (the calculations carried out for 400 cycles). The values of the load parameters are $a = 5 \cdot 10^{-3}$, $u = 0$ and $v = 2.0392$.

space and does not settle at any accumulation point fact reflected in a broad, dense and indistinct power spectrum.

Contradictory behaviour can be observed in Fig. (7.3) were the Poincaré section for two different values v, all other parameters being left constant, are shown. Unexpectedly, a chaotic behaviour is evident for the weakest v (first row); in spite of the fact that the Poincaré sections seem similar, the lower section ends at the accumulation point $(\phi, \ell) = (270°, -1)$. This characteristic has a match in the radiation spectrum which presents a comb of odd order harmonics in the second case.

We conclude that the plain ring exhibits chaotic behaviour which is reflected in broad and indistinct electromagnetic spectrum.

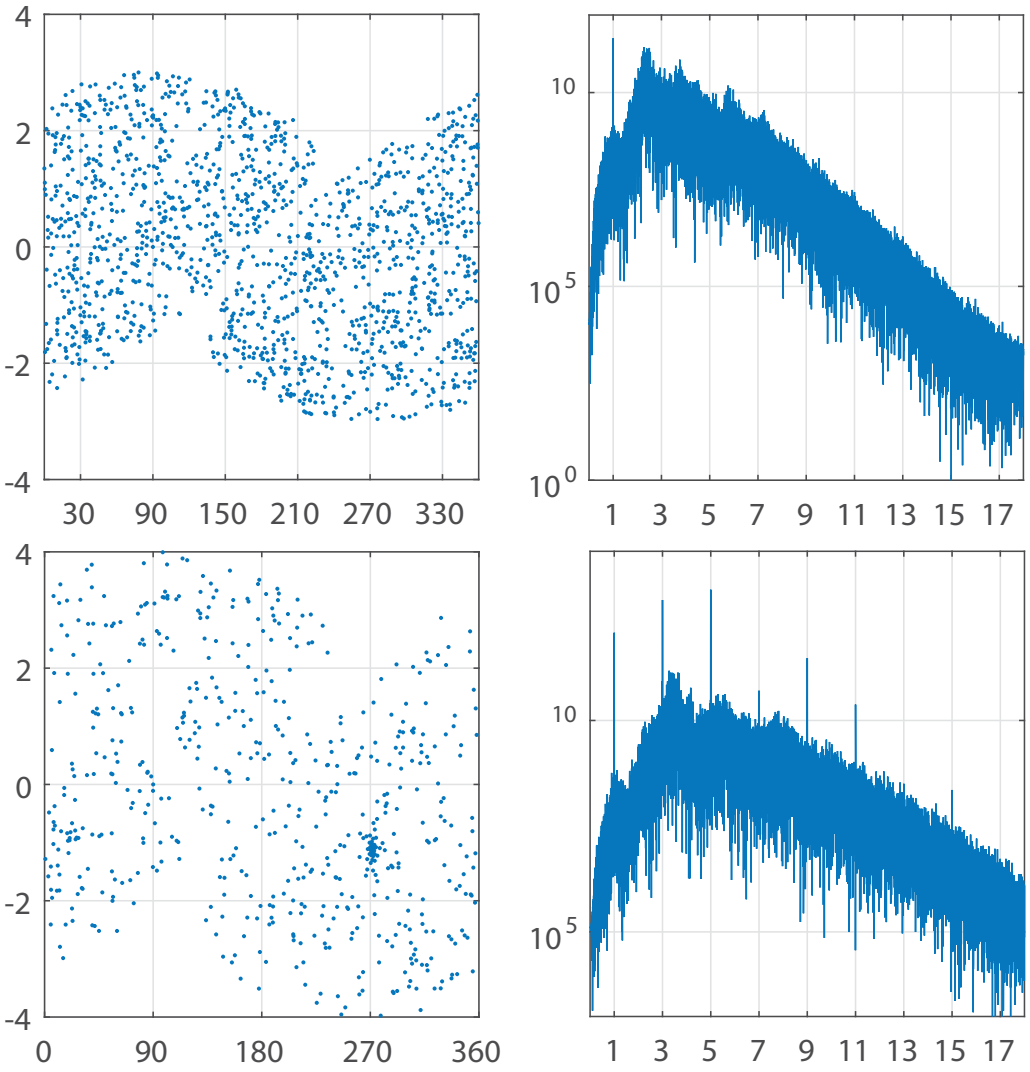

Figure 7.3: Left column: Poincaré section of the motion of the electron in a plain ring; abscissa ϕ (degrees); ordinate ℓ (diensionless). Right column: Fourier power spectrum of $\phi(\tau)$(arb. un.) vs the harmonic order ω/ω_L. $u = 0$. Always the electron starts at rest from $\phi_0 = 90°$; for both plots $a = 5 \cdot 10^{-3}$; the calculations are carried out for 1500 cycles. Top $v = 2.8839$ the phase space is filled and does not show periodicity. Bottom $v = 6.4486$ a late periodicity is evident.

7.3.2 Structured ring

In this paragraph we show how the equation of motion of the electron can be unstable against small variations of the parameters of the problem; this effect could be called parametric chaos.

We now structure the ring by releasing the condition $u = 0$; of course in this case the dynamics is much more complex than before.

In the absence of the laser, the system has six stable equilibrium points (at $\phi_n = 30° + n60°$ with $n = 0 \ldots 5$) and six unstable equilibrium points; our choice of a particle initially at rest would always result in a pendular, damped motion towards the closest stable position.

The introduction of an external laser field introduces variations to the theme. A weak enough laser can only push the electron toward an oscillation about the closest stable position. At intermediate intensity it can force the particle to rotate along the ring and, eventually, to finish its motion oscillating around a well other than the parent one. All of these options are determined by the actual value of the initial condition and of the parameters. Tiny changes on these values will induce different terminal states of motion.

In Fig. 7.4 we show the Poincaré section in three cases that start from very close initial position (9°, 10°, 11°) but result in a final different state of motion. The three simulations reach a different attractor in a rather dissimilar way. It is significative the central plot of Fig. 7.4: the attractor point is at $\phi = 150°$ which is reached for $\tau > 250$ cycles; the stroboscopic point moving in a chaotic way for most of the simulation finally settles into an attractor at $\phi = 150°$, however occasionally we have also observed death and revival of chaos. The power spectra are less ambiguous: they are equally noisy and indistinct. The particle that starts from the bottom of a potential well ($\phi_0 = 30°$) oscillates about this position and emits a well resolved spectrum; however if it starts from $\phi_0 = 90°$, where the laser coupling is mostly effective, then it quickly begins to rotate along the ring and eventually finishes captured by the well at $\phi_0 = 150°$. The reason of such a different behaviour is to be find in the fact that the laser is weak enough

to be unable to extract the particle from the parent well but in the most favorable case. We conclude that the motion of a laser driven electron in a structured ring is chaotic. The chaotic nature of the motion does not make easy any prediction on the total energy that can be absorbed by the ring during a full laser shot; heuristically we can say that the maximum energy that the electron can absorb from the field should be of the order of $2V_0$; we have numerically found that within the range of our values from Eq. (7.5) that $K \leq 2.8$.

Of course even a very stable laser field can present small fluctuations of the intensity during an actual shot or from shot to shot. The outcome of a particular output must be checked against such small fluctuation. From Fig. 7.5 we deduce that unfavorable cases can be found resulting in different physical behaviour. The top row of the figure shows a noteworthy effect. We have checked that the electron does not rotate along the ring: this fact is suggested, but not proved, by the appearance of the Poincaré section. Thus the laser is not intense enough to extract the electron from the parent well. The power spectrum is surprising: it shows a comb of odd harmonics which would be paradigmatic if obtained in a quantum framework.

Therefore we conclude that the equation of motion of the charge carrier can be unstable against small variations of the parameters of the problem; this effect could be called parametric chaos. In performing experiments care must be paid to choose parameters whose indetermination is within stability regions of the equation. The results of Fig. 7.5 have large physical relevance. From one hand, it warns against the risk to extract general physical interpretations from data obtained from experiments run with an unstable laser field. From the other hand, it points towards the possibility to control the output of an experiment by a fine tuning of the laser parameters.

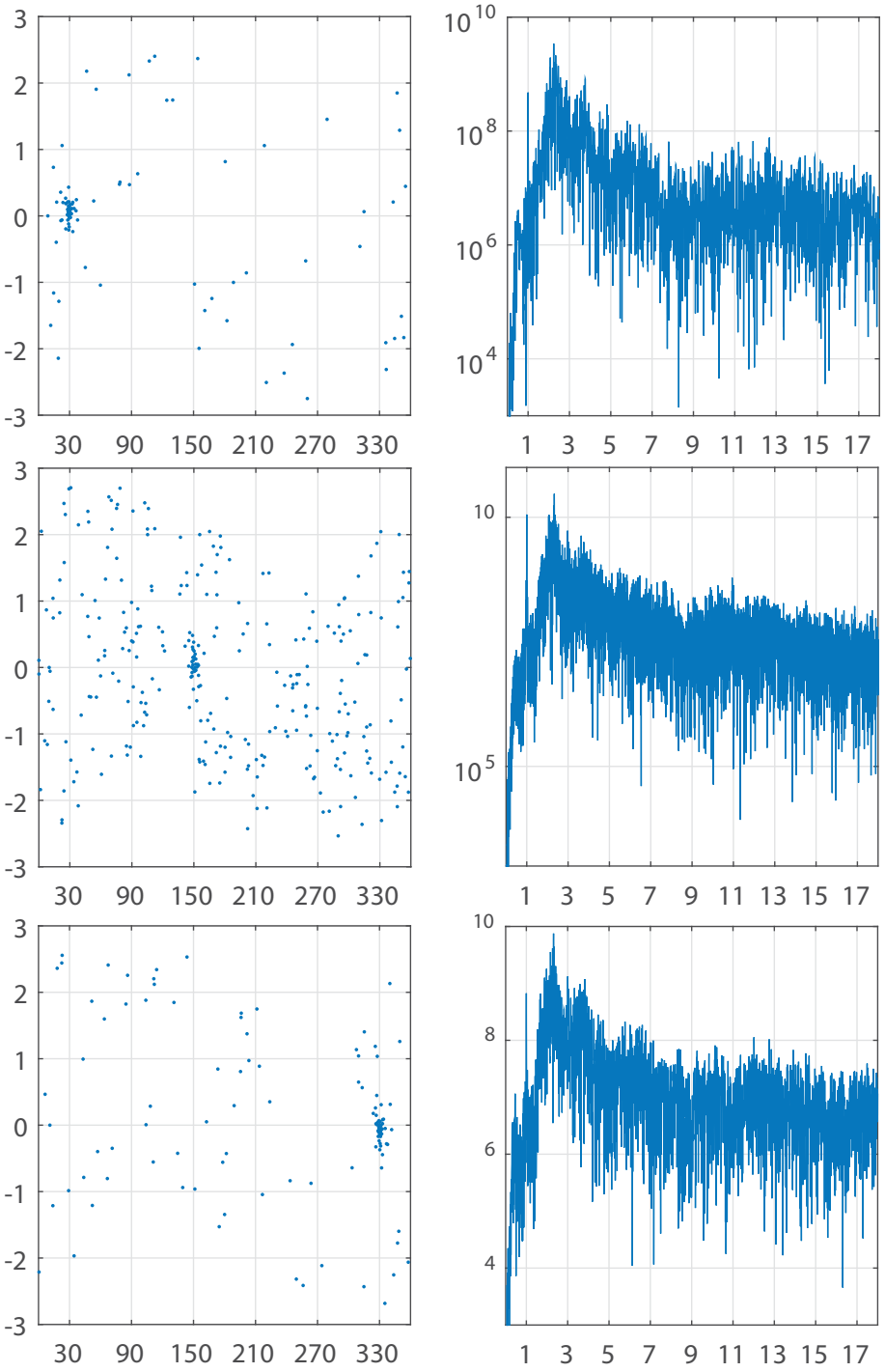

Figure 7.4: Left column: Poincaré section of the motion of the electron in a structured ring; abscissa ϕ (degrees); ordinate ℓ (diensionless). Right column: Fourier power spectrum of $\phi(\tau)$(arb. un.) vs the harmonic order ω/ω_L. $u = 0$. In all the three plots the electron starts at rest and calculations are carried out for 300 cycles. Top $\phi_0 = 9°$; center $\phi_0 = 10°$; bottom $\phi_0 = 11°$. The values of the load parameters are $a = 5 \cdot 10^{-3}$, $u = 2.4348$ and $v = 2.0392$.

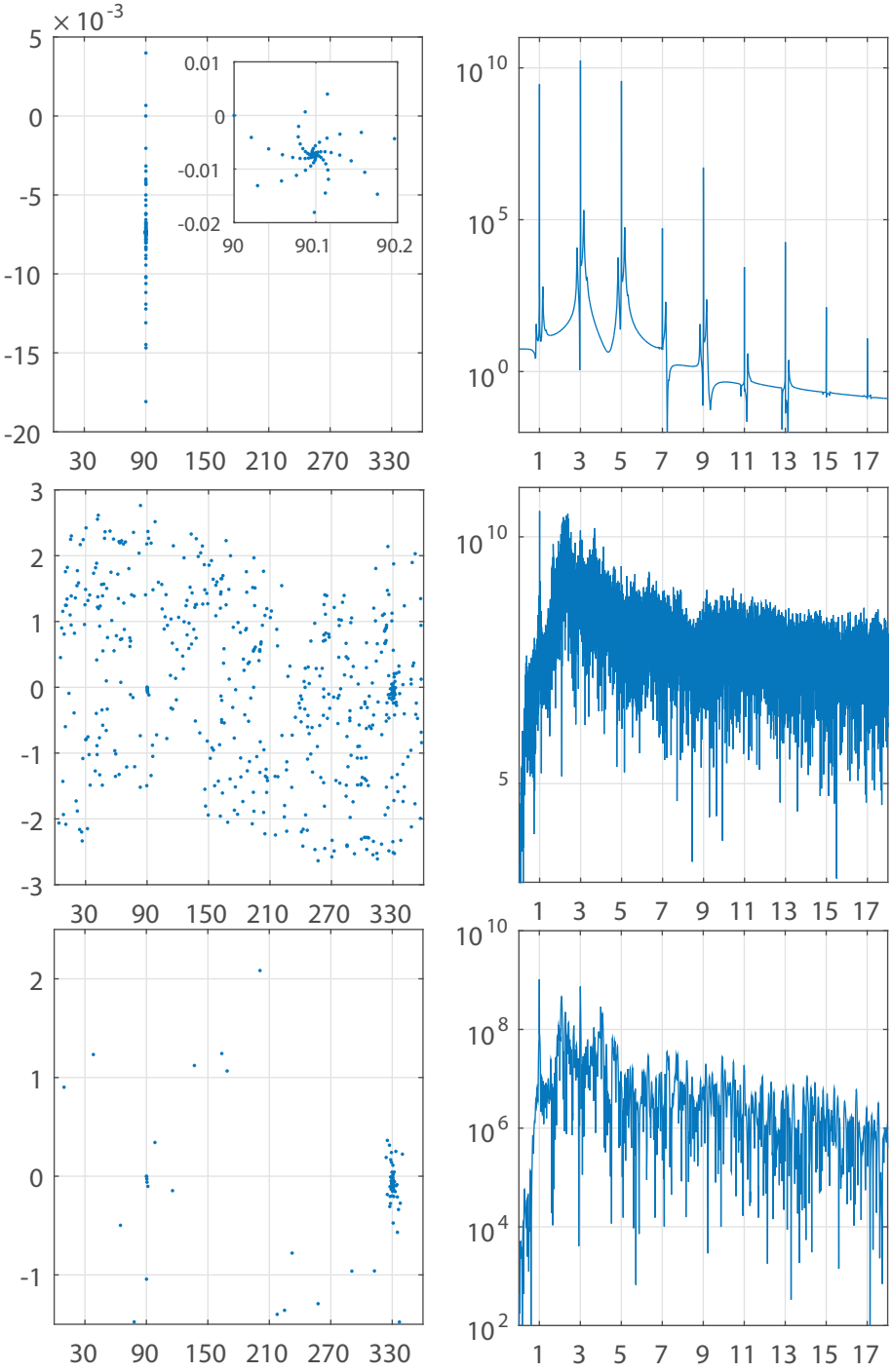

Figure 7.5: Left column: Poincaré section of the motion of the electron in a structured ring; abscissa ϕ (degrees); ordinate ℓ (diensionless). Right column: Fourier power spectrum of $\phi(\tau)$ (arb. un.) vs the harmonic order ω/ω_L. Always the electron starts at rest from $\phi_0 = 90°$. Top $v = 1.9771$, calculations carried out for 300 cycles; center $v = 1.9813$, calculations carried out for 600 cycles; bottom $v = 1.9855$, calculations carried out for 600 cycles. The values of the load parameters are $a = 5 \cdot 10^{-3}$, $u = 2.4348$.

7.4 Conclusion

The simulations indicate that plain and structured rings acted upon by a laser are good emitters of HHG and versatile tools for controlling the extension of the plateau and the polarization of the emitted harmonics both in classical and quantum domain [30, 41]. In fact, the particular symmetry of the system permits easy engineering of a suitable configuration of the laser pump fields which induces the ring to emit radiation with predesigned characteristics. We have seen that a classical charge, bound on a circle and driven by a laser, displays a variety show of comportment which can be obtained by small changes of the initial conditions and of the physical parameters characterizing the system such as the laser intensity. Surprisingly the classical spectra closely resemble the quantum ones with odd order harmonics and broad resonance lines that were also found in HHG from few level atoms.

In [38] it is shown that the wave function of one electron on a structured ring is described by Mathieu functions. These are non hypergeometric function showing oscillating stable as well as unstable solutions.

In the classical realm, the Mathieu equation occurs in the study of parametric oscillations that are induced by small non resonant excitation; the assortment of possible cases and connections is large and can only be mentioned here; we refer the interested reader to the book by Nayfeh and Mook [42]. The physical systems quickly slips toward chaotic behaviour. We consider as suggestive, however, that the wave function of a quantum ring is described by Mathieu functions which are underlying the physics of classical parametric excitations.

The relation between classical chaotic systems and their quantum equivalent is still obscure and is object of debate. We hope that a ring can unveil some of the secrets of the issue.

8 Momentum partition between constituents of exotic atoms during laser-induced tunneling ionization

This chapter is the result of the collaboration with the Professor Karen Z. Hatsagortsyan, whom I am very grateful, at the Max-Planck-Institut für Kernphysik, of Heidelberg in Germany. Now we present the article resulting from this collaboration (*D. Cricchio, E. Fiordilino and K. Z. Hatsagortsyan* Phys. Rev. A, 92:–, doi: 92.023408, 2015) in which we investigate the influence of the atomic core (ion) degree of freedom on the electron (muon) tunneling dynamics in the strong field of a circular polarized laser in the case of hydrogen, muonium, muonic hydrogen, and positronium atoms. In particular we study the impact of this effect on the photoelectron (-muon) momentum distribution and, respectively, on the partition of the photon momentum transfer between the electron (muon)and on the partition of the photon momentum between the electron (muon) and the atomic core (proton, antimuon, positron).

8.1 Introduction

In a strong laser field ionization of an atom takes place by absorption of multiple laser photons [43, 44, 45]. The photons carry momentum which is distributed among the ionized electron and the atomic core (ion) after the interaction. The photon momentum transfer in ionization is a nondipole effect, theoretically described by a first relativistic correction to the nonrelativistic Hamiltonian. In classical terms the momentum transfer to the electron along the laser propagation direction arises due to the magnetically induced Lorentz force. At rather strong laser fields the ionization is in the

tunneling regime, when the Keldysh parameter γ is small, and the electron is released from the atom by means of tunneling through the potential barrier formed by the laser suppressed atomic potential. In the tunneling regime the Lorentz force induces the momentum transfer to the electron along the laser propagation direction either when the electron moves in continuum after releasing from the atom, or during the tunneling step of the ionization. The first effect is characterized by the the relativistic field parameter $\xi \equiv eE_0/m_e c\omega$, where the E_0 and ω are the laser field amplitude and angular frequency, respectively, $-e$ and m_e are the electron charge and mass, respectively, and c is the speed of light. The momentum transfer along the laser propagation direction in continuum is $\Delta p_z \sim U_p/c$, where $U_p = m_e c^2 \xi^2/2$ is the electron ponderomotive energy in the laser field. It is responsible for shifting of the angular distribution of photoelectrons from the laser polarization direction into the propagation direction in relativistically strong laser fields when $\xi \sim 1$ [43, 46], for the suppression of the electron rescattering with the ion [47] and, consequently, suppression of nonsequential double ionization [48, 49] and high-order harmonic generation [50, 51].

The relativistic theory for the under-the-barrier dynamics demonstrated [52] that the magnetically induced Lorentz force brings about a momentum shift along the laser propagation direction also during the under-the-barrier motion. It has a characteristic value of I_p/c, which can be estimated from $\Delta p_z \sim e(v_a/c)B_0\tau_k \sim I_p/c$, with the atomic velocity $v_a = \sqrt{2I_p/m_e}$, the ionization potential I_p, the laser magnetic field $B_0 = E_0$, the Keldysh time $\tau_K = \gamma/\omega$, and the Keldysh parameter $\gamma = \sqrt{I_p/2U_p}$.

At nonrelativistic intensities the photon momentum transfer is rather small, nevertheless, it has been measured in a recent remarkable experiment [53], using nonrelativistic laser intensities of $2 - 10 \times 10^{14}$ W/cm^2 and detecting electron momenta of an order of 10^{-3} a.u.. The experimental results [53] in a circularly polarized laser field indicated that after tunneling ionization the ion carries a momentum I_p/c along the momentum of incoming photons, while the electron carries a momentum of U_p/c. This is in accordance with calculations of [54] and with the so-called simpleman model [55]. The latter assumes that the electron appears at the ionization tunnel exit with a vanishing momentum and then is driven solely by the laser field. The ion momentum

in this case follows from the momentum conservation law.

However, due to the Lorentz force effect during the under-the-barrier dynamics, the electron appears at the tunnel exit with a nonvanishing momentum along the laser propagation direction [52]. The latter contributes to the asymptotic electron momentum because of which the final ion momentum decreases with respect to the prediction of the simpleman model. Thus, the peak of the electron momentum distribution along the laser propagation direction is at $p_{ez} = I_p/3c$ (if the Coulomb field of the atomic core is neglected during the under-the-barrier motion), in contrast to the simpleman model vanishing prediction, and the ion should carry a momentum $p_{iz} = 2I_p/3c$ [56, 52]. Moreover, the ion momentum increases when the Coulomb field of the atomic core is accounted for in the near the over-the-barrier ionization regime, e.g., it is $p_{iz} = 0.8I_p/c$ at $E_0/E_a = 0.05$, see Fig. 6 in [57], where $E_a = (2I_p)^{3/2}$ is the atomic field strength. As it is noted in [56], these results are not inconsistent with the experiment of Ref. [53] because of the large experimental error. The experiment on the momentum partition at ionization is most clearly shown in a circularly polarized laser field because in this case the recollisions are avoided. In a linearly polarized field the Coulomb focusing because of recollisions modifies significantly the final momentum distribution [58] and complicates the analyses [59]. Recently, a numerical relativistic calculation of the electron momentum distribution in a linearly polarized laser field [60] indicated that the momentum shift in the laser propagation direction depends linearly on the laser intensity, which is in accordance with the experiment [53].

If the atomic degree of freedom is neglected during tunneling ionization of the electron, the momentum transfer to the ion can be simply deduced via the momentum conservation law, taking into account the electron momentum after the ionization. In treating the electron dynamics in strong field ionization, usually, the ion is assumed to be not moving. While it is a good approximation for the ionization of hydrogen and other common atoms because of smallness of the mass ratio of the electron to the ion, it is not the case for exotic atoms such as muonium [the bound state of an electron and antimuon, the mass ratio of an electron to muon is $m_e/m_\mu \approx 1/207$], muonic hydrogen [the bound state of a muon and a proton, the mass ratio of a muon to proton

is $m_\mu/m_p \approx 0.1126$] and positronium [the bound state of the electron and positron, the mass ratio of an electron to a positron is $m_{e-}/m_{e+} = 1$]. The hydrogen ionization problem taking into account the ion degree of freedom first was considered in [56] for derivation of the ion momentum, however, neglecting its impact on the electron momentum distribution.

Note that the influence of the nuclear degrees of freedom on the electronic dynamics is well known in strong field molecular processes as, so-called, non-Born-Oppenheimer dynamics, see e.g. [61, 62, 63].

In this chapter we investigate the influence of the atomic core (ion) degree of freedom on the electron (muon) tunneling dynamics in a strong laser field of a circular polarization in the case of hydrogen, muonium, muonic hydrogen, and positronium atoms. The impact of this effect on the photo-electron (-muon) momentum distribution and, respectively, on the partition of the photon momentum transfer between the electron (muon) and the atomic core (proton, antimuon, positron) are studied.

We label by "electron" the negative component of the exotic atom, which is the electron in the case of muonium and positronium, and muon in the case of muonic hydrogen. The label "ion" is employed for the positive component of the exotic atom, which is the proton in the case of muonic hydrogen, antimuon in the case of muonium, and the positron in the case of positronium.

The structure of the paper is the following. In Sec. 8.2 the momentum partition is analysed using the simpleman model along with the energy-momentum conservation law. In Sec. 8.3 the result of the strong field approximation (SFA) is presented, which is followed by the discussion in Sec. 8.4 and the conclusion in Sec. 8.5.

8.2 The simpleman model and the energy-momentum conservation

In this section we derive the momentum partition between the electron and ion during tunneling ionization, assuming that the photoelectron dynamics follows the simpleman

model [55]. The information provided by energy and momentum conservation laws is used to deduce the ion momentum $\vec{p}_i$ and the number of absorbed laser photons n corresponding to a certain photoelectron momentum $\vec{p}_e$ in the tunneling ionization process.

According to the simpleman model, the electron appears in continuum with a vanishing momentum in the most probable trajectory and afterwards is driven by the laser field, absorbing n laser photons. The energy conservation for the ionization process reads:

$$(\varepsilon_e - m_e c^2) + (\varepsilon_i - m_i c^2) = n\omega - I_p, \tag{8.1}$$

where $\varepsilon_{e,i} = c\sqrt{\vec{p}_{e,i}^{\,2} + m_{e,i}^2 c^2}$ and $m_{e,i}$ are the energy and mass of the electron and the ion, respectively. The momentum conservation provides

$$\vec{p}_{e\perp} + \vec{p}_{i\perp} = 0 \tag{8.2}$$

$$p_{e\,z} + p_{i\,z} = \frac{n\omega}{c}, \tag{8.3}$$

where $p_{e,i\,z}$ and $\vec{p}_{e,i\perp}$ are the electron and the ion momentum components along the laser propagation direction z and the transverse direction, respectively. Combining Eqs. (8.1) and (8.3) we derive

$$(\varepsilon_e - cp_{e\,z} - m_e c^2) + (\varepsilon_i - cp_{i\,z} - m_i c^2) = -I_p. \tag{8.4}$$

In the case of a common atom ($m_i \gg m_e$) the kinetic energy of the ion is small and can be neglected, $\varepsilon_i - m_i c^2 \approx 0$. In the plane laser field

$$\Lambda \equiv \varepsilon - cp_z \tag{8.5}$$

is an integral of motion [47]. In the simpleman model $\Lambda_e = m_e c^2$ for the electron because of vanishing of the electron kinetic momentum at the tunnel exit. Consequently, the ion momentum is derived

$$p_{iz} = \frac{I_p}{c}. \tag{8.6}$$

In the simpleman model the electron transverse kinetic momentum in continuum is derived from the conservation of the transverse canonical momentum $\vec{p}_{e\perp} - e\vec{A}(\phi) =$

const. Taking into account that at the ionization moment ϕ_0 the electron kinetic momentum is vanishing, we have

$$\vec{p}_{e\perp} = -e\left[\vec{A}(\phi_0) - \vec{A}(\phi)\right], \tag{8.7}$$

where $\phi = \omega(t - z/c)$ is the laser phase. The electron longitudinal momentum is derived from the conservation law

$$\Lambda_{e,i} + cp_{e,i\,z} = c\sqrt{p_{e,i}^2 + m_{e,i}^2c^2}, \tag{8.8}$$

which yields

$$p_{e,i\,z} = \frac{c^2p_\perp^2 + m_{e,i}^2c^4 - \Lambda_{e,i}^2}{2c\Lambda_{e,i}}. \tag{8.9}$$

Assuming a vanishing transverse momentum at the tunnel exit ($\Lambda_e = m_ec^2$) yields

$$p_{e\,z} = \frac{e^2}{2m_e}\left[\vec{A}(\phi_0) - \vec{A}(\phi)\right]^2. \tag{8.10}$$

At switching off the laser field $\vec{A}(\phi) \to 0$:

$$\vec{p}_{e\perp} = -e\vec{A}(\phi_0), \tag{8.11}$$

$$p_{e\,z} = \frac{U_p}{c}, \tag{8.12}$$

$$\varepsilon_e = m_ec^2 + U_p\,, \tag{8.13}$$

where $U_p = e^2\vec{A}^2(\phi_0)/(2m_e) = m_ec^2\xi^2/2$. Therefore, according to the simpleman model, Eqs. (8.3), (8.6) and (8.12), from the totally absorbed photon momentum during ionization

$$\frac{n\omega}{c} = \frac{I_p}{c} + \frac{U_p}{c} \tag{8.14}$$

the ion absorbs the momentum $p_{iz} = I_p/c$ and the rest of the photon momentum U_p/c is transferred to the electron.

The experiment of Ref. [53] is in accordance with the above mentioned results of the simpleman model. However, the ion dynamics during the tunneling and the relativistic features of the electron under-the-barrier dynamics [56, 52, 57] have impact

on the momentum partition in strong field ionization which will be discussed in the next sections. Here we shortly mention that when going beyond the simpleman model, the Lorentz force during the under-the-barrier motion induces a nonvanishing momentum component for the electron, $p_{ez}^{(0)}$, along the laser propagation direction at the tunnel exit. Then, $\Lambda_e \approx m_e c^2 - c p_{ez}^{(0)}$, when $p_{ez}^{(0)} \ll m_e c$ as usually is the case, and from Eq. (8.4) one derives

$$p_{iz} = I_p/c - p_{ez}^{(0)} \,. \tag{8.15}$$

In the case of exotic atoms, when the constituents masses are of the same order, the simpleman condition for the vanishing momentum at the tunnel exit concerns the relative momentum

$$M\vec{p}^{(0)} = m_i \vec{p}_e^{(0)} - m_e \vec{p}_i^{(0)} = 0 \,, \tag{8.16}$$

see Table I. Then, $\vec{p}_{e\perp}^{(0)} = \vec{p}_{i\perp}^{(0)} = 0$, because of Eq. (8.2). Moreover, taking into account that $p_{i\,z}^{(0)} = (m_i/m_e) p_{e\,z}^{(0)}$, one has

$$\Lambda_i - m_i c^2 = \frac{m_i}{m_e}(\Lambda_e - m_e c^2), \tag{8.17}$$

and from Eq. (8.4) one derives

$$\Lambda_e = m_e c^2 \left(1 - \frac{I_p}{Mc^2}\right), \tag{8.18}$$

$$\Lambda_i = m_i c^2 \left(1 - \frac{I_p}{Mc^2}\right), \tag{8.19}$$

where $M = m_e + m_i$. The electron and ion momenta can be calculated from Eqs. (8.9) and (8.11), which finally leads to the following expressions in the leading order of $I_p/(Mc^2)$:

$$\vec{p}_{e\perp} = -e\vec{A}(\phi_0) \,, \tag{8.20}$$

$$p_{e\,z} \approx m_e c \left[\frac{\xi^2}{2}\left(1 + \frac{I_p}{Mc^2}\right) + \frac{I_p}{Mc^2}\right] , \tag{8.21}$$

$$\vec{p}_{i\perp} = e\vec{A}(\phi_0) \,, \tag{8.22}$$

$$p_{i\,z} \approx m_i c \left[\frac{\xi^2}{2}\frac{m_e^2}{m_i^2}\left(1 + \frac{I_p}{Mc^2}\right) + \frac{I_p}{Mc^2}\right] . \tag{8.23}$$

This general expression for the final electron and ion momenta according to the simpleman model includes the limiting cases of the infinitely heavy ionic core [$m_i \to \infty$, see Eqs. (8.6), (8.11) and (8.12)] and of the positronium atom [$m_e = m_i$]. In the latter case there is symmetry between the electron and positron dynamics stemming from a positronium atom

$$p_{e\,z} = p_{i\,z} \approx \frac{m_e c \xi^2}{2}\left(1 + \frac{I_p}{2m_e c^2}\right) + \frac{I_p}{2c}\,. \tag{8.24}$$

where p_{iz} denotes the positron momentum.

Thus, the simpleman model along with the energy-momentum conservation provides information on momentum partition between the electron and ion in the tunneling ionization process, given by Eqs. (8.20)-(8.23). We underline that the simpleman model does not take into account the initial momentum of the electron at the tunnel exit, which can arise due to the Lorentz force [52] and due to nonadiabatic dynamics (in the intermediate regime between the tunneling and mutiphoton regimes) [64]. Moreover, the Lorentz force effect depends on the ionic recoil inducing corrections of the order of m_e/m_i. Note also that the final momentum distribution is disturbed also by the Coulomb focusing during the electron motion in the continuum [58].

In the next sections the Lorentz force effect and the impact of the ion recoil for the momentum partitioning between the ion and the electron are discussed.

8.3 Strong field approximation

We consider strong field ionization of a simple atomic system consisting of a positively and a negatively charged particles (labelled as "ion" and "electron", respectively) which are initially in the ground state of the bound system. The main aim is to study the influence of the ion motion on the electron tunneling dynamics and its impact on the momentum partitioning between the ionized electron and the atomic core in tunnelling ionization. The theory will be applied for the cases of ionization of hydrogen, muonium, muonic hydrogen, and for positronium. The degree of freedom both of the ion and the electron will be taken into account. The effect of the magnetically induced

Lorentz force on the ionization dynamics is included by means of nondipole treatment of the laser field in the weakly relativistic regime.

The Hamiltonian of the system under the consideration, consisting of an ion and an electron in a laser field reads:

$$\begin{aligned} \mathcal{H} &= \frac{1}{2m_i}\left[-i\vec{\nabla}_i - q_i\vec{A}\left(t-\frac{z_i}{c}\right)\right]^2 \\ &+ \frac{1}{2m_e}\left[-i\vec{\nabla}_e - q_e\vec{A}\left(t-\frac{z_e}{c}\right)\right]^2 + \frac{q_iq_e}{\mid \vec{r}_e - \vec{r}_i \mid}, \end{aligned} \tag{8.25}$$

where $\vec{r}_{e,i}$, $q_i = 1$ and $q_e = -1$ are the radius-vectors and charges of the ion and the electron, respectively (henceforth atomic units are used). To simplify the calculations it is convenient to write the Hamiltonian in the relative and the center-of-mass (c.m.) coordinates:

$$\begin{aligned} \mathcal{H} &= \frac{1}{2m_i}\left[-i\frac{m_i}{M}\vec{\nabla}_R + i\vec{\nabla}_r - q_i\vec{A}\left(\tau+\frac{m_e}{M}\frac{z}{c}\right)\right]^2 \\ &+ \frac{1}{2m_e}\left[-i\frac{m_e}{M}\vec{\nabla}_R - i\vec{\nabla}_r - q_e\vec{A}\left(\tau-\frac{m_i}{M}\frac{z}{c}\right)\right]^2 + \frac{q_iq_e}{r} \end{aligned} \tag{8.26}$$

The variable transformation is shown in Table I. We use nondipole description in order to study the dynamic of the system under the influence of the magnetic component of the laser field which is responsible for the momentum transfer from the photons to the electron and the ion. The circularly polarized laser field propagating in z-direction is

$\vec{R} = (X,Y,Z) = \frac{m_i\vec{r}_i + m_e\vec{r}_e}{m_i+m_e}$	$\vec{r}_i = \vec{R} - \frac{m_e}{M}\vec{r}$	$t - \frac{z_i}{c} = \tau + \frac{m_e}{Mc}z$
$\vec{r} = (x,y,z) = \vec{r}_e - \vec{r}_i$	$\vec{r}_e = \vec{R} + \frac{m_i}{M}\vec{r}$	$t - \frac{z_e}{c} = \tau - \frac{m_i}{Mc}z$
$\mu = \frac{m_im_e}{m_i+m_e}$	$\vec{\nabla}_i = \frac{m_i}{M}\vec{\nabla}_R - \vec{\nabla}_r$	$\tau = t - \frac{Z}{c}$
$M = m_i + m_e$	$\vec{\nabla}_e = \frac{m_e}{M}\vec{\nabla}_R + \vec{\nabla}_r$	$\zeta = Z$
$\eta \equiv \frac{m_i^2 - m_e^2}{m_im_e}$	$\vec{P} = \vec{p}_e + \vec{p}_i$	$\frac{\partial}{\partial Z} = \frac{\partial}{\partial\zeta} - \frac{\partial}{c\partial\tau}$
$\hat{\vec{P}} = -i\vec{\nabla}_R, \hat{\vec{p}} = -i\vec{\nabla}, \dot{\vec{p}} = \mu\dot{\vec{r}}$	$\vec{p} = \frac{m_i\vec{p}_e - m_e\vec{p}_i}{M}$	$\frac{\partial}{\partial t} = \frac{\partial}{\partial\tau}$

Table 8.1: The variable transformation to the relative and c.m. coordinates and, further, to the light-time.

described by a vector potential:

$$\begin{aligned} A_x(z_\alpha, t) &= A_0 \cos\omega(t - z_\alpha/c) \\ A_y(z_\alpha, t) &= A_0 \sin\omega(t - z_\alpha/c) \end{aligned} \tag{8.27}$$

with $A_0 = E_0/\omega$ and $\alpha \in \{i, e\}$.

The ionization transition amplitude is calculated using SFA [65, 66, 67]:

$$M_{fi} = -i\int_{-\infty}^{\infty} \vec{dt}\, \langle \Psi_{\vec{P},\vec{p}}(t) \mid V_L(t) \mid \Psi_{0,\vec{P}_0}(t)\rangle \tag{8.28}$$

where

$$V_L(t) \equiv \sum_\alpha \left[-\frac{q_\alpha}{m_e}\vec{p}_\alpha \vec{A}(z_\alpha, t) + \frac{q_\alpha^2 \vec{A}^2(z_\alpha, t)}{2m_\alpha} \right]$$

describes the interaction with the laser field; $|\Psi_{0,\vec{P}_0}(t)\rangle = |\Phi_0\rangle e^{iI_p t + i\vec{P}_0\vec{R}}$ is the initial bound state of the electron-ion system which is in the ground state $|\Phi_0\rangle$ with the energy $-I_p$; the momentum of c.m. of the electron-ion system is $\vec{P}_0$; $|\Psi_{\vec{P},\vec{p}}(t)\rangle$ is the continuum state of the electron and ion in the laser field with the asymptotic c.m. momentum $\vec{P}$ and the relative momentum $\vec{p}$, neglecting Coulomb interaction.

Similar to [43], the transition matrix element of Eq. (8.28) can be represented as

$$M_{fi} = -i\int_{-\infty}^{\infty} \vec{dt}\, \langle \Psi_{\vec{P},\vec{p}}(t) \mid V(\vec{r}) \mid \Psi_{0,\vec{P}_0}(t)\rangle, \tag{8.29}$$

where $V(\vec{r}) = q_i q_e/r$ is the atomic potential.

The continuum wave function for the electron and ion system in the laser field, after transformation to the light-time $\tau = t - Z/c$, where Z is the c.m. coordinate along the laser propagation direction, fulfils the equation

$$i\partial_\tau \Psi_{\vec{P},\vec{p}}(\tau) = \hat{H}\Psi_{\vec{P},\vec{p}}(\tau)\,, \tag{8.30}$$

with

$$\begin{aligned} \hat{H} = \frac{1}{2m_i}\left[-i\frac{m_i}{M}\left(\vec{\nabla}_R - \frac{\hat{\vec{z}}}{c}\partial_\tau\right) + i\vec{\nabla} - q_i\vec{A}\left(\tau + \frac{m_e}{M}\frac{z}{c}\right)\right]^2 \\ + \frac{1}{2m_e}\left[-i\frac{m_e}{M}\left(\vec{\nabla}_R - \frac{\hat{\vec{z}}}{c}\partial_\tau\right) - i\vec{\nabla} - q_e\vec{A}\left(\tau - \frac{m_i}{M}\frac{z}{c}\right)\right]^2. \end{aligned}$$

Taking into account the conservation law $[\hat{\vec{P}}, \hat{H}] = 0$, the c.m. coordinates are factorized in the wave function:

$$\Psi_{\vec{P},\vec{p}}(\tau, \vec{r}, \vec{R}) = \exp\left(i\vec{P}\cdot\vec{R} - i\mathcal{E}t\right)\phi(\vec{r}, \tau), \tag{8.31}$$

with the c.m. energy $\mathcal{E}$ and momentum $\vec{P}$, after the interaction is switched off.

In the weakly-relativistic regime the vector potential can be expanded to the first order in $1/c$:

$$\vec{\vec{A}}\left(\tau \pm \frac{m_\alpha z}{Mc}\right) \approx \vec{A}(\tau) \mp \frac{m_\alpha z}{Mc}\vec{E}(\tau). \tag{8.32}$$

Then, neglecting the high-order terms over $1/c$ in Eq. (8.30), we arrive at the following equation:

$$\begin{aligned} & \left\{ i\left(1 - \frac{P_z}{Mc}\right)\partial_\tau - \frac{1}{2\mu}\left[-i\vec{\nabla} + \vec{A}(\tau)\right]^2 \right. \\ + \quad & \frac{z}{m_e c}\left[-i\vec{\nabla} + \vec{A}(\tau)\right]\vec{A}'(\tau)\left(1 - \frac{m_e}{m_i}\right) \\ - \quad & \left. \frac{P^2}{2M} + \frac{z}{Mc}\vec{P}\cdot\vec{A}'(\tau) + \mathcal{E}\right\}\phi(\vec{r}, \tau) = 0\,. \end{aligned} \tag{8.33}$$

When the wave function is parametrized as

$$\phi(\vec{r}, \tau) = \exp[i\vec{p}\cdot\vec{r} + iT(\tau)z - iS(\tau)]\,, \tag{8.34}$$

one obtains

$$T(\tau) = \frac{\eta}{Mc\left(1 - \frac{P_z}{Mc}\right)}\int_{-\infty}^{\tau} d\tau' \left[\vec{p} + \vec{A}(\tau')\right]\vec{A}'(\tau')\,, \tag{8.35}$$

$$S(\tau) = \frac{1}{2\mu\left(1 - \frac{P_z}{Mc}\right)}\int_{-\infty}^{\tau} d\tau' \left[\vec{p} + \hat{\vec{z}}T(\tau') + \vec{A}(\tau')\right]^2\,, \tag{8.36}$$

where μ and η are defined in Table I. Finally, the continuum wave function for the electron-ion system in the laser field in the leading order of the $1/c$-expansion is

$$\Psi_{\vec{P},\vec{p}}(\tau, \vec{r}, \vec{R}) = \mathcal{N}\exp\left(i\mathcal{S}\right)\,, \tag{8.37}$$

with the normalization constant $\mathcal{N}$ and the action

$$\mathcal{S} = \vec{P}\cdot\vec{R} - \mathcal{E}t + \vec{p}\cdot\vec{r} + \frac{\eta\, z}{Mc}\left[\vec{p}\cdot\vec{A}(\tau) + \frac{\vec{A}^2(\tau)}{2}\right]$$

$$- \quad \frac{1}{\mu}\left(1+\frac{P_z+\eta p_z}{Mc}\right)\int_{-\infty}^{\tau} d\tau' \left[\vec{p}\cdot\vec{A}(\tau')+\frac{\vec{A}^2(\tau')}{2}\right]. \tag{8.38}$$

We calculate the matrix elements of the amplitude between the ground state and the continuum as:

$$M_{fi} \;=\; -i\mathcal{N}\int d\vec{t}\int d\vec{R}\int d\vec{r}\, e^{-i\mathcal{S}}V(r)\Phi_0(r)e^{iI_p t}, \tag{8.39}$$

assuming that the atom is at rest in the initial state $\vec{P}_0 = 0$.

Let us first consider the momentum sharing between the electron and the ion in the simplest and transparent case when the atomic potential is modelled by a short-range potential. Later we will discuss the correction to this picture due to the real atomic potential. In the case of short-range potential

$$V(r) = (2\pi/\kappa)\delta(\vec{r})\partial_r r, \tag{8.40}$$

one has $\langle\vec{p}|V|\Phi_0\rangle = -\sqrt{\kappa}/(2\pi)$, with $\kappa \equiv \sqrt{2\mu I_p}$. We expand the last term of the action in Eq. (8.38):

$$\begin{aligned}
&\exp\left\{-\frac{i}{\mu}\left(1+\frac{P_z+\eta p_z}{Mc}\right)\int_{-\infty}^{\tau}\left(\vec{p}\cdot\vec{A}(\tau')+\frac{A^2}{2}\right)\vec{d\tau}'\right\} \\
&= \sum_{n=-\infty}^{\infty} i^n J_n(\zeta)\exp\left\{in\omega\tau + i\sigma_0\tau + in\varphi_0\right\},
\end{aligned} \tag{8.41}$$

where $J_n(\zeta)$ is the Bessel functions, n is the number of absorbed photons, $\tan\varphi_0 = p_x/p_y$, and

$$\zeta \;=\; \left(1+\frac{P_z+\eta p_z}{Mc}\right)\frac{p_\perp A_0}{\mu\omega}, \tag{8.42}$$

$$\sigma_0 \;=\; \left(1+\frac{P_z+\eta p_z}{Mc}\right)\frac{A_0^2}{2\mu}, \tag{8.43}$$

and obtain for the transition amplitude

$$\begin{aligned}
M_{fi} \;&=\; i(2\pi)^3\mathcal{N}\sqrt{\kappa}\,\delta\left(\vec{P}_\perp\right)\sum_{n=-\infty}^{\infty}\delta\left(P_Z+\frac{\sigma_0}{c}-\frac{n\omega}{c}\right) \\
&\times\; \delta\left(\frac{P_Z^2}{2M}+\frac{p^2}{2\mu}+I_p+\sigma_0-n\omega\right)J_n\left(\zeta\right)e^{in\varphi_0}
\end{aligned} \tag{8.44}$$

Then we can calculate the ionization rate

$$dW = |M_{fi}|^2\frac{d^3\vec{P}}{(2\pi)^3}\frac{d^3\vec{p}}{(2\pi)^3} = |M_{fi}|^2\frac{d^3\vec{p}_i}{(2\pi)^3}\frac{d^3\vec{p}_e}{(2\pi)^3}. \tag{8.45}$$

Describing the final phase space via the electron and ion momenta, the ionization rate reads

$$\begin{aligned}\frac{dW}{d^3\vec{p}_i d^3\vec{p}_e} &= \frac{\kappa}{(2\pi)^4}\sum_n \delta\left(\vec{p}_{e\perp}+\vec{p}_{i\perp}\right)\delta\left(p_{ez}+p_{iz}-\frac{n\omega-\sigma_0}{c}\right)\\ &\times\ \delta\left(\Delta\right)\, J_n^2(\zeta)\,,\end{aligned} \tag{8.46}$$

where

$$\begin{aligned}\Delta &\equiv I_p - n\omega + \sigma_0 + \frac{p_e^2}{2m_e}+\frac{p_i^2}{2m_i}\,,\\ \sigma_0 &= \frac{m_e^2c^2\xi^2}{2\mu}\left[1+\frac{p_{ez}+p_{iz}}{Mc}+\frac{\eta}{Mc}\left(\frac{m_i}{M}p_{ez}-\frac{m_e}{M}p_{iz}\right)\right]\,,\\ \zeta &= \frac{m_e c\xi p_{e\perp}}{\mu\omega}\left[1+\frac{p_{ez}+p_{iz}}{Mc}+\frac{\eta}{Mc}\left(\frac{m_i}{M}p_{ez}-\frac{m_e}{M}p_{iz}\right)\right]\,.\end{aligned}$$

After the integration over the ion momenta, one obtains for the photoelectron momentum distribution

$$\frac{dW}{d^3\vec{p}_e} = \frac{\kappa}{(2\pi)^4}\frac{1}{1+\frac{\xi^2}{2}\frac{m_e^2}{m_i^2}}\sum_n J_n^2(\zeta)\delta\left(\Delta\right)\,. \tag{8.47}$$

Here we take into account that

$$\left|\frac{\partial}{\partial p_{iz}}p_{ez}+p_{iz}\frac{n\omega-\sigma_0}{c}\right| = 1+\frac{\xi^2}{2}\frac{m_e^2}{m_i^2}.$$

Expressing the ion momentum via the electron momentum using the momentum conservation δ-function, we have

$$\zeta = \frac{m_e c\xi p_{e\perp}}{\mu\omega}\left[1+\left(1-\frac{m_e}{m_i}\right)\frac{p_{ez}}{m_e c}+\frac{m_e^2}{Mm_i}\nu\right]\,, \tag{8.48}$$

$$\nu = \frac{1}{1+\frac{\xi^2}{2}\frac{m_e^2}{m_i^2}}\left\{\frac{n\omega}{m_e c^2}-\frac{\xi^2}{2}\frac{m_e}{\mu}\left[1+\left(1-\frac{m_e}{m_i}\right)\frac{p_{ez}}{m_e c}\right]\right\}\,, \tag{8.49}$$

$$\Delta = m_e c^2\left\{\tilde{I}_p+\frac{p_e^2}{2\mu m_e c^2}-\nu\left(1+\frac{p_{ez}}{m_i c}\right)+\frac{\nu^2}{2}\frac{m_e}{m_i}\right\}\,, \tag{8.50}$$

where $\tilde{I}_p \equiv I_p/m_e c^2$ and $\nu \equiv (n\omega-\sigma_0)/m_e c^2$.

The ionization rate given by Eq. (8.47) depends on ion mass and takes into account the impact of the motion of the c.m. of the electron-ion system on the tunneling dynamics. For the hydrogen atom it is negligible as it scales with the small ratio $m_e/m_i \approx 1/1836$. However, for exotic atoms this effect cannot be neglected.

8.4 Discussion

Let us analyse the ionization differential rate to find out the most probable momentum of the ionized electron and ion in the case of different atomic systems. We can approximately replace the summation over the photon number n in Eq. (8.47) by integration and carry out the latter using the δ-function:

$$\frac{dW}{d^3\vec{p}_e} \approx \frac{\kappa}{(2\pi)^4} \frac{J_n^2(\zeta)}{\omega\left(1+\dfrac{p_{ez}}{m_i c}-\dfrac{m_e}{m_i}\nu\right)}\,, \tag{8.51}$$

where we have used that

$$\frac{\partial\Delta}{\partial n} = \frac{\omega}{1+\frac{\xi^2}{2}\frac{m_e^2}{m_i^2}}\left(1+\frac{p_{ez}}{m_i c}-\frac{m_e}{m_i}\nu\right)\,. \tag{8.52}$$

Here, the number of absorbed photons, or the parameter ν, is determined from the energy conservation $\Delta = 0$, whose approximate solution reads

$$\nu \approx \frac{\tilde{I}_p + \dfrac{p_e^2}{2\mu m_e c^2}}{1+\dfrac{p_{ez}}{m_i c}}\,, \tag{8.53}$$

where we have used that $\tilde{I}_p \ll 1$ and $p_e^2 \ll \mu m_e c^2$. Accordingly, the number of absorbed laser photons is

$$n \;=\; \frac{m_e c^2}{\omega}\left\{\nu\left(1+\frac{\xi^2}{2}\frac{m_e^2}{m_i^2}\right)+\frac{\xi^2 M}{2m_i}\left[1+\left(1-\frac{m_e}{m_i}\right)\frac{p_{ez}}{m_e c}\right]\right\}\,, \tag{8.54}$$

The qualitative behaviour of the momentum distribution according to the differential ionization rate of Eq. (8.51) is determined by the Bessel function. In the tunneling regime, when $U_p/\omega \gg 1$ and $I_p \gg 1$, one has $\zeta \gg 1$, therefore, for the further analysis we will use the asymptotics of the Bessel function $n \sim \zeta \to \infty$ [68]:

$$J_n^2(\zeta) \sim \frac{1}{2\pi\sqrt{2(n-\zeta)\zeta}} \exp\left\{-\frac{4\sqrt{2}}{3}\frac{(n-\zeta)^{3/2}}{\zeta^{1/2}}\right\}\,. \tag{8.55}$$

The peak of the momentum distribution corresponds to the minimum of the expression $\mathcal{F} \equiv (n-\zeta)^3/\zeta$, achievable at $n \sim \zeta$, where n and ζ are given by Eqs. (8.54) and (8.48).

8.4.1 Hydrogen atom

First, let us consider the simplest limit of infinitely heavy ion $m_i \to \infty$. In this case,

$$\nu = \frac{\varkappa^2}{2} + \frac{p_\perp^2}{2} + \frac{p_z^2}{2}, \tag{8.56}$$

$$\zeta = \frac{m_e c^2}{\omega} \xi p_\perp (1 + p_z), \tag{8.57}$$

$$n = \frac{m_e c^2}{\omega} \left[\nu + \frac{\xi^2 (1 + p_z)}{2} \right], \tag{8.58}$$

with $\varkappa^2/2 \equiv \tilde{I}_p$, $p_\perp \equiv p_{e\perp}/m_e c$ and $p_z \equiv p_{e\,z}/m_e c$, which yields

$$\mathcal{F}(p_\perp, p_z) = \left(\frac{m_e c^2}{\omega} \right)^2 \frac{\left[\varkappa^2 + p_\perp^2 + p_z^2 + (\xi^2 - 2p_\perp \xi)(1 + p_z) \right]^3}{8 \xi p_\perp (1 + p_z)}. \tag{8.59}$$

The conditions for $\mathcal{F} = \min$, $\partial \mathcal{F}/\partial p_\perp = 0$ and $\partial \mathcal{F}/\partial p_z = 0$, read, respectively:

$$\begin{aligned} &6 \left[p_\perp - \xi (1 + p_z) \right] p_\perp = \varkappa^2 + p_\perp^2 + p_z^2 + (\xi^2 - 2p_\perp \xi)(1 + p_z), \\ &3(1 + p_z) \left[2p_z + \xi^2 - 2p_\perp \xi \right] = \\ &\qquad = \varkappa^2 + p_\perp^2 + p_z^2 + (\xi^2 - 2p_\perp \xi)(1 + p_z). \end{aligned} \tag{8.60}$$

Solving the latter in perturbation with respect to ξ and taking into account that $p_\perp \sim \xi$ and $p_z \sim \xi^2$, as well as $\varkappa \sim \xi$, we obtain:

$$p_{e\perp} = m_e c \xi \left(1 + \frac{\gamma^2}{6} \right), \tag{8.61}$$

$$p_{e\,z} = \frac{I_p}{3c} + \frac{p_{e\perp}^2}{2 m_e c}. \tag{8.62}$$

In the latter the leading order terms with respect to γ are retained ($\gamma = \varkappa/\xi < 1$ in the tunnelling regime). The ion momentum can be deduced from the δ-functions of Eq. (8.46),

$$p_{i\,z} = \nu m_e c^2 - p_{e\,z}, \tag{8.63}$$

$$p_{i\perp} = -p_{e\perp}. \tag{8.64}$$

and using Eqs. (8.49),(8.61), and (8.62):

$$p_{i\,z} = \frac{2 I_p}{3c}. \tag{8.65}$$

Comparing Eq. (8.65) with our qualitative discussion in Sec. II, see Eq. (8.15), we can conclude that the electron momentum at the tunnel exit is $p_z^{(0)} = I_p/3c$, which is the reason of variation the ion momentum from the I_p/c value. This result coincides with the predictions of Refs. [56, 52].

8.4.2 Exotic atoms

In the case of exotic atoms, such as positronium ($m_e/m_i = 1$), muonic hydrogen atom ($m_e/m_i \approx 0.1126$), and muonium ($m_e/m_i \approx 1/207$), the masses of constituents are comparable and, therefore we have to use the general expressions for the parameters n and ζ, given by Eqs. (8.48),(8.49), and (8.54).

First, we find an approximate solution of Eq. (8.49) in perturbation with respect to the parameter ξ:

$$\nu \approx \nu^{(2)} + \nu^{(4)}\,, \tag{8.66}$$

where $\nu^{(n)} \sim \xi^n$, assuming that $p_\perp \sim \xi$ and $p_z \sim \xi^2$.

$$\nu^{(2)} = \frac{p_\perp^2}{2}(1+\tilde{\mu}) + \frac{\varkappa^2}{2}, \tag{8.67}$$

$$\nu^{(4)} = \frac{p_z^2}{2}(1+\tilde{\mu}) - \nu^{(2)}\tilde{\mu}p_z + \frac{{\nu^{(2)}}^2}{2}\tilde{\mu}\,, \tag{8.68}$$

where $\tilde{\mu} \equiv m_e/m_i$. The parameters of the Bessel functions up to the order of ξ^4 are:

$$\zeta \approx \frac{m_e c^2}{\omega}(1+\tilde{\mu})\xi p_\perp \left[1 + (1-\tilde{\mu})p_z + \frac{\tilde{\mu}^2}{1+\tilde{\mu}}\nu^{(2)}\right], \tag{8.69}$$

$$n \approx \frac{m_e c^2}{\omega}\left\{\nu^{(2)}\left(1 + \frac{\xi^2\tilde{\mu}^2}{2}\right) + \nu^{(4)} + \frac{\xi^2}{2}\left[1 + \tilde{\mu} + (1-\tilde{\mu}^2)p_z\right]\right\}. \tag{8.70}$$

The condition $\partial\mathcal{F}/\partial p_\perp = 0$ in this case yields:

$$3p_\perp(1+\tilde{\mu})\left[1 + (1-\tilde{\mu})p_z + \frac{\tilde{\mu}^2}{1+\tilde{\mu}}\nu^{(2)}\right]\left\{(1+\xi^2\tilde{\mu}^2)p_\perp + \tilde{\mu}p_\perp(\nu^{(2)} - p_z) - \xi\left[1 + (1-\tilde{\mu})p_z + \frac{\tilde{\mu}^2}{1+\tilde{\mu}}\nu^{(2)} + p_\perp^2\tilde{\mu}^2\right]\right\}$$

$$= \left\{ \nu^{(2)} \left(1 + \frac{\xi^2 \tilde{\mu}^2}{2} \right) + \nu^{(4)} + (1+\tilde{\mu}) \left[1 + (1-\tilde{\mu}) p_z \right] \frac{\xi^2}{2} \right.$$
$$\left. - (1+\tilde{\mu}) \xi p_\perp \left[1 + \tilde{\mu} + (1-\tilde{\mu}) p_z + \frac{\tilde{\mu}^2}{1+\tilde{\mu}} \nu^{(2)} \right] \right\}$$
$$\times \left[1 + (1-\tilde{\mu}) p_z + \frac{\tilde{\mu}^2}{1+\tilde{\mu}} \nu^{(2)} + p_\perp^2 \tilde{\mu}^2 \right], \tag{8.71}$$

which in the leading order reads

$$3 p_\perp (p_\perp - \xi) = \frac{(p_\perp - \xi)^2}{2} + \frac{\varkappa^2}{2(1+\tilde{\mu})}. \tag{8.72}$$

The solution of the latter provides us the most probable transverse momentum:

$$p_{e\perp} = m_e c \xi \left(1 + \frac{\gamma^2}{6} \frac{1}{1 + \frac{m_e}{m_i}} \right). \tag{8.73}$$

The derived transverse momentum component contains a nonadiabatic correction, the term $\sim \gamma^2$ in Eq. (8.73), which is absent in our simpleman estimation via Eqs. (8.20) and which is disturbed by the ion recoil (see the term m_e/m_i).

The second condition of the maximal probability $\partial \mathcal{F}/\partial p_z = 0$ is

$$3 \left[1 + (1-\tilde{\mu}) p_z + \frac{\tilde{\mu}^2}{1+\tilde{\mu}} \nu^{(2)} \right] \left\{ (1-\tilde{\mu}^2) \frac{\xi^2}{2} + p_z (1+\tilde{\mu}) - \nu^{(2)} \tilde{\mu} \right.$$
$$\left. - (1-\tilde{\mu}^2) \xi p_\perp \right\} = (1-\tilde{\mu}) \left\{ \nu^{(2)} \left(1 + \frac{\xi^2 \tilde{\mu}^2}{2} \right) + \nu^{(4)} \right.$$
$$+ (1+\tilde{\mu}) \left[1 + (1-\tilde{\mu}) p_z \right] \frac{\xi^2}{2}$$
$$\left. - (1+\tilde{\mu}) \xi p_\perp \left[1 + \tilde{\mu} + (1-\tilde{\mu}) p_z + \frac{\tilde{\mu}^2}{1+\tilde{\mu}} \nu^{(2)} \right] \right\}. \tag{8.74}$$

In the leading order, the Eq. (8.75) is simplified:

$$3 \left[(1-\tilde{\mu}) \frac{\xi^2}{2} + p_z - \frac{p_\perp^2}{2} \tilde{\mu} - \tilde{\mu} \frac{\varkappa^2}{2(1+\tilde{\mu})} - (1-\tilde{\mu}) \xi p_\perp \right]$$
$$= (1-\tilde{\mu}) \left[\frac{p_\perp^2}{2} + \frac{\varkappa^2}{2(1+\tilde{\mu})} + \frac{\xi^2}{2} - \xi p_\perp \right], \tag{8.75}$$

the solution of which provides us the most probable longitudinal momentum:

$$p_{e\,z} = \frac{p_{e\perp}^2}{2 m_e c} + \frac{I_p}{3c} \left(1 + \frac{m_e}{M} \right). \tag{8.76}$$

The ion momentum is derived from Eqs. (8.63) and (8.64). The second term corresponds to the momentum of the electron at the tunnel exit. The longitudinal component of the ion momentum, then, is

$$p_{i\,z} = \frac{p_\perp^2}{2m_e c}\frac{m_e}{m_i} + \frac{2I_p}{3c}\left(1 - \frac{m_e}{2M}\right). \tag{8.77}$$

The electron and ion longitudinal momentum Eqs. (8.76) and (8.77) are different from the prediction of the simpleman model Eqs. (8.21) and (8.23). It is due to the nonvanishing electron-ion relative momentum at the tunneling exit which depends on the ionization energy I_p as well as on the mass ratio m_e/M. The latter factor describes the role of the ion motion during the tunneling process.

Now, from Eqs. (8.73), (8.76), and (8.77), we are able to evaluate the most probable momentum for ionization of exotic atoms, taking into account the effect of the ion motion on the ionization dynamics.

Muonium

In the case of muonium (electron and antimuon) the most probable momentum of the electron is

$$p_{e\perp} \approx m_e c\xi\left(1 + 0.166\gamma^2\right), \tag{8.78}$$

$$p_{e\,z} \approx \frac{p_{e\perp}^2}{2m_e c} + 0.335\frac{I_p}{c}. \tag{8.79}$$

The momentum of the antimuon is

$$p_{\bar{\mu}\perp} \approx m_e c\xi\left(1 + 0.166\gamma^2\right), \tag{8.80}$$

$$p_{\bar{\mu}\,z} \approx \frac{p_{e\perp}^2}{414m_e c} + 0.665\frac{I_p}{c}. \tag{8.81}$$

Muonic hydrogen

In the case of a muonic hydrogen atom (muon and proton) the most probable momentum of the muon is

$$p_{\mu\perp} \approx m_e c\xi\left(1 + 0.1498\gamma^2\right), \tag{8.82}$$

$$p_{\mu z} \approx \frac{p_{\mu\perp}^2}{2m_\mu c} + 0.367\frac{I_p}{c}\,, \tag{8.83}$$

While for the proton they are

$$p_{p\perp} \approx m_e c\xi\left(1 + 0.1498\gamma^2\right)\,, \tag{8.84}$$

$$p_{p z} \approx \frac{p_{\mu\perp}^2}{16m_\mu c} + 0.633\frac{I_p}{c}\,, \tag{8.85}$$

Positronium

In the case of a positronium atom the most probable momentum of the photoelectron is

$$p_{e\perp} = m_e c\xi\left(1 + \frac{\gamma^2}{12}\right)\,, \tag{8.86}$$

$$p_{e z} = \frac{p_{e\perp}^2}{2m_e c} + \frac{I_p}{2c}\,. \tag{8.87}$$

The positron momentum components are the same by the absolute value (the transverse momentum is opposite).

8.4.3 The role of the Coulombic atomic potential

In the discussion above, we assumed a short-range atomic potential, Eq. (8.40). Now we examine how the SFA calculations are modified when the exact Coulombic atomic potential is employed. In this case the matrix element $\langle\vec{p}|V|\Phi_0\rangle = -\sqrt{\kappa}/(2\pi)$ should be replaced by

$$\begin{aligned}\langle\vec{p}|V|\Phi_0\rangle &= \frac{4\sqrt{\pi}\alpha\kappa^{3/2}}{\kappa^2 + p_\perp^2 + \left[p_z + \beta(\tau)\right]^2} \\ &\approx \frac{4\sqrt{\pi}\alpha\kappa^{3/2}}{\kappa^2 + p^2}\left[1 - \frac{2p_z\beta(\tau)}{\kappa^2 + p^2}\right],\end{aligned} \tag{8.88}$$

where $\alpha = e^2/\hbar$ and

$$\begin{aligned}\beta(\tau) &= \beta_0 + \beta_1\sin(\omega\tau + \varphi_0) \\ \beta_0 &\equiv \left(1 - \frac{m_e}{m_i}\right)\frac{m_e c\xi^2}{2},\end{aligned}$$

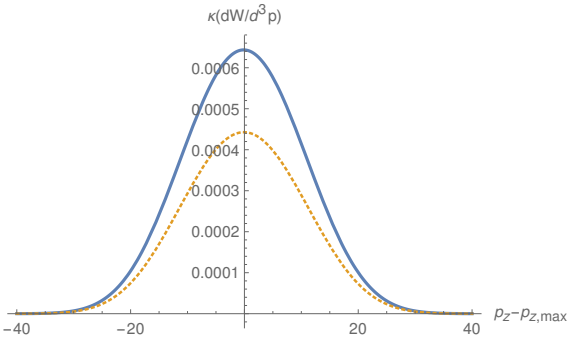

Figure 8.1: The electron distribution function over the momentum along the laser propagation direction $p_z \equiv p_{e\,z}/(m_e c\xi^2/2)$ in the case of a positronium ionization: (solid) via Eq. (8.90) using Coulomb atomic potential; (dashed) via Eq. (8.51) (multipled by a factor of 100) when atomic potential is modelled by a short range potential. The transverse momentum is evaluated at the maximum of the momentum distribution $p_{e\perp} = m_e c\xi(1+\gamma^2/12)$ according to Eq. (8.86), $p_{z,\,\max} \equiv (p_{e\,\perp}/mc\xi)^2 + \gamma^2/2$ corresponds to the longitudinal component of the electron momentum at the maximum of the distribution according to Eq. (8.87). The laser parameters are $E_0/E_a = 0.2$, $\omega = 0.05$ ($\gamma = 0.5$, $\xi = 0.0172$).

$$\beta_1 \equiv \left(1 - \frac{m_e}{m_i}\right)\xi p_\perp$$

In Eq. (8.88) we have expanded the expression with respect to $\beta(\tau) \sim 1/c$. Then rather than Eq. (8.46), we will have the following differential ionization rate

$$\begin{aligned}\frac{dW}{d^3\vec{P}d^3\vec{p}} &= \frac{4}{\pi}\sum_n \frac{\alpha^2\kappa^3}{(\kappa^2+p^2)^2}\delta\left(\vec{P}_\perp\right)\delta\left(P_z + \frac{n\omega - \sigma_0}{c}\right) \\ &\times \delta(\Delta)\; J_n^2(\zeta)\left[1 - \frac{4p_z}{\kappa^2+p^2}\left(\beta_0 + \frac{n}{\zeta}\beta_1\right)\right]. \end{aligned} \tag{8.89}$$

The ionization differential rate integrated over the ion momenta reads

$$\begin{aligned}\frac{dW}{d^3\vec{p}_e} &\approx \frac{4}{\pi}\frac{J_n^2(\zeta)}{1 + \dfrac{p_{ez}}{m_i c} - \dfrac{m_e}{m_i}\nu} \\ &\times \frac{\alpha^2\kappa^3}{(\kappa^2+p^2)^2}\left[1 - \frac{4p_z}{\kappa^2+p^2}\left(\beta_0 + \frac{n}{\zeta}\beta_1\right)\right], \end{aligned} \tag{8.90}$$

where $p^2 = p_{e\perp}^2 + \left(p_{ez} - m_e^2 c\nu/M\right)^2$ and $p_z = p_{ez} - m_e^2 c\nu/M$. The parameters ζ, ν, n are determined by Eqs. (8.48), (8.49) and (8.54).

The qualitative behaviour of the ionization rate is illustrated in Fig. 8.1 on the example of the positronium ionization. The accounting of the exact atomic potential corrects only the value for the ionization rate, but the position of the peak of the

momentum distribution is determined by the Bessel function. Therefore, one can rely on the conclusions on the momentum sharing between the ion and the electron presented in this section above. Figure 1 illustrates that our analytical expression o Eq. (8.87) [which is the particular $m_e = m_i$ case of the general Eq. (8.76)] provides the correct value for the longitudinal component of the electron momentum at the maximum of the distribution.

8.5 Conclusion

We have investigated the momentum partition between the constituents of exotic atoms during strong field tunneling ionization. The momentum distribution is deviated from the prediction of the simpleman model. One reason for the deviation is that the electron appears in the continuum with nonvanishing momentum along the laser propagation direction which is due to the effect of the magnetically induced Lorentz force during the under-the-barrier dynamics and due to nonadiabatic effects. The second reason is the impact of the recoil of the atomic core on the tunneling dynamics and, therefore, on the momentum shift of the electron (muon) along the laser propagation direction. The second factor is negligible for common atoms but significant in the case of exotic atoms such as muonic hydrogen and positronium.

8.6 Acknowledgment

We acknowledge helpful discussions with Prof. C. H. Keitel. D.C. acknowledges the hospitality of the Max Planck Institute for Nuclear Physics during his three-month visit and thanks Dr. P. P. Corso for funding the Heidelberg visit.

9 Graphene in strong laser field: experiment and theory

In this final chapter we present the article (*R. Ganeev, E. Fiordilino, D. Cricchio, P. P. Corso, M. Suzuki, S. Yoneya, and H. Kuroda* Las. Phys. Lett., doi: 12:065401–, 2015) that can be considered the conclusion of the main project. In fact the main research is to find a model that can explain the dynamic and the characteristics of the graphene. In order to do it we created a model where we have nanorings instead the hexagonal cells of graphene. In this last work we compare the harmonic generation of the graphene driven by one and two laser field with the harmonic generation calculated using our nanoring model.

9.1 Introduction

The laser ablation based high-order harmonic generation (HHG) has been advanced towards the carbon-contained molecules of increasing complexity such as carbon nanofibers and diamond nanoparticles (NP) [69], fullerenes [70, 71, 72], and carbon nanotubes [73, 71]. The estimates of similar plasma structures produced on the surfaces of powdered nanomaterials during laser ablation have shown that the concentration of particles becomes in the range of 1016 - 1017 cm-3 [69, 70], which is sufficient to observe the high-order nonlinear optical processes induced in these species. The cross-section of recombination of the accelerated electron with the parent particle in the case of NP is higher compared with the atoms [74]. The uncertainty in the exact mechanism of the HHG from NP has previously been underlined in a few studies [75, 74, 76] . Among

additional mechanisms, the ionization and recombination to the same ion, to the neighboring ions, and to the whole NP have been proposed. The experiments with gas NP have revealed some difficulties in disentangling the harmonics produced by different species (monomers and NP of different sizes). One has to note that the comparative studies of HHG in the plasmas consisted of either NP or monomers showed that, at optimal experimental conditions, the former emitters provide stronger harmonic yield, thus pointing out the advanced properties of the large emitters of harmonics in the NP-contained plasmas. In the meantime, the nonlinear optical properties of another clustered species, graphene, have been in the centre of various theoretical and experimental studies during last few years [77, 78, 79, 80, 81, 82, 83]. Particularly, the HHG from a graphene sheet exposed to intense femtosecond laser pulses has been calculated in Ref. [83] based on the three-step model of HHG. They predicted that graphene may generate more intense harmonic signals than gas-phase atoms or molecules and serve as a useful tool for selective harmonic generation when exposed to an intense driving laser field. The first experimental evidence of harmonic generation in this medium has been reported in Ref. [77] by using the ablation technique for graphene-contained plasma formation with further propagation of the ultrashort pulses through the preformed plasma medium. In the meantime, the interaction of the plasma components with the laser fields are rather complex and the content of the emitting particles is not well determined, thus a theoretical approach that might give a quick qualitative hint on the expected results is called for. The important issues that were missed during those first observations of the harmonic generation from the graphene-contained plasmas are the morphological studies of the debris of ablated graphene, comparative application of the single- and two-color pumps of plasma, use of recently developed double-pulse method for the HHG in the powdered targets, and theoretical consideration of the HHG in this medium based on the conditions of experiments. In this chapter, we address these issues and show the peculiarities of harmonic generation in the plasma contained the wrapped sheets of graphene. We also describe a simple model of laser-graphene interaction, which reasonably well reproduces the details of the experimental findings.

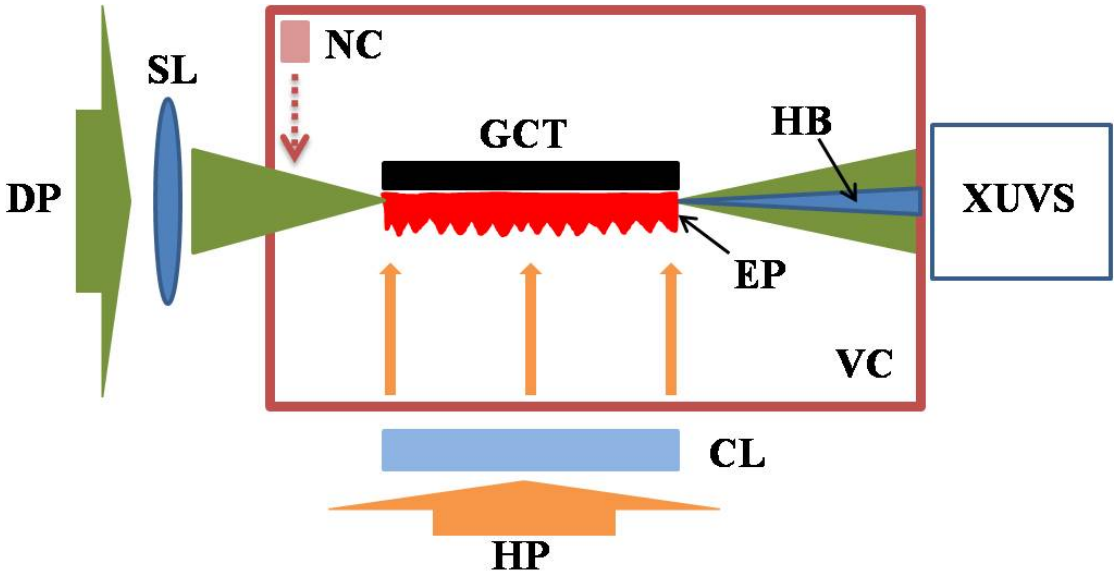

Figure 9.1: Experimental setup. DP, driving pulse; HP, heating pulse; SL, spherical lens; CL, cylindrical lens; VC, vacuum chamber; GCT, graphene-containing target; EP, extended plasma; NC, nonlinear crystal (BBO); HB, harmonic beam; XUVS, extreme ultraviolet spectrometer.

9.2 Experiment

Analysis of the morphology of original and ablated graphene

The experimental setup was similar to those used for the harmonic generation in various laser-produced extended plasmas [84]. Briefly, the uncompressed radiation of Ti:sapphire laser (central wavelength $\lambda = 802$ nm, pulse duration 370 ps, pulse energy $E_{hp} = 3$ mJ) was used to ablate the graphene-contained target and to form the extended plasma plume using the cylindrical focusing of the heating pulse [Fig. 9.1]. The compressed driving pulse from the same laser with the energy of $E_{dp} = 4$ mJ and 64 fs pulse duration was used, 35 ns from the beginning of ablation, for the focusing inside the graphene-contained plasma. The intensity of driving pulse inside the plasma volume was $8 \cdot 10^14$ W/cm^2. The harmonic emission was analyzed by an extreme ultraviolet spectrometer. Graphene nanoparticle powder (SkySpring Nanomaterials Inc.) was used as the ablating target. The powder of graphene NP was glued on the 5-mm-long glass plates, which were then installed in the vacuum chamber for ablation. The morphology of graphene was analyzed using the transmission electron microscopy

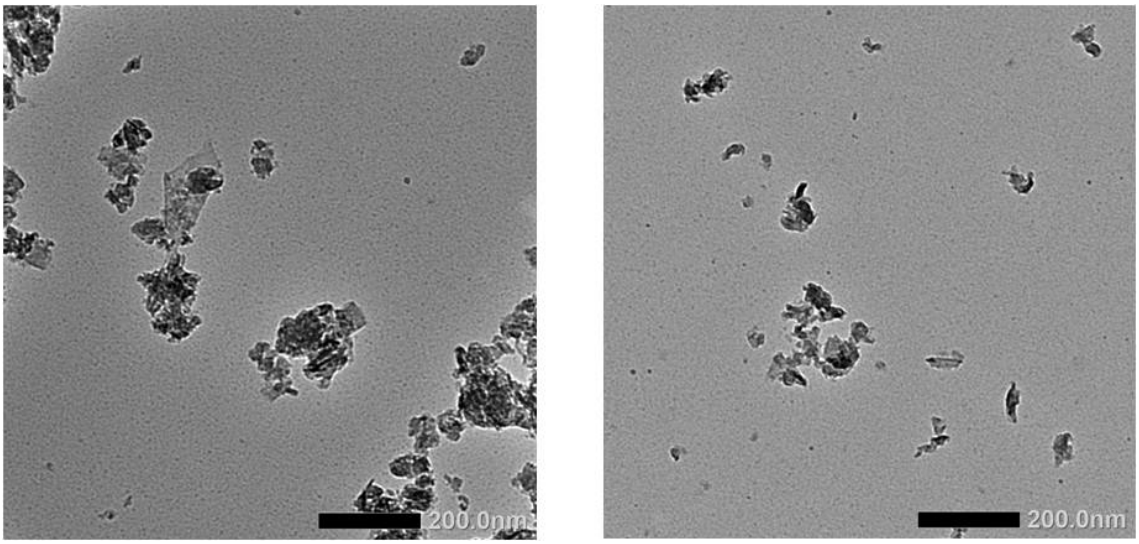

Figure 9.2: TEM images of original graphene nanopowder (left panel) and deposited debris (right panel) at the optimal conditions of ablation. The length of the black lines is 200 nm.

(TEM) of the original NP and plasma debris. Left panel of Fig. 9.2 shows the TEM image of as-supplied powder of graphene. The sizes of graphene NP were distributed in a broad range of 10 - 80 nm. We also analyzed the plasma debris, which were collected on the carbon grids placed nearby to ablation area, at the optimal and non-optimal conditions of NP-contained plasma formation. These conditions refer to the strong and weak harmonic yields from the graphene-contained plasma. The analysis of post-ablation conditions of the deposited debris provides the information about the plasma components despite the possible difference between the composition of the plasma in its early stages and the deposited material, which can be modified due to the aggregation on the substrate. To compare the dependence of the spatial characteristics of the debris under different ablating conditions, the target was ablated using the 370 ps pulses of the Ti:sapphire laser at a repetition rate of 10 Hz using the variable fluencies. The right panel of Fig. 9.2 shows the material ejected upon ablation of graphene nanopowder. One can see that the shapes of deposited material were similar to those of the initial NP-contained target, though the sizes of deposited NP were smaller, probably due to disintegration of large crumpled and wrapped sheets of graphene onto the smaller parts. The monolayer, bilayer, and trilayer nanosized chunks were observed depending on the conditions of ablation. In these studies, the moderate laser ablation fluency ($\sim$ 0.7

J/cm^2) was used, which corresponded to the conditions of efficient HHG. Ablation of the graphene-contained target by higher fluency ($\sim$ 2 J/cm^2) did not yield similar nanostructured deposits, but rather the groups of chaotically shaped large aggregates. The harmonic yield from the plasma produced using high fluency of heating pulses was lower compared with the optimal conditions of ablation. The use of high ablation fluencies resulted in the formation of the large amount of free electrons, which is a detrimental factor for the HHG due to the growing contribution of latter species on the phase mismatch between the driving and harmonic waves. The presence of larger amount of NP in the plasma did not compensate for the deteriorated phase relations between interacting waves caused by significant amount of free electrons in the plasma plume.

Variation of harmonic emission using the extended and narrow graphene-contained plasmas

In the case of graphene NP, the ablation plasma plume may contain various species of carbon, i.e. neutrals and ions, small molecules, small and large NP, aggregates, etc., which can contribute to harmonic generation in various extents. It is important to determine their presence in the region where the driving laser beam interacts with the expanding plasma. The indirect confirmation of the change of the role of these species in the harmonic generation can be proven by the observation of the variation of harmonic yield and cutoff at different fluencies of heating radiation. This peculiarity, which showed the relatively strong harmonic yield and low cutoff at moderate ablation (i.e., at a fluency of heating radiation in the range of $0.5 - 0.8$ J/cm^2), as well as the weak harmonic yield and extended cutoff at stronger ablation ($1.5 - 1.8$ J/cm^2), points out the involvement of NP or monomers as the harmonic emitters at these two conditions of ablation. Below we show the results supporting this assumption. Previous studies have shown that the use of extended plasmas enables the growth of HHG efficiency compared with the narrow plasma plumes produced on the bulk targets [84]. Similar feature was observed in the case of the comparative studies of the 0.5- and 5-mm-long graphene NP plasmas (Fig. 9.3 on the next page).

The harmonic cutoff at the "optimal" conditions of ablation of the extended target (i.e. at the fluence of ~ 0.6 J/cm^2, which corresponded to the presence of the NP in the plasma plume) was H21 (upper panel).Note that, in the case of extended plasma ($\ell = 5$ mm), the stability of harmonic yield was better compared with the narrow plasma plume ($\ell = 0.5$ mm). The propagation through the extended graphene plasma plume did not lead to attenuation of harmonic radiation caused by absorption due to small density of the NP plasma. The harmonic yield in the case of 5-mm-long plasma was 10 times larger compared with the 0.5-mm-long plasma (middle panel). The over-excitation of 0.5-mm-long target led to appearance of the emission lines from multiply charged carbon followed with the insignificant growth of harmonic yield compared with the former case (bottom panel).

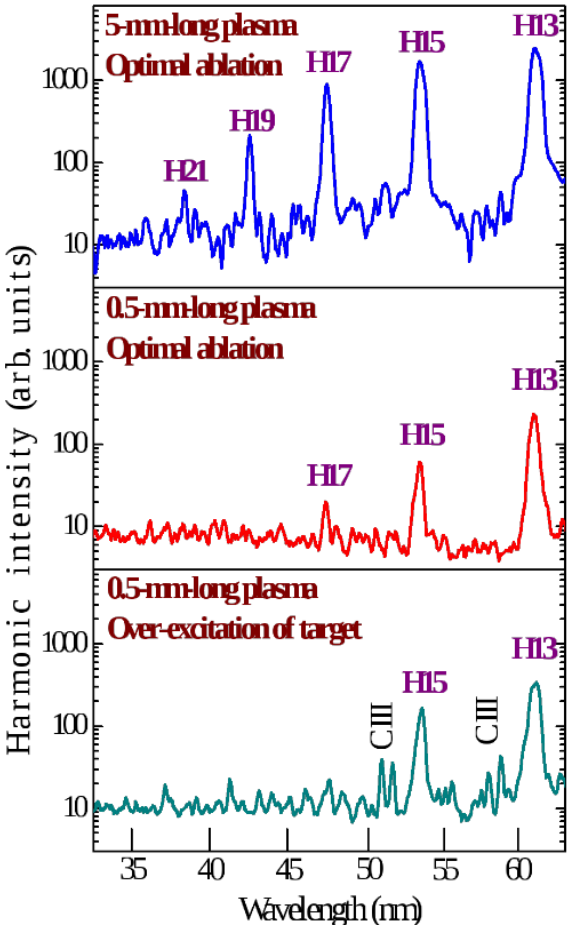

Figure 9.3: Harmonic spectra from 5 mm-long (upper panel) and 0.5 mm-long (middle panel) graphene-containing plasma at the optimal ablation of targets. The over-excitation of graphene containing target at the conditions of narrow plasma formation (bottom panel) led to the appearance of C III emission lines, followed by the insignificant growth of harmonic yield.

These studies showed that the divergence and spectral width of the harmonics produced in the graphene NP plasma were larger than those produced in the monomer plasma plumes, particularly in the case of ablation of the bulk graphite. The larger divergence could arise from a stronger influence of the long trajectories of accelerated and recombined electrons on the harmonic yield. This assumption can be explained by the growth of recombination cross section when larger particles have a higher probability to recombine with the returning electron moving on the long trajectory. The obser-

vation of relatively low-order harmonics from the graphene-contained plasma could be related with the involvement of neutral NP as the emitters of coherent radiation. The growth of the fluency of heating radiation from 0.6 to 1.4 J/cm^2 on the 5-mm-long graphene target led to strong plasma emission assigned to the doubly and triply ionized carbon. At these conditions, the harmonic cutoff was extended from H21 to H33, with the weaker harmonic yield along a whole range of generation compared with the case of the "optimal" ablation of graphene NP. This extension of cutoff was related with the appearance of a large amount of ionized carbon monomers, dimers, and trimers, which may largely contribute to the high-order harmonic yield at these conditions. Similar cutoff was observed in the case of ablation of the bulk graphite target. Thus one can assume that the original graphene NP were responsible for the generation of relatively strong harmonics up to the H21, while the appearance of ionized monomers led to extension of cutoff and weaker harmonic yield.

Application of two-color and double-pulse schemes for the HHG in graphene plasma

The division of driving field on two parts, particularly through the second-harmonic generation in the nonlinear optical crystal, may add some insight in the dynamics of harmonic emission in the presence of a weak second field. This weak field can modify the emission spectrum by adding the even harmonic components. It was shown recently that the addition of weak (∼5%) orthogonally polarized second-harmonic field allows a significant growth of odd and even harmonic generation in the silver plasma produced on the extended bulk target [85]. It would be interesting to analyze the influence of similar additional field on the harmonic spectra originated from the graphene NP.

Figure 3 shows the raw images of the single-color (802 nm, upper figure) and two-color (802 nm and 401 nm, bottom figure) pump induced spectra of the harmonics generated in the graphene-contained plasma. The 0.3-mm-thick BBO crystal was installed on the path of the focused driving radiation inside the vacuum chamber [9.1]. Though the second-harmonic ($\lambda = 401$ nm) conversion efficiency was only ∼5%, the energy of this field was sufficient to significantly modify the whole high-order harmonic

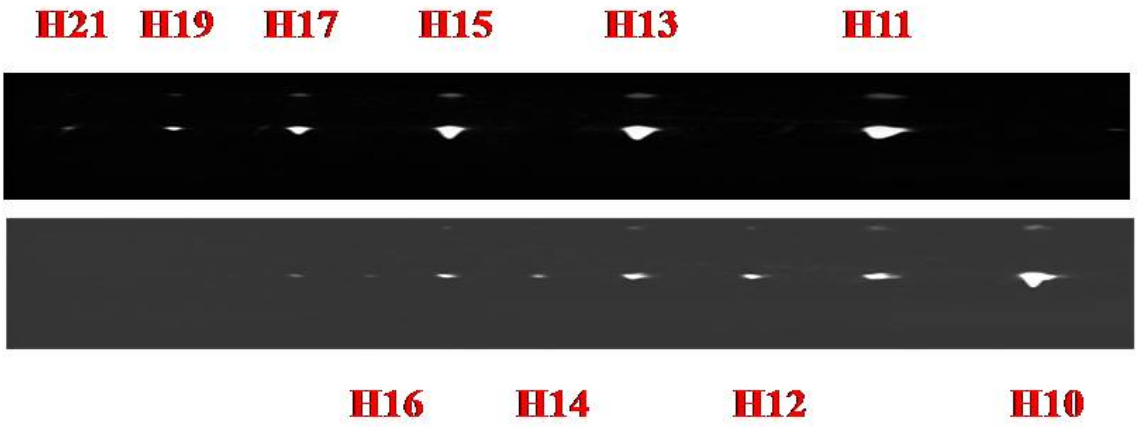

Figure 9.4: Raw images of the harmonics generated in the graphenecontaining plasma using the single-color (802 nm, upper panel) and two-color (802 nm + 401 nm, bottom panel) pumps.

spectrum. The role of 401 nm radiation was clearly underlined in this experiment, which showed that, even at very large difference between the energies of the fundamental and second harmonic fields (95:5), the energies of even harmonics (H10 - H14) were similar to the odd ones. At the same time, these studies showed that, contrary to the monomer plasma [85], the two-color pump of graphene-contained plasma did not lead to the growth of harmonic yield, as well as did not allow the even harmonic generation in the short-wavelength range. Largest even harmonics in these two cases of different emitters corresponded to the H42 [85] and H16 (Fig. 9.4). The reasons of the difference in the involvement of the weak second field in the case of monomers and NP are, probably, related with lesser growth of the ionization rate in the latter case, while, in the case of monomers, the growth of this parameter was assumed to be a main reason of the observed enhancement of harmonic yield in the case of gas HHG experiments [86].

Below we describe our studies of the harmonic generation using the double 802-nm femtosecond pulses propagated close to the graphene-contained target. The harmonics were observed in the case of double-pulse configuration of femtosecond radiation, without the preliminary ablation of target by picosecond heating pulses. The graphene-contained target was moved toward and out of the optical axis of the double-pulse ultrashort radiation using the translation stage to create the conditions when this radiation

"touches" the target. We were able to achieve the conditions when the generating harmonics prevail over the plasma emission induced during ablation of graphene powder by the wings of the spatial distribution of the focused radiation (see inset in Fig. 9.5). The optimization of this process was accomplished by producing the variable driving radiation using the manipulation of the triggering signal on the Pockels cell in the regenerative amplifier of our Ti:sapphire laser. The variation of the delayed signal on the driver of Pockels cell led to separation of single pulse or double pulses, with the time interval between pulses of 8 ns. The variable delay allowed the formation of two driving pulses for harmonic generation (double-pulse scheme) with different ratios between the intensities of these pulses [87]. The usefulness of the application of the proposed double-pulse scheme for the harmonic generation is related with the simplified analysis of the high-order nonlinear optical properties of the media. This scheme can find the application in the nonlinear spectroscopy of powdered materials. One can assume the difficulty in the formation of a sufficient amount of particles in the plasma plume produced during excitation of the target by the spatial wing of the first pulse using the double-pulse scheme. Small interval between first (P1) and second (P2) pulses (8 ns) also prevents the appearance of a large amount

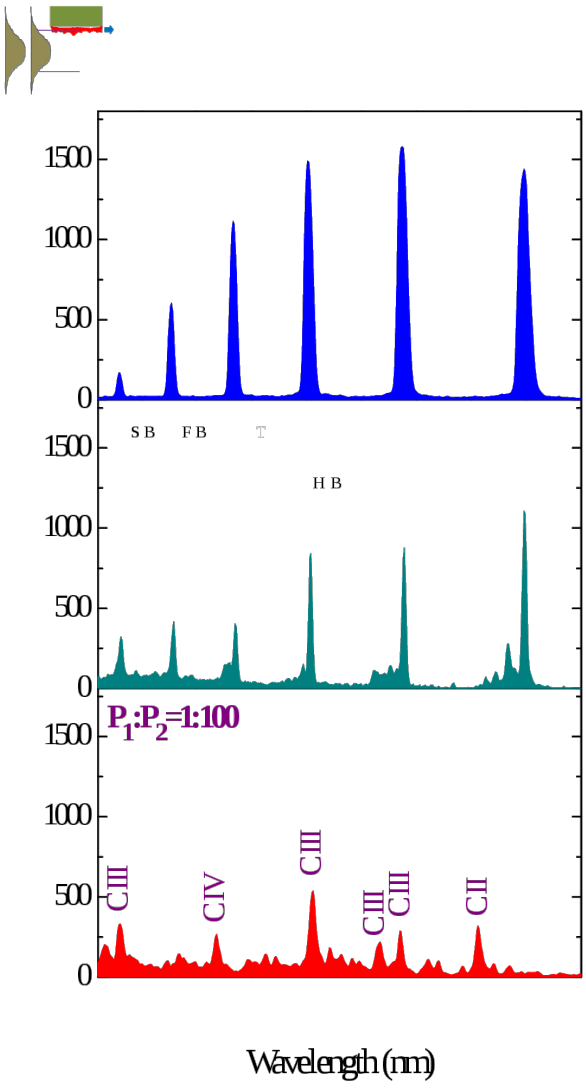

Figure 9.5: Harmonic and plasma spectra obtained during propagation of the laser radiation near the graphene target at different ratios of the P1 and P2. Inset: scheme for harmonic generation using the double-pulse method. FB, first beam; SB, second beam; T, target; HB, harmonic beam.

of plasma particles along the axis of propagation of the second pulse. The heating, annealing, and evaporation of glued graphene powders occurred at the conditions of strong interaction of the wing of the first beam and the target. We gradually moved the graphene-contained target up and down to keep the stable harmonic yield. The ratio between the first and second pulses was varied in a broad range (between 1:100 and 3:1). The optimum conditions were found at the $P_1 : P_2 = 2{:}1$ (Fig. 9.5 on the preceding page, upper panel) when the strong lower-order harmonics were generated while the plasma emission was insignificant. The use of 1:3 ratio between first and second pulses significantly decreased the harmonic yield (middle panel; the plot was 10 times multiplied for better visibility). No harmonics were observed in the case of single pulse (bottom panel) and low $P_1 : P_2$ ratios (¡1:5) of the double-pulse scheme, as well as in the case of pure glue. We compared these double-pulse studies of graphene-contained plasma with similar experiments using extended bulk targets. Particularly, the harmonic cutoff in the case of double-pulse excitation of the bulk silver was lesser than in the case of the conventional heating of target by picosecond pulses followed with the optimally delayed (43 ns) single femtosecond pulse propagation through the silver plasma plume (H27 and H61 respectively). In the meantime, our experiments with graphene-contained plasma showed the opposite results [H31 (not shown in the middle panel of Fig. 9.5 on the previous page) and H23 (upper panel of Fig. 9.3 on page 116)]. The latter difference is related with the involvement of various components of ablated graphene (neutral NP and ionized monomers respectively in the cases shown in the upper panel of Fig. 9.3 on page 116 and middle panel of Fig. 9.5 on the preceding page), while in the case of bulk target, the singly ionized silver monomers were involved in the HHG at the conditions of single- and double-pulse schemes. The difference in the harmonic cutoffs from silver plasma was attributed to the extremely unfavorable conditions of plasma formation on the bulk target using the weak spatial wing of the first pulse in the case of the double-pulse scheme, contrary to the graphene target. The comparison of graphene with similar powdered target (carbon nanofiber powder) showed that the optimal conditions of plasma formation using double-pulse scheme were achieved at significantly different ratios of $P_1 : P_2$ (2:1 and 1:3 [87], respectively).

Probably, the difference in the nonlinear optical properties of the sheets of graphene and the extended (10 μm) tubes of nanofibers was the main reason of the observed optimization of HHG at different ratios of two pulses.

9.3 Theoretical studies of the HHG in graphene

The species content of the plasma used in the experiments cannot be well determined as it depends upon group of factors. However, in spite of the appearance of different components during graphene ablation, it is possible developing a theory, which can account for the observed spectra in different experimental conditions. We focus our attention on the graphene content of the plume and adopt the simplest possible model of HHG, which can give some insight of this process without blurring the main results. The striking geometrical symmetry of complex systems, such as C60 and graphene ring, can be exploited for simplifying, to some extent, the Hamiltonian to be used [88]. For example, a wealth of information on stability, energy levels and other physical properties of spherical carbon allotropes can be gained by modeling the macromolecule as a spherical surface where the electrons are constrained to move [2]. Moreover, the presence of a moderate laser pulse forces the electron to undergo oscillations that may result in an averaging of the details of the location and structure of the atoms within the molecule, hence justifying the use of simple models. Thus the model of a single active electron bound on a spherical surface accounts for HHG [1] and for the experimental observation [72].

Unidimensional models of ring-shaped structures in the presence of laser field have proved that such species could be good emitters of harmonics [30, 41]. Therefore, to explain the basic structure of the experimental spectra emitted by the graphene-contained plasma, we consider a single electron bound over a one-dimensional circle of radius R driven by two orthogonal laser fields with angular frequencies x and y. Such a model is meant to mimic a single graphene ring but can account for a larger planar aggregatio of single graphene rings; however, in what follows, we carry out simulations

for a single ring. The full Hamiltonian of the problem is

$$\mathcal{H} = \mathcal{H}_0 + \Big[\hbar\omega_x g_x \cos(\varphi)\sin(\omega_x t) + \hbar\omega_y g_y \sin(\varphi)\sin(\omega_y t + \theta)\Big] \tag{9.1}$$

where

$$\mathcal{H}_0 = \frac{\hbar^2 \hat{\ell}_z^2}{MR^2} \tag{9.2}$$

is the Hamiltonian of the ring in the absence of the external field, $\hbar^2\hat{\ell}_z^2$ is the z component of the angular momentum operator, M is the mass of the charge carrier, $\hbar\omega_{x(y)}$ is the laser-ring interaction energy, $0 \leq g_x(t) \leq 1$ and $0 \leq g_y(t) \leq 1$ are the profiles of the x and y components of the field. Let $\mid n\rangle = e^{in\varphi}/\sqrt{2\pi}$ and $\hbar\omega_n = \hbar n^2/(2MR^2)$ denote the eigenstates and eigenenergies of $\mathcal{H}_0$ such that $\mathcal{H}_0 \mid n\rangle = \mathcal{H} \mid n\rangle = \hbar\omega_n \mid n\rangle$. It is possible to write the full state $\mid t\rangle$ of the charge carrier in the ring as

$$\mid t\rangle = \sum_{n=-\infty}^{+\infty} c_n(t) \mid n\rangle. \tag{9.3}$$

In this way, the time dependent Schrödinger equation (TDSE) $i\hbar\partial_t = \mathcal{H} \mid t\rangle$ assumes the form of a ladder of coupled differential equations

$$\begin{cases} i\hbar\dot{c}_m(t) = \hbar\omega_m c_m(t) + \dfrac{1}{2\pi}\Big[A(t)c_{m-1} + A(t)^* c_{m+1}\Big] \\ c_m(t=0) = \delta_{m,0} \end{cases} \tag{9.4}$$

where

$$A(t) = \hbar\omega_x g_x \sin(\omega_x t) + i\hbar\omega_y g_y \sin(\omega_y t + \theta) \tag{9.5}$$

By defining $u_{j,k} = c_j^*(t)c_k(t)$, the quantum averaged components of the charge position assume the form

$$x(t) = \langle t \mid x \mid t\rangle = R \sum_{m=-\infty}^{+\infty} \frac{1}{2\pi} u_{m,m-1}(t) + u_{m,m-1}^*(t)\Big] \tag{9.6}$$

$$y(t) = \langle t \mid y \mid t\rangle = R \sum_{m=-\infty}^{+\infty} \frac{i}{2\pi} u_{m-1,m}(t) + u_{m-1,m}^*(t)\Big] \tag{9.7}$$

The electromagnetic emission from the graphene rich plume finds its physical origin in the large accelerations undergone by the molecular charges acted upon by the laser

field. Following the common use, the general properties of the spectrum is obtained by adopting the single active electron approximation that assumes that one electron alone is affected by the field, and by using the classical Larmor formula

$$\frac{dS}{d\omega} = \frac{4q^2}{3c^3} \mid \vec{a}(\omega) \mid^2 \tag{9.8}$$

where $dS/d\omega$ is the energy irradiated in the frequency range $[\omega, \omega + d\omega]$ by the accelerating charge q during the whole laser shot; $\vec{a}(\omega)$ is the Fourier transform of the acceleration; two successive applications of the TDSE give the needed expression for it

$$\begin{aligned}
\ddot{x} &= -\frac{R}{2\pi\hbar^2}\Big\{\hbar\omega_{m-1,m}\dot{u}^*_{m,m-1} + \frac{1}{2\pi}\left[\left(\dot{A}+\dot{A}^*\right)u_{m,m-2} + \left(A+A^*\right)\dot{u}_{m,m-2} - \right. \\
&- \left. \dot{A}^* u_{m-1,m-1} - A^*\dot{u}_{m-1,m-1} - \dot{A}u_{m+1,m-1} - A\dot{u}_{m-1,m-1}\right]\Big\} + cc \qquad (9.9) \\
\ddot{y} &= -\frac{iR}{2\pi\hbar^2}\Big\{\hbar\omega_{m,m-1}\dot{u}^*_{m-1,m} + \frac{1}{2\pi}\left[\left(\dot{A}+\dot{A}^*\right)u_{m-1,m-1} + \left(A+A^*\right)\dot{u}_{m-1,m} - \right. \\
&- \left. \dot{A}^* u_{m-2,m} - A^*\dot{u}_{m-2,m} - A^* u_{m,m} - A\dot{u}_{m,m}\right]\Big\}e + cc \qquad (9.10)
\end{aligned}$$

with

$$i\hbar\dot{u}_{j,k} = \hbar\omega_{k,j}u_{k,j}\frac{1}{2\pi}\left[A(t)u_{j-1,k} + A(t)^* u_{j,k-1} - A(t)u_{j+1,k}\right] \tag{9.11}$$

In what follows we give the results of our numerical calculations with laser and ring parameters equal to those used in the above described experimental conditions; namely the ring radius is $R = 3a_0$ (a_0 is the Bohr radius), the laser photon wavelengths are $\lambda_x = 802$ nm and $\lambda_y = 401$ nm. For simplicity, the pulse profiles were chosen equal and rectangular $g_x(t) = g_y(t) = 1$ and pulse duration $\tau = 25$ optical cycles of the fundamental or $\tau = 6.7 \cdot 10^{-14}$ s. We consider both cases of single or two simultaneous laser fields driving the charge carrier; the total intensity is $I_x + I_y = 8 \cdot 10^{14}$ W/cm^2. When both 802 and 401 nm pulses are present simultaneously, the intensity of the two orthogonal laser fields are taken in the ratio $I_x/I_y = 95/5$. To easy the comparison with the experimental plots, we show only the harmonic content.

We begin our theoretical analysis by considering the case when single laser pulse (802 nm) drives the graphene ring.

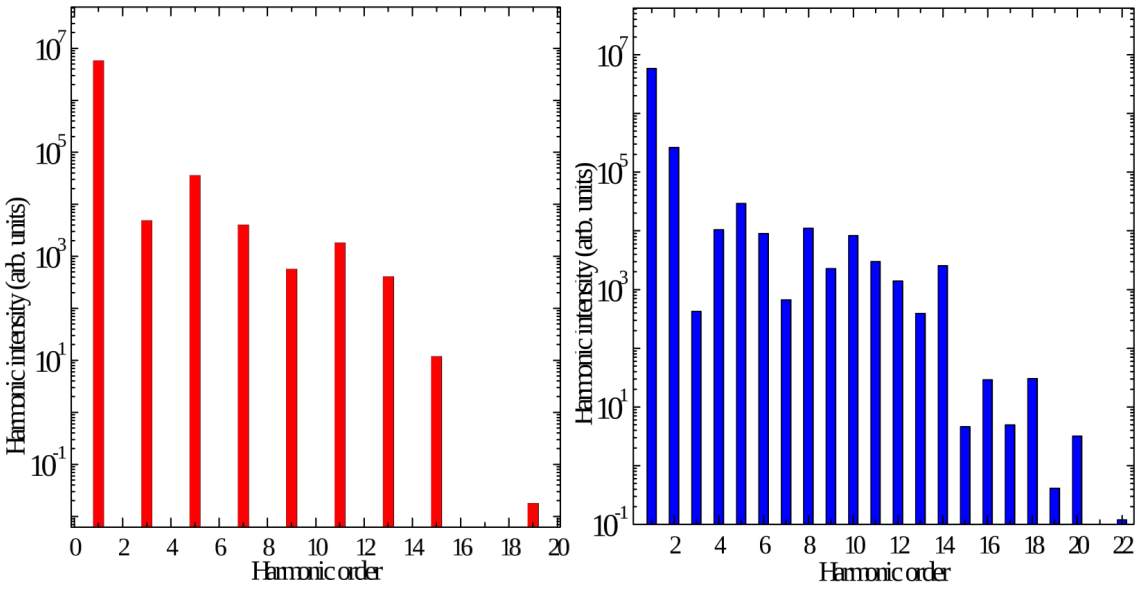

Figure 9.6: left: Spectrum emitted by a graphene unit cell driven by a single, linearly polarized laser field. The parameters of calculations are: R = 3 a_0; laser wavelength $\lambda_x = 802$ nm; laser intensity $I = 8 \cdot 10^{14}$ W/cm^2; and pulse duration $\tau = 6.7 \cdot 10^{-14}$ s. **Right**: Spectrum emitted by a graphene unit cell driven by two orthogonal laser fields. The parameters entering the calculations are: $R = 3$ a_0; laser wavelengths $\lambda_x = 802$ nm and $\lambda_x = 401$ nm; laser intensities $I_x = 7.6 \cdot 10^{14}$ W/cm^2 and $I_y = 4 \cdot 10^{13}$ W/cm^2; and pulse duration $\tau = 6.7 \cdot 10^{-14}$ s.

The harmonic spectrum, shown in Fig. 9.6 (Left), is formed by a plateau followed by a cutoff after H17, which is approximately the same as the experimental one although the descend defined from calculations is rather steeper (compare with Fig. 9.3 on page 116). However the properties of emitted radiation can be controlled with a judicious change of the characteristics of the pump field. For example, an extended cutoff is to be expected by exploiting resonances between the laser photon energy and graphene transition while the polarization state of a particular harmonic can be controlled with the polarization of the laser [30]. It is apparent in Fig. 9.6 (Right) that the presence of an orthogonal, second harmonic laser field ($I_y = 4 \cdot 10^{13}$ W/cm^2, $I_x = 7.6 \cdot 10^{14}$ W/cm^2) slightly extends the plateau in countertendency to the experimental result (see Fig. 9.4 on page 118). However, the use of the weaker laser intensity $I_x = 6 \cdot 10^{14}$ W/cm^2, gives a smaller cut-off and a better general agreement between calculations and experiments. This can be understood by considering that in the present simulation we used the nominal intensity of the experiments and a rectangular pulse shape. This is a simplifying assumption since a real laser pulse presents some spatio-temporal

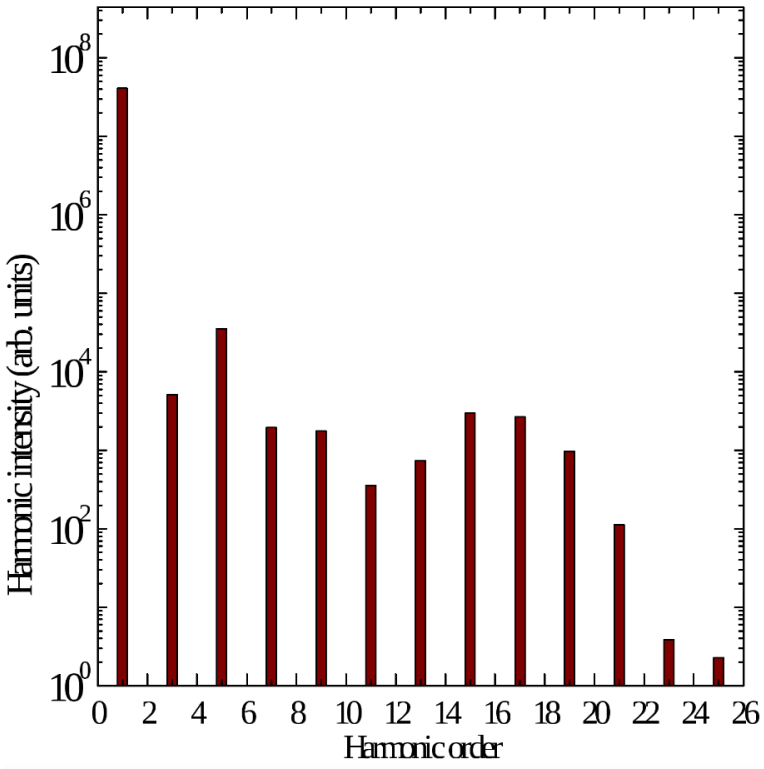

Figure 9.7: Spectrum emitted by a graphene unit cell driven by two sequential linearly polarized laser fields along the x-axis. The parameters entering the calculations are: $R = 3$ a$_0$; laser wavelengths $\lambda_x = 802$ nm; laser intensities $I_{x1} = 8 \cdot 10^{14}$ W/cm^2 and $I_{x1}/I_{x2} = 2$; and pulse duration $\tau = 6.7 \cdot 10^{-14}$ s.

fluctuations, the overall effect of which is the reduction of the average field experienced by the graphene ring. Other results indicate that by changing the phase in Eq. (1) it is possible to achieve a fine control of the extension of cutoff and of the relative intensity of harmonics. Indeed, an adjustable delay of the second, y-polarized pulse, provides an additional control of the overall harmonic spectrum. In this case, time-frequency analysis performed by means of the Morlet's short time Fourier transform indicates a temporal dependence of the profile of selected harmonics, which could allow a real time manipulation of chemical reactions [41]. In this chapter, we restrict the laser physical parameters to those of the experimental conditions; however the system has been theoretically examined in different configurations of the drivers and reveals as an attractive tool for controlling the driving and harmonic radiation. Figure 9.7 shows the spectrum obtained with two sequential pulses both polarized along the x axis with intensity $I_{x1} = 8 \cdot 10^14$ W/cm^2 and $I_{x1} = 2I_{x2}$. The aim of these calculations is a

comparison with the results of double-pulse experiments shown in the upper panel of Fig. 9.5 on page 119. We must stress that this calculation gives only a tentative value, since the experimental conditions are radically different from previous experiments; indeed no attempt has been given to describe the time laps between the two pulses or the changed density of the plasma. However, the agreement is noteworthy; for example, calculations were able to reproduce a local maximum of the H15.

9.4 Discussion

The theoretical model takes into account only the emission from the confined electrons in the graphene component of the plasma. The reasonable agreement with observed experimental data might suggest that the actual plume is mostly formed of small, but entire, planar graphene cells whose emission overcomes that from smaller components such as carbon atoms, molecules or from other fragments and allotropes. This consideration might indicate the possibility of using HHG as a diagnostic tool. Moreover, the mentioned presence of a free electron cloud is detrimental for HHG and can quench the HHG contribution from recollisional electrons thus explaining the fact that a model that does not account for ionization is sufficient. The agreement also shows that fine details of the molecular target are often unnecessary for the description of laser-induced phenomena in complex molecules. Different experimental conditions might be realized and require more refined models. These models should include the details of the interaction between electrons and atoms and a mechanism resembling the three-step model. The model we propose is just a first approximation of the actual system since it takes into account the symmetry of the problem, while excluding the details of any potential, which could mimic the presence of scattering centers. This approach is justified by the fact that during the evolution within the graphene's ring, the electron wave function generally averages fine details of the potential. It seems that recollisional effects do not contribute much to the HHG perhaps because of the presence of both ionized electrons and undistinguished debris of the ablation process. In fact, the obtained results are qualitatively in good agreement with the

experimental results thus showing that the overall profile of the emitted spectrum is mainly due to the angular symmetry of the physical system. Currently, we are trying to improve our model in order to take into account the details of the potential and we are confident we will be able to show more results in the near future moving towards a better level of approximation. In doing so at the moment we are facing the problem of properly shaping the potential, since we are considering a single-active electron model in which we need to take somehow into account the screening effect of the other electrons. Actually the calculations are able to reproduce with accord the extension of the cutoff and some details of harmonic spectrum such as the presence of a local maximum of the intensity of the H15 in Figs. 5 and 7. However the theory predicts a faster quenching than the observed one. The reason of this disagreement cannot be ascertained because of the imprecise knowledge of the plasma composition and of the theoretical assumptions. The above reasons do not allow the quantitative comparison of the observed values of the intensities of harmonics obtained during experimental and theoretical studies. Raw estimates of harmonic efficiency in the range of H11 - H19 ($\sim 5 \cdot 10^{-5}$) allow calculating the approximate amount of coherent XUV photons per pulse ($\sim 2 \cdot 10^{8}$photons/pulse). The theoretical calculations do not allow the direct quantitative definition of the absolute value of converted photons but rather provide the qualitative coincidence of the plateaulike range of harmonic distribution and harmonic cutoff.

9.5 Conclusions

In conclusion, we have analyzed the interaction of ablated graphene and strong laser field. Morphological studies confirmed the presence of relatively large multi-plate graphene species deposited on the nearby substrates at the conditions of the optimal ablation of graphene target using the 370-ps pulses. We have observed the monolayer, bilayer, trilayer, etc. nanosized chunks depending on the conditions of ablation. However, some uncertainty still remains about the correlation of the presence of different graphene NP in the plasma and their influence on the nonlinear optical response of

the medium. The ablation of graphene target at different fluencies of heating pulse has revealed two sources of harmonic generation (the neutral NP in case of intense lower-order harmonics and the ionized monomers in case of higher-order harmonics). We have presented the single- and two-color studies of plasma harmonics during ablation of the graphene powders and obtained the equal odd and even harmonics at very small ratio between the second and fundamental driving energies (1:19). We have also analyzed the HHG using the double-pulse scheme during interaction of the spatial wings of two femtosecond beams with the graphene and found the optimal conditions for the HHG. Finally, we have presented and discussed a simple theory to explain the observations. The graphene ring was modeled as an unstructured one-dimensional circular structure within the single active electron approximation. The comparison between theoretical and experimental spectra showed a reasonable agreement for both the harmonic cutoff and the shape of spectrum.

9.6 Acknowledgments

The authors thank M. Baba for the TEM measurements of graphene and B. Frusteri for preliminary results from improved models.

Part 3

Conclusions

10 Conclusions

The main research of these three years of studies was focused on investigation of the properties of the quantum rings driven by a laser field and on the way they can be used to approximate the the comportment of the graphene in these conditions. In particular we studied

- High harmonic generation
- Polarization of the emitted harmonics
- Energy and angular momentum acquired by the electron
- Modulation of the high harmonic spectrum by changing the laser parameters

All these calculations were performed using both one and two orthogonal lasers and varying the initial parameters such as the laser intensity, the laser photon energy, the shape and the laser pulse duration and the dimensions of the quantum ring. These different initial conditions were performed in order to have a complete knowledge of the dynamic of the nanoring and permit us to demonstrate that our model is a good approximation to calculate the high harmonic spectrum of the graphene driven by a laser field.

The main results obtained in these three years can be summarized as follows:

I We presented the comparisons of the experimental and theoretical studies of high-order harmonic generation in the plasmas containing fullerenes under dif-

ferent conditions and laser duration of the pulse of 4.5 fs and 45 fs. The comparative studies show that, for shorter pulses, the cutoff of harmonic generation from fullerenes increases compared with case of multi-cycle pulses (published in [3]).

II Quantum rings driven by a laser can efficiently emit an electromagnetic field endowed of interesting properties: the characteristics of the harmonic field can be controlled by changing the laser parameters. In particular, our investigations show that the polarization of the driving laser provides a fine tool of control; as a result, the polarization of the diffused harmonics can be tuned. Another interesting result is the fact that non zero angular momentum can be stored in the nanoring (published in [2]).

III In this work we have shown the possibility of controlling the emitted harmonics by changing parameters such as the laser intensity, the energy of the laser photon or the shift between the shape pulses. We notice that the combination of two orthogonal lasers generates a spectrum with more harmonics respect to the case of only one laser. We also studied the spectrum by varying the shift between the pulse shapes. With a Gabor analysis of the spectrum we noticed that the laser with angular frequency ω_x has a greater contribution in the first area of the total spectrum and that it generates the odd harmonics. On the other hand the laser with angular frequency ω_y generates the even harmonics and has a greater contribution in the final area of the total spectrum. Another important result is that we can control the polarization of the emitted harmonics and the angular momentum of the electron. Finally we have shown that the nanoring can acquire a residual angular momentum and that it absorbs and emits energy periodically. With these last results we hope that the nanoring can be used to store angular momentum and use it in quantum information theory (published in [89, 41]).

IV We investigated the possibility to use nanorings driven by a laser field to make logic circuits. In particular we used the emitted signals and the final angular momentum of the nanoring to create logic gate that can be used to make logic

operations. In fact we noticed the possibility to construct the XOR, OR and AND logic gates and use them to make a half and full adder. Combining two or more nanoring, we can obtain a full adder, but the presence of XOR and AND logic gates give us the possibility to make a Toffoli gate. We also can use the angular momentum acquired by the electron in the nanoring to store information. In fact we can consider the final angular momentum like a pseudo-spin that can be reversed by changing the direction of circular polarization of the incident laser field (published in [90, 91]).

V We study a quantum ring driven by an intense laser field that emits electromagnetic radiation stemming from the strong acceleration experienced by the active electrons. In order to elucidate the physical origin of such a rich variety of spectra we study the comportment of one single classical charge constrained both on a plain and a structured ring and acted upon by a linearly polarized laser field. Our simulations show that the response of the ring evidences chaotic and unstable behavior that can be at the origin of the variegated quantum results. Thus the model here discussed might cast light in the still obscure relation between classical chaos and quantum realm.

VI We investigated the momentum partition between the constituents of exotic atoms during strong field tunneling ionization. The momentum distribution is deviated from the prediction of the simpleman model. One reason for the deviation is that the electron appears in the continuum with nonvanishing momentum along the laser propagation direction which is due to the effect of the magnetically induced Lorentz force during the under-the-barrier dynamics and due to nonadiabatic effects. The second reason is the impact of the recoil of the atomic core on the tunneling dynamics and, therefore, on the momentum shift of the electron (muon) along the laser propagation direction. The second factor is negligible for common atoms but significant in the case of exotic atoms such as muonic hydrogen and positronium (published in [92]).

VII We presented the single- and two-color studies of plasma harmonics during ab-

lation of the graphene powders and obtained the equal odd and even harmonics at very small ratio between the second and fundamental driving energies (1:19). We have also analyzed the HHG using the double-pulse scheme during interaction of the spatial wings of two femtosecond beams with the graphene and found the optimal conditions for the HHG. Finally, we have presented and discussed a simple theory to explain the observations. The graphene ring was modeled as an unstructured one-dimensional circular structure within the single active electron approximation. The comparison between theoretical and experimental spectra showed a reasonable agreement for both the harmonic cutoff and the shape of spectrum (published in [93]) .

To finalize, we trust that the present work could be hopefully for a better understanding of the dynamics of the nanorings, and in general of the dimensionally reduced systems, driven by strong fields.

Publications

Ph. D. Publications

[1] D. Cricchio and E. Fiordilino *Nanoscale*, doi:10.1039/C5NR06905J, 2015.

[2] D. Cricchio, E. Fiordilino and K. Z. Hatsagortsyan *Phys. Rev. A* **92**, 023408 (2015).

[3] R. Ganeev, E. Fiordilino, D. Cricchio, P. P. Corso, M. Suzuki, S. Yoneya, and H. Kuroda *Las. Phys. Lett.* **12**(6), 065401 (2015).

[4] D. Cricchio and E. Fiordilino *Las. Phys. Lett.*, **11**(6), 066002 (2014), doi: 10.1088/1612-2011/11/6/066002.

[5] R. A. Ganeev, C. Hutchison, T. Witting, F. Frank, S. Weber, W. A. Okell, E. Fiordilino, D. Cricchio, F. Persico, A. Zaïr, John W. G. Tisch and J. P. Marangos *J. Opt. Soc. Am. B, Opt. Phys.* **30**(1), 7-12 (2013).

[6] G. Castiglia, P. P. Corso, D. Cricchio, R. Daniele, E. Fiordilino, F. Morales, and F. Persico *Phys. Rev. A* **88**, 033837 (2013).

Acts of Congress: Abstracts and Poster

[7] D. Cricchio and E. Fiordilino ISBN: 978-88-907460-8-6, 28/09-02/10/ 2015 (*Book of Abstract: Italian National Conference on Condensed Matter Physics FISMAT 2015*).

[8] D. Cricchio and E. Fiordilino *Nanoring as logic gate and memory mass device* (*Poster: Italian National Conference on Condensed Matter Physics FISMAT 2015*).

[9] D. Cricchio, G. Castiglia, P. P. Corso, R. Daniele, E. Fiordilino, and F. Morales *(Abstract and Seminar: 22th International Laser Physics Workshop (LPHYS'13) July 15-19, 2013, Prague, Czech Republic.)*

Pre Ph. D. Publications

[10] D. Cricchio, E. Fiordilino, and F. S. Persico *Phys. Rev. A* **86**, 013201 (2012).

[11] D. Cricchio, P. P. Corso, E. Fiordilino, G. Orlando, and F. Persico. *J. Opt. Soc. Am. B, Opt. Phys.* **42**, 085404 (2009).

11 Congresses

22nd INTERNATIONAL LASER PHYSICS WORKSHOP - (Prague, July 15-19, 2013)

Speakers (July 19): Nanorings driven by a laser field.

Abstract: We present the dynamics of an electron constrained over an 1D ring with radius of 0.142 nm driven by a laser field. The temporal evolution of the system is evaluated by a semi-analytical solution of the full quantum time dependent Schrödinger equation. In our calculation the gap energy between the ground and the first excited state of the nanoring is three times the photon energy laser (0.63 eV) and the laser intensity is $4 \cdot 10^{14}$ W/cm^2. Our analysis is performed by considering different polarization states of the incident laser. Our attention is mainly focused on the study of the High Harmonic Generation (HHG), the energy and the angular momentum absorbed by the driven system. We observe 1) that the harmonic yield is strongly dependent upon the pump polarization field and almost vanishes for circular polarization and 2) that the ring can be left in a state with average angular momentum different than zero.

Italian National Conference on Condensed Matter Physics - FISMAT 2015 - (Palermo September 28 - October 2, 2015)

Poster and Abstract (September 28): Nanoring as logic gate and memory mass device.

Abstract: We study the application of one nanoring driven by a laser field in different states of polarization in logic circuits. In particular we show that assigning boolean values to different state of the incident laser field and to the emitted signals, we can create logic gates such as OR, XOR and AND. We also show the possibility to make logic circuits such as half-adder and full-adder using one and two nanoring respectively. Using two nanorings we made the Toffoli gate. Finally we use the final angular momentum acquired by the electron to store information and hence show the possibility to use an array of nanorings as a mass memory device.

12 Schools

International School on Graphene based systems (Cargese)
(07-19/04/2014)

International School on the "New frontiers in down-scaled materials and devices: realization and investigation by advanced methods" (Otranto).
(14-20/09/2014)

Bibliography

[1] D. Cricchio, P. P. Corso, E. Fiordilino, G. Orlando, and F. Persico. *J. Phys. B: At., Mol. Opt. Phys.*, 42(8):085404, 2009.

[2] D. Cricchio, E. Fiordilino, and F. Persico. *Phys. Rev. A*, 86:013201, Jul 2012.

[3] R. A. Ganeev, C. Hutchison, T. Witting, F. Frank, S. Weber, W. A. Okell, E. Fiordilino, D. Cricchio, F. Persico, A. Zaïr, et al. *J. Opt. Soc. Am. B*, 30(1):7–12, 2013.

[4] X. Y. Kong, Y. Ding, and Z. L. Wang. *Science*, 303(5662):1348–1351, February 2004.

[5] I. Bâldea, A. K. Gupta, L. S. Cederbaum, and N. Moiseyev. *Phys. Rev. B*, 69:245311, Jun 2004.

[6] M. Lewenstein, Ph. Balcou, M. Yu. Ivanov, Anne L'Huillier, and P. B. Corkum. *Phys. Rev. A*, 49:2117–2132, Mar 1994.

[7] M. Heden. *J. Appl. Phys.*, 2005. PhD Thesis Goteborg University 2005.

[8] P. B. Corkum. *Phys. Rev. Lett.*, 71:1994–1997, Sep 1993.

[9] M. Lewenstein, Ph. Balcou, M. Yu. Ivanov, Anne L'Huillier, and P. B. Corkum. *Phys. Rev. A*, 49:2117–2132, Mar 1994.

[10] P. Salières, A. L'Huillier, and M. Lewenstein. *Phys. Rev. Lett.*, 74:3776–3779, May 1995.

[11] A. Di Piazza, E. Fiordilino, and M. H. Mittleman. *Phys. Rev. A*, 64:013414, Jun 2001.

[12] M. Yu Ivanov, P. B. Corkum, and P. Dietrich. *Las. Phys.*, 3, 1993.

[13] B. Sundaram and P. W. Milonni. *Phys. Rev. A*, 41:6571–6573, Jun 1990.

[14] G. Orlando, G. Castiglia, P. P. Corso, and E. Fiordilino. *J. Opt. Soc. Am. B: At., Mol. and Opt. Phys.*, 41(5):055601, 2008.

[15] A. D. Bandrauk and H. Yu. *Phys. Rev. A*, 59:539–548, Jan 1999.

[16] A. Di Piazza, E. Fiordilino, and M. H Mittleman. *J. Opt. Soc. Am. B: At., Mol. and Opt. Phys.*, 34(18):3655, 2001.

[17] T. Zuo, A. D. Bandrauk, M. Ivanov, and P. B. Corkum. *Phys. Rev. A*, 51:3991–3998, May 1995.

[18] G. Castiglia, P. P. Corso, R. Daniele, E. Fiordilino, and F. Morales. *Journal of Modern Optics*, 60(17):1452–1457, 2013.

[19] M Born and E Wolf. *Principles of Optics*. Cambridge University Press, 7 edition, 1999.

[20] V. T. Platonenko and V. V. Strelkov. *Quantum Electronics*, 28(9):749, 1998.

[21] V. V. Strelkov. *Phys. Rev. A*, 74:013405, Jul 2006.

[22] A. Matos-Abiague and J. Berakdar. *Phys, Lett. A*, 330(1âĂŞ2):113 – 119, 2004.

[23] A. Salomon, M. Zielinski, R. Kolkowski, J. Zyss, and Y. Prior. *J. Phys. Chem. C*, 117(43):22377–22382, 2013.

[24] D. Bauer and F. Ceccherini. *Laser and Part. Beams*, 19:85–90, 2001.

[25] R. A. Ganeev, P. A. Naik, H. Singhal, J. A. Chakera, M. Kumar, M. P. Joshi, A. K. Srivastava, and P. D. Gupta. *Phys. Rev. A*, 83:013820, Jan 2011.

[26] R. A. Ganeev, T. Witting, C. Hutchison, F. Frank, P. V. Redkin, W. A. Okell, D. Y. Lei, T. Roschuk, S. A. Maier, J. P. Marangos, and J. W. G. Tisch. *Phys. Rev. A*, 85:015807, Jan 2012.

[27] S. A. Sørngård, S. I. Simonsen, and J. P. Hansen. *Phys. Rev. A*, 87:053803, May 2013.

[28] A. Matos-Abiague and J. Berakdar. *Phys. Lett. A*, 330(1-2):113âĂŞ119, 2004.

[29] N. F. Hinsche, A. S. Moskalenko, and J. Berakdar. *Phys. Rev. A*, 79:023822, Feb 2009.

[30] G. Castiglia, P. P. Corso, D. Cricchio, R. Daniele, E. Fiordilino, F. Morales, and F. Persico. *Phys. Rev. A*, 88:033837, Sep 2013.

[31] I. J. Kim, C. M. Kim, H. T. Kim, G. H. Lee, Y. S. Lee, J. Y. Park, D. J. Cho, and C. H. Nam. *Phys. Rev. Lett.*, 94:243901, Jun 2005.

[32] J. Mauritsson, P. Johnsson, E. Gustafsson, A. L'Huillier, K. J. Schafer, and M. B. Gaarde. *Phys. Rev. Lett.*, 97:013001, Jul 2006.

[33] C. K. Chui. Academic Press, 1992.

[34] A. Fleischer and N. Moiseyev. *Phys. Rev. A*, 74:053806, Nov 2006.

[35] A. Di Piazza, K. Z. Hatsagortsyan, and C. H. Keitel. *Phys. Rev. D*, 72:085005, 2005.

[36] M. Ferray, A. L'Huillier, X. F. Li, L. A. Lompre, G. Mainfray, and C. Manus. *J. Opt. Soc. Am. B: At., Mol. and Opt. Phys.*, 21(3):L31, 1988.

[37] S. De Luca and E. Fiordilino. *J. Mod. Opt.*, 45(9):1775–1783, 1998.

[38] G. Castiglia, P. P. Corso, U. De Giovannini, E. Fiordilino, and B. Frusteri. *J. Opt. Soc. Am. B: At., Mol. and Opt. Phys.*, 48(11):115401, 2015.

[39] J. M. T. Thompson, John Wiley H. B. Stewart, *Nonlinear Dyn. and Chaos*, and LTD Sons. 2002.

[40] *Classical Mechanics*. Pearson Education, 2000.

[41] D. Cricchio and E. Fiordilino. *Las. Phys, Lett.*, 11(6):066002, 2014.

[42] A. H. Nayfeh, John Wiley D. T. Mook, *Nonlinear Oscil.*, and Sons. 1979.

[43] W. Becker, F. Grasbon, R. Kopold, D. Milošević, G. G. Paulus, and H. Walther. *Adv. Atom. Mol. Opt. Phys.*, 48:35, 2002.

[44] N. B. Delone and V. P. Krainov. *Multiphoton processes in atoms* . Springer Series on Atoms+Plasmas. Springer, Berlin, 2000.

[45] M. Protopapas, C. H. Keitel, and P. L. Knight. *Rep. Prog. Phys.*, 60(4):389, 1997.

[46] Yousef I. Salamin, S.X. Hu, Karen Z. Hatsagortsyan, and Christoph H. Keitel. *Phys. Rep.*, 427:41, 2006.

[47] A. Di Piazza, C. Müller, K. Z. Hatsagortsyan, and C. H. Keitel. *Rev. Mod. Phys.*, 84:1177, 2012.

[48] M. Dammasch, Ma. Dörr, U. Eichmann, E. Lenz, and W. Sandner. *Phys. Rev. A*, 64:061402, 2001.

[49] M. Klaiber, K. Z. Hatsagortsyan, and C. H. Keitel. *Phys. Rev. A*, 71(3):033408, 2005.

[50] M. Klaiber, K. Z. H., and C. H. Keitel. *Phys. Rev. A*, 75:063413, 2007.

[51] M. W. Walser, C. H. Keitel, A. Scrinzi, and T. Brabec. *Phys. Rev. Lett.*, 85(24):5082–5085, 2000.

[52] M. Klaiber, E. Yakaboylu, H. Bauke, K. Z. Hatsagortsyan, and C. H. Keitel. *Phys. Rev. Lett.*, 110:153004, 2013.

[53] C. T. L. Smeenk, L. Arissian, B. Zhou, A. Mysyrowicz, D. M. Villeneuve, A. Staudte, and P. B. Corkum. *Phys. Rev. Lett.*, 106:193002, 2011.

[54] A. S. Titi and G. W. F. Drake. *Phys. Rev. A*, 85:041404, 2012.

[55] This approach named as a Simpleman theory, has been proposed more than 25 years ago in different variations by several authors, see M. Yu. Kuchiev, JETP Lett. **45**, 404 (1987); H. B. van Linden van den Heuvell and H. G. Muller, in Multiphoton Processes, ed. S. J. Smith and P. L. Knight, Cambridge University Press (1988); K. J. Schafer, B. Yang, L. F. DiMauro, and K. C. Kulander, Phys. Rev. Lett. **70**, 1599 (1993); P. B. Corkum, Phys. Rev. Lett. **71**, 1994 (1993), and proved to have a high predicitve power in discussions of strong-field phenomena.

[56] Szczepan Chelkowski, André D. Bandrauk, and Paul B. Corkum. *Phys. Rev. Lett.*, 113:263005, 2014.

[57] E. Yakaboylu, M. Klaiber, H. Bauke, K. Z. Hatsagortsyan, and C. H. Keitel. *Phys. Rev. A*, 88:063421, 2013.

[58] D. Comtois, D. Zeidler, H. Pépin, J. C. Kieffer, D. M. Villeneuve, and P. B. Corkum. *J. Phys. B*, 38(12):1923, 2005.

[59] A. Ludwig, J. Maurer, B. W. Mayer, C. R. Phillips, L. Gallmann, and U. Keller. *Phys. Rev. Lett.*, 113:243001, 2014.

[60] I. A. Ivanov. *Phys. Rev. A*, 91:043410, 2015.

[61] R. E. F. Silva, F. Catoire, P. Rivière, H. Bachau, and F. Martín. *Phys. Rev. Lett.*, 110:113001, 2013.

[62] O. I. Tolstikhin and L. B. Madsen. *Phys. Rev. Lett.*, 111:153003, 2013.

[63] X. Zhou, P. Ranitovic, C. W. Hogle, J. H. D. Eland, H. C. Kapteyn, and M. M. Murnane. *Nat. Phys.*, 8:232, 2012.

[64] M. Klaiber, , K. Z. Hatsagortsyan, and C. H. Keitel. *Phys. Rev. Lett.*, 114:083001, 2015.

[65] F. H. M. Faisal. *J. Phys. B*, 6(4):L89, 1973.

[66] L. V. Keldysh. *Zh. Eksp. Teor. Fiz.*, 47:1945–1957, 1964.

[67] Howard R. Reiss. *Phys. Rev. A*, 22:1786, 1980.

[68] M. Abramowitz and I. A. Stegun. *Handbook of Mathematical Functions*. Dover, New York, 1970.

[69] R. A. Ganeev, M. Baba, M. Suzuki, and H. Kuroda. *J. Appl. Phys.*, 115"(18"):183101, 2014".

[70] R. A. Ganeev, L. B. Elouga Bom, J. Abdul-Hadi, M. C. H. Wong, J. P. Brichta, V. R. Bhardwaj, and T. Ozaki. *Phys. Rev. Lett.*, 102:013903, Jan 2009.

[71] R. A. Ganeev, P. A. Naik, H. Singhal, J. A. Chakera, M. Kumar, U. Chakravarty, and P. D. Gupta. *Opt. Commun.*, 285(12):2934 – 2941, 2012.

[72] R. A. Ganeev, C. Hutchison, T. Witting, F. Frank, S. Weber, W. A. Okell, E. Fiordilino, D. Cricchio, F. Persico, A. Zaïr, J. W. G. Tisch, and J. P. Marangos. *J. Opt. Soc. Am. B*, 30(1):7–12, Jan 2013.

[73] R. A. Ganeev, P. A. Naik, H. Singhal, J. A. Chakera, M. Kumar, M. P. Joshi, A. K. Srivastava, and P. D. Gupta. *Phys. Rev. A*, 83:013820, Jan 2011.

[74] H. Ruf, C. Handschin, R. Cireasa, N. Thiré, A. Ferré, S. Petit, D. Descamps, E. Mével, E. Constant, V. Blanchet, B. Fabre, and Y. Mairesse. *Phys. Rev. Lett.*, 110:083902, Feb 2013.

[75] P. Moreno, L. Plaja, and L. Roso. *EPL (Europhys. Lett.)*, 28(9):629, 1994.

[76] V. Véniard, R. Taïeb, and A. Maquet. *Phys. Rev. A*, 65:013202, Dec 2001.

[77] R. A. Ganeev, M. Suzuki, M. Baba, Sh. Yoneya, and H. Kuroda. *JETP Letters*, 100(7):434–438, 2014.

[78] M. Gullans, D. E. Chang, F. H. L. Koppens, F. J. García de Abajo, and M. D. Lukin. *Phys. Rev. Lett.*, 111:247401, Dec 2013.

[79] E. Hendry, P. J. Hale, J. Moger, A. K. Savchenko, and S. A. Mikhailov. *Phys. Rev. Lett.*, 105:097401, Aug 2010.

[80] Kenichi L. Ishikawa. *Phys. Rev. B*, 82:201402, Nov 2010.

[81] S. A. Mikhailov. *Phys. Rev. B*, 84:045432, Jul 2011.

[82] S. Wu, L. Mao, A. M. Jones, W. Yao, C. Zhang, and X. Xu. *Nano Lett.*, 12(4):2032–2036, 2012. PMID: 22369519.

[83] Stian Astad Sørngård, Sigrid Ina Simonsen, and Jan Petter Hansen. *Phys. Rev. A*, 87:053803, May 2013.

[84] R. A. Ganeev, M. Suzuki, and H. Kuroda. *Phys. Plasmas*, 21(5):053503, 2014.

[85] R. A. Ganeev, M. Suzuki, and H. Kuroda. *J. Opt. Soc. Am. B*, 31(4):911–918, Apr 2014.

[86] I J. Kim, G. H. Lee, S. B. Park, Y. S. Lee, T. K. Kim, C. H. Nam, T. Mocek, and K. Jakubczak. *Applied Phys, Lett.*, 92(2):021125, 2008.

[87] R. A. Ganeev, M. Suzuki, S. Yoneya, and H. Kuroda. *Applied Phys, Lett.*, 105(4):–, 2014.

[88] D. Bauer and F. Ceccherini. *Laser and Part. Beams*, 19:85–90, 1 2001.

[89] In *Nanorings driven by a laser field*. Laser Physics Workshop 2013, 2013.

[90] D. Cricchio and E. Fiordilino. *Nanoscale*, 2015, doi:10.1039/C5NR06905J.

[91] D. Cricchio and E. Fiordilino. In *Italian National Conference on Condensed Matter Physics (Including Optics, Photonics, Liquids, Soft Matter) FISMAT 2015*, 2015.

[92] D. Cricchio, E. Fiordilino, and K. Z. Hatsagortsyan. *Phys. Rev. A*, 92:023408, Aug 2015.

[93] R. A. Ganeev, E. Fiordilino, D. Cricchio, P. P. Corso, M. Suzuki, S. Yoneya, and H. Kuroda. *Las. Phys, Lett.*, 12(6):065401, 2015.

List of Figures

List of Tables